東北大学機関リポジトリ
TOUR
Tohoku University Repository

Chemical and physical properties of the Fe-S-Si system under high pressure and temperature: Implications for the planetary cores

著者	Sakairi Takanori
学位授与機関	Tohoku University
学位授与番号	11301甲第17703号
URL	http://hdl.handle.net/10097/00121782

博 士 論 文

Chemical and physical properties of the Fe–S–Si system under high pressure and temperature: Implications for the planetary cores

(高温高圧下における Fe–S–Si の化学的及び物理的性質：惑星核への応用)

坂入　崇紀

平成 29 年

Abstract

The physical properties, such as density and sound velocity, of the Earth's deep interior have been determined by seismic observations known as PREM and it is accepted that the core of the Earth is composed of mainly Fe alloy. However, the density and sound velocity of pure iron at high pressure and temperature conditions could not explain those of PREM. This suggests the Earth's core contains some light elements (S, Si, O, C, and H). Sulfur and silicon are both important candidates as light elements and some geochemical models predicted that sulfur and silicon could be present not only in the core of the Earth but also in the core of other terrestrial planets such as Mars and Mercury. Therefore, it is essential for understanding the property of the planetary core to reveal the chemical and physical properties of the Fe–S–Si system. In this study, high pressure experiments in the Fe–S–Si system have been performed related to the melting relationships (Chapter 2), element partitioning (Chapter 3), and sound velocity (Chapter 4). The present experimental results were applied to discuss the core formation of Mars and Mercury and the chemical composition of the Earth's core.

In Chapter 2, the phase and melting relationships in the Fe–S–Si system were determined up to 60 GPa by using a double-sided laser-heated diamond anvil cell combined with X-ray diffraction. On the basis of the X-ray diffraction patterns, I confirmed that hcp/fcc Fe–Si alloys, and Fe_3S are stable phases under subsolidus conditions in the Fe–S–Si system. Both solidus and liquidus temperatures are significantly lower than the melting temperature of pure Fe and both increase with pressure. The slopes of the Fe–S–Si liquidus and solidus curves determined here are smaller than the adiabatic temperature gradients of the liquid cores of Mercury and Mars. -Thus, crystallization of their cores started at the core–mantle boundary region.

In Chapter 3, an experimental study on solid–liquid partitioning in the Fe–S–Si system was reported up to 148 GPa. The metallic liquid phase was relatively sulfur rich, whereas the coexisting hcp-Fe phase was silicon rich. Based on the partitioning data, the total amount of light elements in the bulk core of the Earth was constrained to be 7.4–9.9 wt. %. The present results demonstrated that the present-day Earth has a sulfur-rich outer core and a significant amount of sulfur may create the seismologically observed density contrast between the inner and outer cores.

In Chapter 4, the sound velocity of Fe–6wt. % Si alloy at high pressure and temperature conditions was measured using inelastic X-ray scattering method. The V_P of Fe–Si alloy in this study were followed linear relationships between density and velocity and the present result indicated that the effect of temperature on the V_P of Fe-Si alloy was very small than that of pure iron. The Birch's law for Fe–6wt. % Si, was obtained as $V_P = 0.90 \pm 0.12 \times \rho - 0.15$ (±1.19). By using linear mixing model, the present result indicates that 2.2(3) wt. % of silicon in the Earth's inner core can explain both the density and sound velocity of the PREM at ICB condition assuming that the light element in the inner core is only silicon.

Acknowledgment

I sincerely appreciate Prof. Eiji Ohtani for his encouragement, useful discussions and continuous support for my work. And I greatly acknowledge Dr. Seiji Kamada for his kind help in experiments and useful discussions. I also appreciate Dr. Tatsuya Sakamaki for experimental supports and useful comments. I am also grateful to Dr. Takeshi Sakai for experimental support and useful suggestions. I would like to express my gratitude to Dr. Yuki Shibazaki and Dr. Shin Ozawa for useful comments and their encouragement. I deeply appreciate Dr. Hiroshi Fukui and Dr. Masaaki Miyahara for experimental supports. I also thank Dr. Akio Suzuki, Dr. Motohiko Murakami, Dr. Hidenori Terasaki, Dr. Suguru Takahashi, and Dr. Rei Shiraishi for their useful comments and kind cooperation. I am grateful to Dr. Naohisa Hirao, Dr. Yasuo Ohishi, Dr. Alfred Q.R. Baron, Dr. Satoshi Tsutsui, Dr. Hiroshi Uchiyama, and Dr. Daisuke Ishikawa for providing a chance of the experiments at SPring-8 facility. I also thank to Mr. Kosui Watanabe, Mr. Keitaro Watanabe, and Mr. Akihiro Takahata as a research collaborator. I am so grateful Ms. Yoko Takahashi and Ms. Takako Ohtomo for their encouragement and warm help. I would like to express my special thanks to all of my colleagues for their encouragement, warm help and useful discussions: Ms. Izumi Mashino, Mr. Itaru Ohira, Mr. Fumiya Maeda, Mr. Tomofumi Kawadai, Ms. Nanami Suzuki, Mr. Masaki Tahara, Ms. Mako Igarashi, Mr. Yohei Amaike, Ms. Shuko Kuga, Mr. Ryota Abe, Mr. Sei Sato, Mr. Ryosuke Tanaka, Mr. Hiromu Tobe, Ms. Kei Nozu and Mr. Ko Fukuyama and all members of Department of Earth Science, Tohoku University.

I gratefully acknowledges the Japan Society for the Promotion of Science (JSPS) for providing a research fellowship. This work was supported by a Grant-in-Aid for Scientific Research from the Ministry of Education, Culture, Science, Sport and Technology of the

Japanese Government (no. 22000002 and no. 15H05748) to E.O. This work was partly supported by a grant from the Ministry of Education and Science of the Russian Federation, project 14.B25.31.0032, awarded to E.O. This work was conducted as part of the Global Center of Excellence program “Global Education and Research Center for Earth and Planetary Dynamics”. The XRD experiments were performed at the BL10XU (proposal numbers: 2012B1560, 2013A1496, 2013B0104, 2014A0104, and 2014B014 to Eiji Ohtani) and IXS experiments were conducted at the BL35XU (proposal numbers: 2015A1539 and 2015B1334 to Eiji Ohtani and 2014B1269, 2015A1627, and 2015B1202 to Tatsuya Sakamaki).

Contents

Chapter 1:

Introduction

1.1. The density deficit of the Earth's core

The physical and chemical properties of the Earth's core are major topic and one of the major goals of Earth Sciences. The composition of the core has implications for core dynamics, thermal evolution, planetary formation, and source origin of the geodynamo. We have already known that the Earth's core is mainly composed of iron alloy from the analyses of iron meteorites and the observation of moment of inertia. Therefore, the behavior of iron at high pressure and temperature conditions, such as phase relations, sound velocity, is essential for understanding the structure of the Earth's interior and has been investigated based on high pressure experiments and theoretical calculations. The density and sound velocities of the Earth's deep interior were showed as "PREM (Preliminary Earth reference model)" based on seismological observations [*Dziewonski and Anderson*, 1981]. The sound velocity, longitudinal wave (V_P) and the transversal wave (Vs), can be expressed by the density (ρ) as follows:

$$V_P = \sqrt{\frac{K + \frac{4}{3}\mu}{\rho}} \tag{1-1}$$

$$V_S = \sqrt{\frac{\mu}{\rho}} \tag{1-2}$$

where K and μ are a bulk modulus and a shear modulus. PREM shows that the Earth's core is divided into a solid inner core and a liquid outer core since V_S does nor propagate in a liquid phase.

Birch [1952] proposed that Earth's core was too light to be made of pure iron based on shockwave experiments on iron. This is one of the major topic in Earth Science called "the core density deficit". In order to reveal this density contrast, physical properties of the iron at

high pressure and temperature conditions have been investigated until present day. Fig. 1-1 shows the comparison of between determined density of iron [*Sakai et al*., 2014] and PREM. The density deficit of the Earth's core was estimated to be ~5% for the inner core [e.g., *Dubrovinsky et al*., 2000; *Dewaele et al*., 2006; *Sakai et al*., 2014] and ~10% for the outer core [e.g., *Brown and McQueen* 1986; *Anderson and Ahrens* 1994].

1.2. Sound velocity of the Earth's core

As mentioned before, the sound velocity profile of the Earth' core has been determined by PREM. In order to provide a constraint on the composition of the core, the information of sound velocity of iron at high pressure condition is essential and have been measured by shockwave measurements [e.g., *Brown and McQeen*, 1986], inelastic X-ray scattering method (IXS) [e.g., *Antonangeli et al*., 2012; *Ohtani et al*., 2013; *Sakamaki et al*., 2016] and nuclear resonant inelastic X-ray scattering (NRIXS) [e.g., *Lin et al.*, 2005; *Mao et al.*, 2001]. Fig. 1-2 shows the sound velocity of pure iron reported by previous high pressure works and that of PREM as a function of pressure. Based on the recent result of IXS measurements, the Earth's inner core has ~10% smaller sound velocity than pure iron at high pressure and temperature condition [*Sakamaki et al*., 2016]. Therefore, the sound velocity of the Earth's core could not be explained assuming that the core consists entirely of iron.

1.3. Light elements in the planetary cores

Based on previous high pressure studies, the density and sound velocity of PREM could not be explained by that of pure iron alone. The candidate for the Earth's core is required to match both the density and sound velocity at pressure and temperature conditions of the core. In order to account for the density deficit, the Earth's core requires some additional constituents,

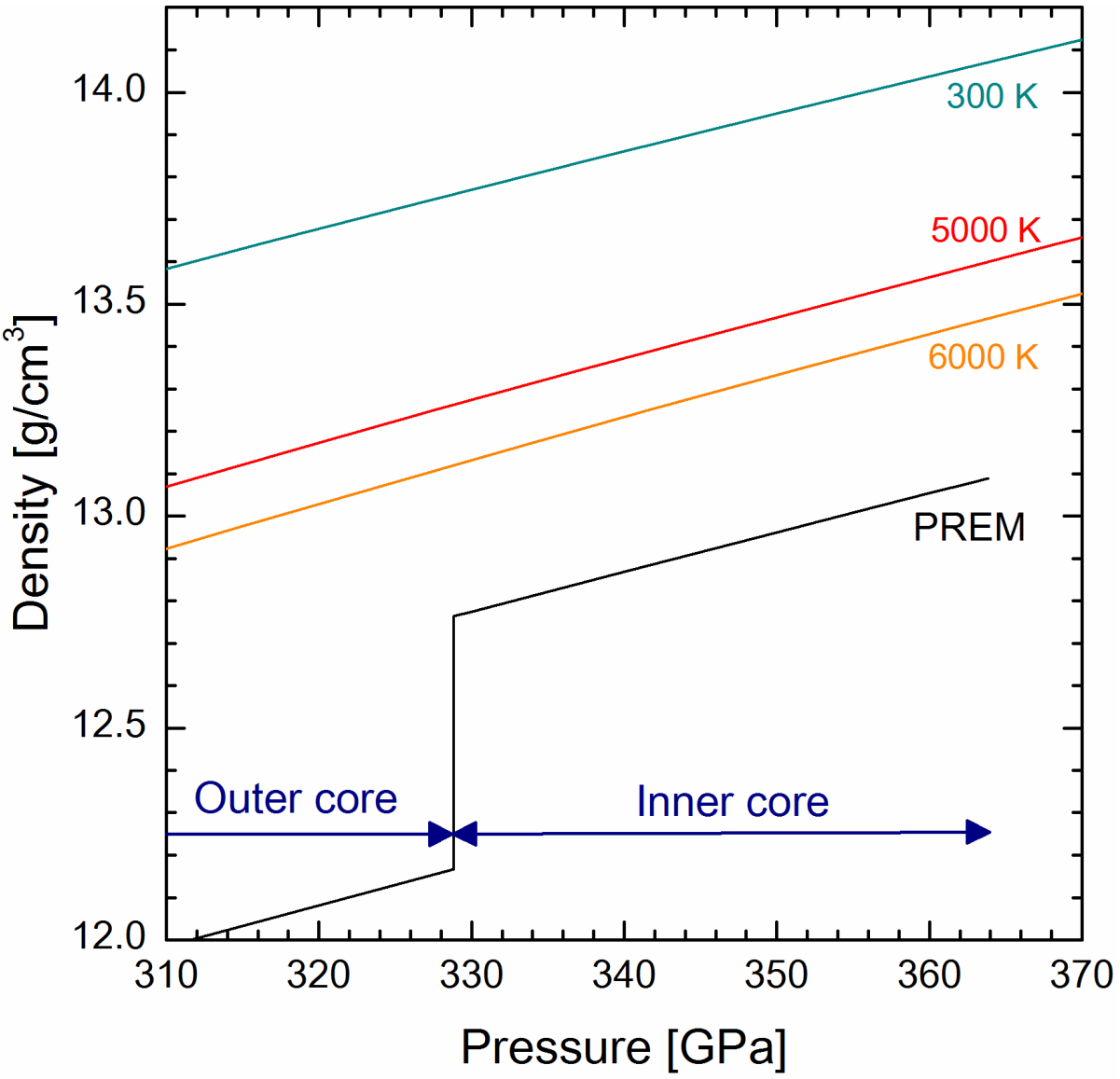

Fig. 1-1. The density of pure iron and that of PREM as a function of pressure. The densities of pure iron were calculated by using thermal equation of state for pure iron [*Sakai et al*., 2014]. Blue, red and orange solid lines represent the compression curves of iron at 300K, 5000K, and 6000 K, respectively. Black line shows the relations between density and pressure of PREM [*Dziewnski and Anderson*, 1981].

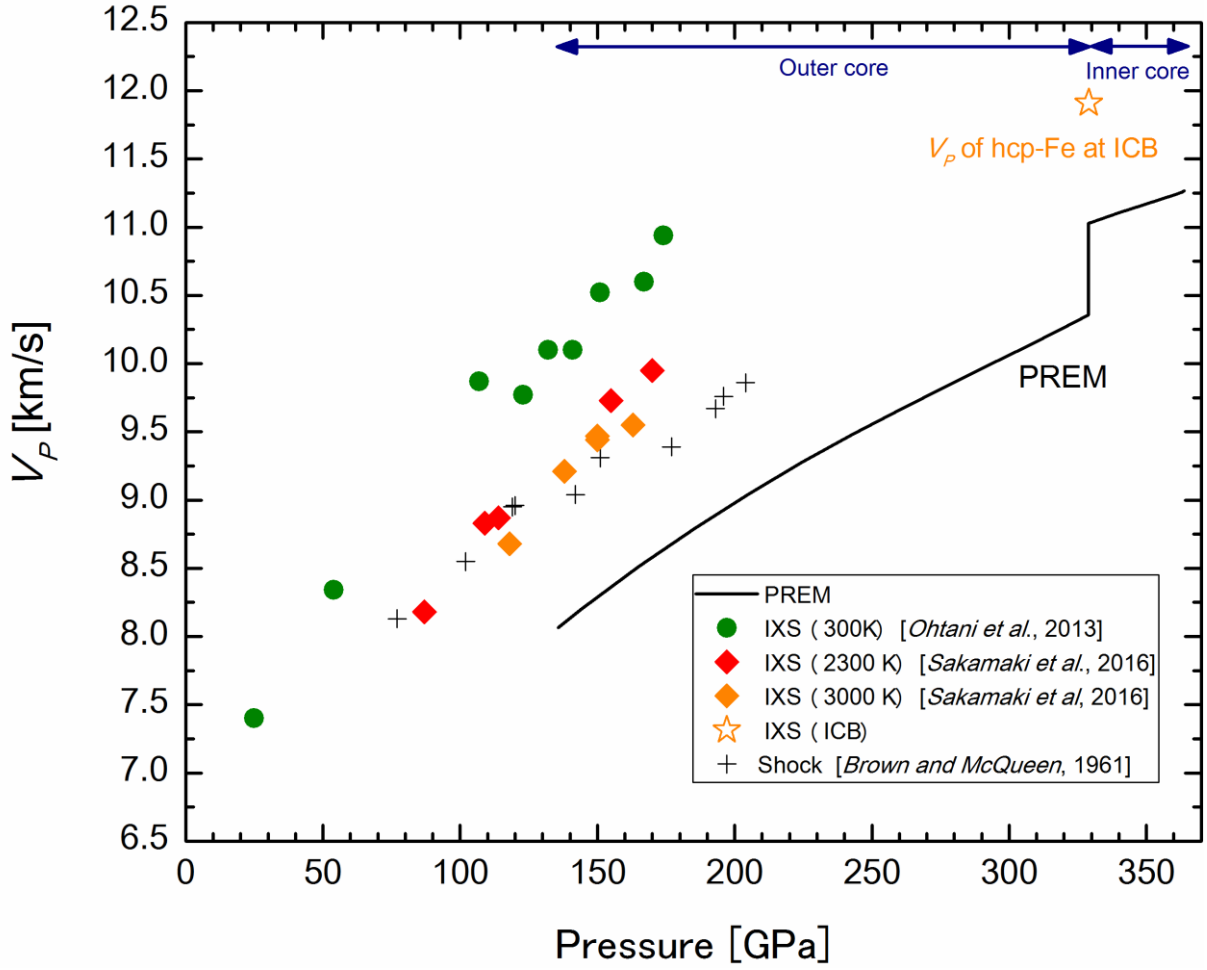

Fig. 1-2. The sound velocity (V_P) of Fe and that of PREM. The V_P of hcp-Fe based on IXS measurements at 300 K [*Ohtani et al.*, 2013] and at high temperature [*Sakamaki et al.*, 2016] were shown as solid symbols. The cross symbols show the V_P of Fe based on shockwave measurement [*Brown and McQueen*, 1961]. The black solid line represents the V_P of PREM [*Dziewonski and Anderson*, 1981]. The obtained V_P of Fe at ICB condition [*Sakamaki et al.*, 2016] was also shown as star symbol. The PREM has ~10% smaller sound velocity than pure iron at ICB condition.

so-called “light element”. Sulfur (S), silicon (Si), oxygen (O), carbon (C), and hydrogen (H) have been identified as the likely light elements [e.g., *Birch*, 1964; *Poirier*, 1994]. In this study, I focused on sulfur and silicon as light elements in the core because of following reasons.

S… Sulfur has been considered as plausible light element in the core because of its depletion in the mantle [*Murthy and Hall*, 1970]. In addition, iron sulfides are found universally in iron meteorites. Previous high pressure studies revealed that sulfur has large solubility in iron at low pressure and high pressures and it lowers the melting point of iron. It is consistent with early core formation and important for presence of liquid core.

Si… Silicon is one of major candidates as light element because of its large abundance in the Earth [e.g., *Birch*, 1964; *Ringwood*, 1959] and it also lowers the melting point of pure iron. The Earth’s mantle is depleted in silicon relative to chondritic material, which suggests silicon was partitioned to the core [e.g., *MacDonald and Knopoff*, 1958]. Previous high pressure partitioning experiments revealed that solubility of silicon into solid iron increased with increasing pressures and temperatures [*Takafuji et al*., 2005; *Sakai et al*., 2006].

As mentioned above, sulfur and silicon are both considered as light element components in the core of the Earth. Additionally, some geochemical studies and high-pressure experiments have predicted that sulfur and silicon could be present not only in the core of the Earth, but also in the core of other terrestrial planets such as Mars and Mercury [e.g., *Bertka and Fei*, 1998]. Some thermal evolution models indicate that Mars and Mercury has liquid outer core and any amount of sulfur and silicon in the core leads to liquid outer core. Therefore,

experimental study of the Fe–S–Si system provides us with key information to understand the properties of the planetary cores.

In this study, three experiments were performed to reveal the chemical and physical properties of the planetary cores. The melting relationships in the Fe–S–Si system were determined in order to discuss the crystallization of the core of the Mars and Mercury (Chapter 2). Secondary, partitioning behavior of light elements between metallic solid and liquid in the Fe–S–Si system was examined and the composition of the Earth's core was estimated (Chapter 3). Finally, sound velocity of Fe–Si alloy was determined based on IXS method and the amount of silicon in the Earth's inner core was discussed (Chapter 4).

1.4. References

Anderson, W. W., and T. J. Ahrens (1994), An equation of state for liquid iron and implications for the Earth's core. *J. Geophys. Res*. **99**, 4273–4284.

Antonangeli, D., T. Komabayashi, F. Occelli, E. Borissenko, A.C. Walters, G. Fiquet, and Y. Fei (2012), Simultaneous sound velocity and density measurements of hcp iron up to 93 GPa and 1100 K: An experimental test of the Birch's law at high temperature. *Earth Planet. Sci. Lett.* **331-332**, 210-214.

Bertka, C. M. and Y. Fei (1998), Density profile of an SNC model Martian interior and the moment-of inertia factor of Mars. *Earth Planet Sci. Lett.* **157**, 79–88.

Birch, F. (1952), Elasticity and constitution of the Earth's interior. *J. Geophys. Res*. **57**, 227–286.

Birch, F. (1964), Density and composition of mantle and core. *J. Geophys. Res*. **69**, 4377–4388.

Brown, J. M. and R. G. McQueen (1986), Phase transitions Grüneisen parameter and elasticity for shocked iron between 77 GPa and 400 GPa. *J. Geophys. Res*. **91**, 7485–7494.

Dewaele, A., P. Loubeyre, F. Occelli, M. Mezouar, P. I. Dorogokupets and M. Torrent (2006), Quasihydrostatic equation of state of iron above 2 Mbar. *Phys. Rev. Lett.* **97**, 215504–215507.

Dubrovinsky, L. S., S. K. Saxena, F. Tutti, S. Rekhi and T. LeBehan (2000), In-situ X-ray study of thermal expansion and phase transition of iron at multimegabar pressure. *Phys. Rev. Lett*. **84**, 1720–1723.

Dziewonski, A.M. and D.L. Anderson (1981), Preliminary reference Earth model, *Phys. Earth Planet. Inter*. **25**, 297–356.

Lin, j. F., V. V. Struzhkin, W. Sturhahn, E. Huang, J. Zhao, M. Y. Hu, E. E. Alp, H. K. Mao, N. Boctor, and R. J. Hemley (2003), Sound velocities of iron–nickel and iron–silicon alloys at high pressures. *Geophys. Res. Lett.* **30**, 2112.

Macdonald, G. J. F. and L. Knopoff (1958), On the chemical composition of the outer core. *Geophys. J. Roy. Astron. Soc.* **1(4)**, 284–297.

Mao, H. K., J. Xu, V. V. Struzhkin, J. Shu, R. J. Hemley, W. Strurhahn, M. Y. Hu, E. E. Alp, L. Vočadlo, D. Alfè, G. D. Price, M. J. Gillan, M. Schwoerer-Böhning, D. Häusermann, P. Eng, G. Shen, H. Giefers, R. Lübbers, and G. Wortmann (2001), Phonon density of states of iron up to 153 gigapascals. *Science* **292**, 914–916.

Murthy, V. R., and H. T. Hall (1970), The chemical composition of the Earth's core: Possibility of sulfur in the core. *Phys. Earth Planet. Inter*. **6**, 123–130.

Ohtani, E., Y. Shibazaki, T. Sakai, K. Mibe, H. Fukui, S. Kamada, T. Sakamaki, Y. Seto, S. Tsutsui, and A. Q. R. Baron (2013), Sound velocity of hexagonal close-packed iron up to core pressures. *Geophys. Res. Lett.* **40**, 5089–5094.

Poirier, J. P. (1994), Light elements in the Earth's outer core: a critical review, *Phys. Earth Planet. Inter.* **6**, 123–130.

Ringwood, A. E. (1959), On the chemical evolution and density of planets. *Geochim. Cosmochim. Acta.* **15**, 257–283.

Sakai, T., T. Kondo, E. Ohtani, H. Terasaki, N. Endo, T. Kuba, T. Suzuki and T. Kikegawa (2006), Interaction between iron and post-perovskite at core-mantle boundary and core signature in plume source region, *Geophys. Res. Lett.* **33**, L15317.

Sakamaki, T., E. Ohtani, H. Fukui, S. Kamada, S. Takahashi, T. Sakairi, A. Takahata, T. Sakai, S. Tsutsui, D. Ishikawa, R. Shiraishi, Y. Seto, T. Tsuchiya, and A. Q. R. Baron (2016), Constraints on the Earth's inner core composition inferred from measurements of the sound velocity of hcp-iron in extreme conditions, *Science Advances*, accepted.

Takafuji, N., K. Hirose, M. Mitome, and Y. Bando (2005), Solubilities of O and Si in liquid iron in equilibrium with (Mg, Fe)SiO_3 perovskite and the light elements in the core, *Geophys. Res. Lett.* **32**, L06313.

Chapter 2:

Melting relationships in the Fe-S-Si system at high pressure and temperature

2.1. Introduction

The Earth's core is mainly composed of an iron alloy, with light elements also required in the core to account for the core density deficit [*Birch*, 1964]. Sulfur, silicon, oxygen, carbon, and hydrogen have been identified as the likely light elements [e.g., *Poirier*, 1994]. Alloying with light elements significantly affects the physical properties of iron and depresses its melting temperature [e.g., *Boehler*, 1996; *Lin et al*., 2002]. There are significant implications for the chemical composition and thermal structure of the Earth's core as a corollary. The melting temperature of an iron alloy is important information for estimating the temperature at the inner–outer core boundary (ICB) of the terrestrial planets. An investigation of high-pressure phases of iron alloys also helps us to understand the structure of the solid inner core. Among the candidate light elements in the core, sulfur and silicon are considered as major light element components based on geochemical models [e.g., *Allégre et al.*, 1995; *Javoy,* 1995] and high-pressure partitioning experiments [e.g., *Hillgren et al*., 2000; *Sakai et al.*, 2006]. Additionally, some geochemical studies and high-pressure experiments have predicted that sulfur and silicon could be present in the cores of other terrestrial planets such as Mars and Mercury [e.g., *Bertka and Fei*, 1998].

Previous high-pressure studies revealed that sulfur and silicon had different effects on the properties of iron alloys. In the Fe–FeS system, Fe_3S_2, Fe_2S, and Fe_3S have been reported as intermediate phases [e.g., *Fei et al*., 1997, 2000; *Li et al*., 2001], and ε-Fe and Fe_3S are stable as the subsolidus phases up to the core conditions. The eutectic temperature in the Fe–Fe_3S system was measured up to 180 GPa using a diamond anvil cell (DAC) [e.g., *Kamada et al*., 2010, 2012; *Morard et al.*, 2008]. It was revealed that the melting temperature of iron is

significantly depressed by the effect of sulfur, and the hcp-Fe phase coexists with partial melts between the solidus and liquidus temperatures. The amount of sulfur in the solid iron increases with increasing pressure at the eutectic temperature [e.g., *Kamada et al*., 2010, 2012; *Li et al.*, 2001]. Information about the amount of sulfur in solid iron is important to understand the chemical properties of the inner core.

Silicon has a high solubility into iron and forms a solid solution with iron at high pressure [e.g., *Kuwayama and Hirose*, 2004], with the solubility of silicon into solid iron increasing with increasing pressure and temperature [e.g., *Kuwayama et al*., 2009]. The high-pressure phase relations of the Fe–Si alloy have been studied using a DAC and it was found that the subsolidus phases of the Fe–Si alloy are related to the amount of silicon in the iron alloy [e.g., *Asanuma et al*., 2008; *Fischer et al.*, 2013; *Lin et al*., 2002]. *Asanuma et al.* [2008; 2011] reported that the stability of hcp + fcc phases broadens by dissolving silicon in iron alloy and the hcp phase is stable at least up to 252 GPa in $Fe_{0.93}Si_{0.07}$ alloy. The melting temperature of Fe–Si alloy was determined up to 119 GPa by laser-heated DAC (LHDAC) experiments and it was revealed that the effect of silicon on the melting temperature of iron alloy is smaller than that of sulfur [*Asanuma et al*., 2010].

In spite of the importance of the effect of both sulfur and silicon on the physical properties of iron alloy, there are few studies about the melting relations of the Fe–S–Si ternary system. Although some previous studies on closure of the Fe–S–Si liquid immiscibility gap have been reported by *Sanloup and Fei* [2004] and *Morard and Katsura* [2010], their experiments were carried out by using a multianvil apparatus at pressures below 25 GPa and the details of higher pressure phase relationships and melting temperatures in the system were not revealed. Therefore, it is desirable to extend the experimental condition as close as possible to conditions of the planetary core. The phase and melting relationships in the Fe–S–Si system

have been investigated up to 60 GPa using a LHDAC combined with an X-ray diffraction technique. The results provide important clues for understanding the properties of the cores of Earth, Mars, and Mercury.

2.2. Experimental procedure

2.2.1. Sample preparation

High pressure was generated by a symmetric-type DAC. The culet sizes of the diamond anvils were 300, 250, or 100 μm, depending on the desired experimental pressures. The starting material was composed of a powder mixture of Fe (99.9%; Wako Pure Chemical Industries, Ltd), FeS (99.9% purity; Rare Metallic Co., Ltd) and FeSi (99.9% purity; Rare Metallic Co., Ltd), which was ground in an agate mortar in order to homogenize the starting materials. The typical grain size of the starting mixture was 1–5 μm, which was confirmed by using a scanning electron microscope (SEM; JEOL JSM-5410). The sample compositions used in this study were $Fe_{80.1}S_{12.7}Si_{7.2}$ (Fe-8wt.%S-4wt.%Si) and $Fe_{74.4}S_{18.5}Si_{7.1}$ (Fe-12wt.%S-4wt.%Si), which have been proposed to explain the density deficit in the Earth's core [e.g., *Chen et al*., 2007]. Additionally, this composition might be close to the composition of Mercury's core, which might contain several wt. % silicon in addition to sulfur as was suggested by previous high-pressure experiments under reducing condition [e.g., *Maravergne et al*., 2004]. I made a thin foil of starting materials using a cold compression technique. For the in situ experiments, the sample foil was sandwiched between NaCl pellets, which worked as a pressure medium, thermal insulator, and pressure marker. These samples were loaded into a sample hole in a precompressed SUS304 or Re gasket, which was typically about 30–50 μm in thickness. Before loading the sample, I checked the homogeneity of the sample by using high-resolution reflection microscope and selected only homogeneous pieces of the mixture foil. Starting

materials, pressure medium, and pressure scales used in this study were summarized in Table 2-1.

First, the sample was compressed to a target pressure at room temperature, and then annealed at around 1500 K for about 10 min to synthesize solid phases and to reduce stress in the cell assemblages. The sample was heated using the double-sided laser heating method [*Shen et al.*, 1996] employing a high-power Nd:YAG laser or fiber laser. Temperatures were determined by fitting the emission spectra from the heated sample to the grey body formula. The emission spectra was fitted to the Plank radiation function,

$$I = \frac{c_1 \varepsilon(\lambda) \lambda^{-5}}{\exp(c_2 / \lambda T) - 1} \tag{2-1}$$

where I is the spectral intensity, c_1 is the first radiation constant, $\varepsilon(\lambda)$ is emissivity, λ is the wavelength of an emission light, c_2 is the second radiation constant, and T is the temperature of the sample. c_1 was treated as a parameter (c_1') because the absolute intensity of emission spectrum is not able to be measured. The wavelength and temperature dependence of the emissivity were assumed to be $\varepsilon(\lambda) = a\lambda + b$. The parameters ($a$, b, c_1', T) were sought by fitting to the emission spectra from the sample. The ranges of wavelength of collected spectra from the samples were typically from 600 to 800 nm. Radiation from the heated sample was collected for time durations between 0.5 and 3 s for analyzing the temperature. The temperature measurements were performed for several tens of seconds during heating. The experimental temperature was determined as an average of the measured temperature over several tens of seconds. The temperature fluctuation during the experiments was approximately 50–100 K. The experimental pressure was determined from the lattice parameters of NaCl using the equation of states (EOS) of B1 phase [*Brown*, 1999] and B2 phase [*Fei et al.*, 2007] of NaCl. The experimental pressure at high temperature was assumed to be $P_{HT} = P_{300K} + \Delta P_{th}$. P_{300K} is a

Table 2-1
Starting materials, pressure medium, and pressure scale used.

Run numnber	starting material	Pressure medium	Pressure scale
FESSI09	Fe-8wt.%S-4wt.%Si	NaCl powder	NaCl (B2) [*Fei et al*., 2007]
FESSI10	Fe-8wt.%S-4wt.%Si	NaCl powder	NaCl (B2) [*Fei et al*., 2007]
FESSI19	Fe-12wt.%S-4wt.%Si	NaCl powder	NaCl (B1) [*Brown*, 1999]
FESSI20	Fe-12wt.%S-4wt.%Si	NaCl powder	NaCl (B2) [*Fei et al*., 2007]
FESSI27	Fe-8wt.%S-4wt.%Si	NaCl powder	NaCl (B1) [*Brown*, 1999]
FESSI36	Fe-8wt.%S-4wt.%Si	NaCl powder	NaCl (B2) [*Fei et al*., 2007]

pressure at room temperature based on the third-order Birch–Murnaghan equation of state, and ΔP_{th} is a thermal pressure based on the Mie–Grüneisen relation:

$P_{th} = \gamma / V[E(T,\theta_D) - E(300K,\theta_D)]$, where $\gamma = \gamma_0 (V/V_0)^q$ and $\theta_D = \theta_0 (V/V_0)^{-\gamma}$, respectively. The parameters of the EOS of NaCl are summarized in *Brown* [1999] and *Fei et al.* [2007]. The temperature of the NaCl was considered to be the same as the temperature of the sample. The EOS of iron was not used to calculate experimental pressure in this study because incorporation of silicon or sulfur into solid iron may expand the unit cell volume of iron [e.g., *Hirao et al.*, 2004]. The error in pressure was evaluated from the error in volume of NaCl and the error in temperature was determined from the standard deviation of the fluctuation of the measured temperatures.

2.2.2. In situ X-ray diffraction experiments

In situ X-ray diffraction experiments were conducted at the BL10XU beamline of the SPring-8 facility [*Ohishi et al.*, 2008]. I used a monochromatic X-ray beam with a typical wavelength of 0.4136(3) Å and it was collimated to a diameter of 15 μm. The beam size was smaller than the size of the laser heating area, which was approximately 30–40 μm across. I checked the X-ray position by X-ray fluorescence of diamonds before heating. Therefore, X-ray and heating areas were aligned well. The melting detection in this study was based on disappearance of the X-ray diffraction peaks, which is same as in previous melting studies [e.g., *Kamada et al.*, 2010, 2012; *Terasaki et al.*, 2011]. An imaging plate (IP: Rigaku R-AXIS IV) or an X-ray charge-coupled device (CCD: Brucker AXS, SMART APEX) were used as X-ray detectors. Typical exposure time used for taking diffraction patterns was 1 s for the CCD detector or 3 min for the IP detector for each run. At high temperatures, the sample diffraction patterns were collected using the CCD detector because it is important to take a diffraction

pattern within a short duration of time to detect melting of the sample. The diffraction patterns of the sample were recorded at room temperature and in the temperature ranges between 1350 and 2270 K in 50–100 K steps at each pressure. After I observed disappearance of the X-ray diffraction peaks of Fe_3S, the laser power was shut down to quench the sample. The reappearance of X-ray diffraction peaks of Fe_3S in the quenched sample was checked, suggesting the disappearance of peaks from Fe_3S at high temperatures was because of the sample melting, but not because of migration from the heating spot of the sample. The diffraction patterns were analyzed using the IP Analyzer software package and the PD Indexer software package programmed by Y. Seto [*Seto et al*., 2010].

2.3. Results

2.3.1. Subsolidus phases in the Fe–S–Si system

The experimental conditions and the observed phases are summarized in Table 2-2. In situ X-ray diffraction experiments were conducted in the pressure range of 20.8 to 61 GPa and the temperature range of 300 to 2270 K. In all the explored pressure ranges, the diffraction peaks of the fcc (γ) phase, and/or the hcp (ε) phase, and Fe_3S were observed under the subsolidus conditions of this study for the two starting compositions of $Fe_{80.1}S_{12.7}Si_{7.2}$ (Fe-8wt.%S-4wt.%Si) and $Fe_{74.4}S_{18.5}Si_{7.1}$ (Fe-12wt.%S-4wt.%Si), as shown in Table 2-2. The diffraction peaks of the fcc and hcp phases were derived from the Fe–Si alloy. Fe_3S, which has been reported as an intermediate phase in the Fe–FeS system [e.g., *Fei et al*., 2000], appeared as a result of a reaction between Fe and FeS. Other possible phases in the Fe–FeS system, such as Fe_2S and Fe_3S_2, were not observed in this study. In this study, because of dissolution of silicon into Fe, the boundary of fcc and hcp phases shifted towards higher pressures compared to that of pure Fe [e.g., *Anzellini et al*., 2013; *Ma et al*., 2004]. Previous studies of the Fe–FeSi

Table 2-2
Experimental conditions and results.

Run number	P [a] [GPa]	T [K]	Observed phases
Fe-8wt.%S-4wt.%Si			
FESSI09_004	58.2(41)	1450(50)	hcp, fcc, Fe_3S, NaCl(B2)
FESSI09_007	59.2(44)	1490(50)	hcp, fcc, Fe_3S, NaCl(B2)
FESSI09_008	59.3(45)	1580(50)	hcp, fcc, Fe_3S, NaCl(B2)
FESSI09_009	60.5(40)	1700(50)	hcp, fcc, Fe_3S, NaCl(B2)
FESSI09_010	59.8(39)	1810(50)	hcp, fcc, Fe_3S, NaCl(B2)
FESSI09_011	59.5(41)	1830(50)	hcp, fcc, Fe_3S, NaCl(B2)
FESSI09_012	60.0(39)	1870(50)	fcc, NaCl(B2)
FESSI09_013	58.1(3)	300	hcp, fcc, Fe_3S, NaCl(B2)
FESSI10_015	54.8(15)	300	hcp, fcc, Fe_3S, NaCl(B2)
FESSI10_016	57.4(43)	1520(50)	hcp, fcc, Fe_3S, NaCl(B2)
FESSI10_017	57.4(49)	1560(50)	hcp, fcc, Fe_3S, NaCl(B2)
FESSI10_018	58.2(45)	1650(50)	hcp, fcc, Fe_3S, NaCl(B2)
FESSI10_019	58(45)	1675(50)	hcp, fcc, Fe_3S, NaCl(B2)
FESSI10_020	57.7(45)	1740(50)	hcp, fcc, Fe_3S, NaCl(B2)
FESSI10_022	56.6(47)	1780(50)	hcp, fcc, Fe_3S, NaCl(B2)
FESSI10_023	56.3(44)	1800(50)	hcp, fcc, Fe_3S, NaCl(B2)
FESSI10_024	54.2(39)	1810(50)	hcp, fcc, Fe_3S, NaCl(B2)
FESSI10_025	54.3(41)	1840(50)	hcp, NaCl(B2)
FESSI10_026	53.9(44)	1880(50)	hcp, NaCl(B2)
FESSI10_030	49.2(6)	300	hcp, fcc, Fe_3S, NaCl(B2)
FESSI27_012	20.9	300	hcp, fcc, Fe_3S, NaCl(B1)
FESSI27_013	20.6	1275(50)	hcp, fcc, Fe_3S, NaCl(B1)
FESSI27_014	20.6	1310(50)	hcp, fcc, Fe_3S, NaCl(B1)
FESSI27_015	20.5	1460(50)	hcp, fcc, Fe_3S, NaCl(B1)
FESSI27_020	20.5	1520(50)	hcp, fcc, NaCl(B1)
FESSI27_021	21.1	300	hcp, fcc, Fe_3S, NaCl(B1)
FESSI27_028	20.8	1760(50)	hcp, fcc, NaCl(B1)
FESSI27_029	20.7	1950(50)	NaCl(B1)
FESSI27_030	20.8	300	hcp, fcc, Fe_3S, NaCl(B1)

FESSI36_002	30.8(3)	300	hcp, fcc, Fe_3S, NaCl(B2)
FESSI36_003	32.5(36)	1430(50)	hcp, fcc, Fe_3S, NaCl(B2)
FESSI36_004	32.4(34)	1500(50)	hcp, fcc, Fe_3S, NaCl(B2)
FESSI36_005	32.6(36)	1550(50)[c]	hcp, fcc, Fe_3S, NaCl(B2)
FESSI36_006	33.2(36)	1660(50)[c]	hcp, fcc, Fe_3S, NaCl(B2)
FESSI36_007	34.5(40)	1790(50)	hcp, fcc, NaCl(B2)
FESSI36_008	32.8(37)	1840(50)	hcp, fcc, NaCl(B2)
FESSI36_009	32.1(51)	1910(50)[c]	fcc, NaCl(B2)
FESSI36_010	33.8(45)	2010(50)[c]	NaCl(B2)
FESSI36_011	33.9(42)	2030(80)	NaCl(B2)
FESSI36_012	30.7(3)	300	hcp, fcc, Fe_3S, NaCl(B2)
FESSI36_026	51.1(8)	300	hcp, fcc, Fe_3S, NaCl(B2)
FESSI36_027	49.5(34)	1620(50)	hcp, fcc, Fe_3S, NaCl(B2)
FESSI36_028	49.5(40)	1865(50)[c]	hcp, fcc, Fe_3S, NaCl(B2)
FESSI36_029	49.4(47)	2150(50)[c]	hcp, fcc, NaCl(B2)
FESSI36_030	50.7(50)	2270(60)	NaCl(B2)
FESSI36_031	47.5(2)	300	hcp, fcc, Fe_3S, NaCl(B2)
FESSI36_032	55.0(5)	300	hcp, fcc, Fe_3S, NaCl(B2)
FESSI36_034	58.3(49)	2170(50)	NaCl(B2)
FESSI36_035	55.2(3)	300	hcp, fcc, Fe_3S, NaCl(B2)
Fe-12wt.%S-4wt.%Si			
FESSI19_005	24.9(1)	300	hcp, fcc, Fe_3S, NaCl(B1,B2)
FESSI19_006	26.4(26)	1350(50)	hcp, fcc, Fe_3S, NaCl(B1,B2)
FESSI19_007	26.9(28)	1410(50)	hcp, fcc, Fe_3S, NaCl(B1,B2)
FESSI19_008	26.3(27)	1390(50)	hcp, fcc, Fe_3S, NaCl(B1,B2)
FESSI19_009	26.6(29)	1470(50)	hcp, fcc, Fe_3S, NaCl(B1,B2)
FESSI19_013	27.1(29)	1460(50)	hcp, fcc, Fe_3S, NaCl(B1,B2)
FESSI19_014	27.3(33)	1610(75)	hcp, NaCl(B1,B2)
FESSI19_016	24.4(1)	300	hcp, fcc, Fe_3S, NaCl(B1,B2)
FESSI20_002	42.1(4)	300	hcp, Fe_3S, NaCl(B2)
FESSI20_003	43.7(26)	1345(50)	hcp, Fe_3S, NaCl(B2)
FESSI20_004	43.9(31)	1450(50)	hcp, Fe_3S, NaCl(B2)
FESSI20_005	43.8(31)	1480(50)	hcp, Fe_3S, NaCl(B2)
FESSI20_006	43.7(31)	1500(50)	hcp, Fe_3S, NaCl(B2)
FESSI20_007	43.8(32)	1570(50)	hcp, Fe_3S, NaCl(B2)

FESSI20_008	44.1(35)	1650(50)	hcp, Fe_3S, NaCl(B2)
FESSI20_013	44.1(38)	1730(50)	hcp, NaCl(B2)
FESSI20_015	42.2(3)	300	hcp, fcc, Fe_3S, NaCl(B2)

The numbers in parentheses show errors and last two digit.

The melting of the sample was detected by disappearance of diffraction pattern.

[a]The pressures are based on the EOS of NaCl(B1) [*Brown*, 1999] and NaCl(B2) [*Fei et al*., 2007].

[b]hcp and fcc represent the structure of Fe-Si alloy, respectively.

[c]The temperatures are estimated by the laser power.

system [e.g., *Asanuma et al*., 2008] reported that silicon expanded the stability field of the fcc phase of Fe alloy, and the Fe–Si alloy had a wide stability field of coexistence of hcp and fcc phases; this is consistent with the results of this study.

2.3.2. Solidus and liquidus temperature in the Fe–S–Si system

Both the solidus and liquidus temperatures were determined up to 61 GPa by using the X-ray diffraction patterns of the starting sample of $Fe_{80.1}S_{12.7}Si_{7.2}$, whereas only the solidus temperature was determined for the starting sample of $Fe_{74.4}S_{18.5}Si_{7.1}$. The solidus temperatures for the two compositions were in good agreement with each other. Changes in the diffraction patterns due to melting of Fe_3S and Fe–Si alloys were observed, as shown in Fig. 2-1(a) A–D. The 2D images of the same diffraction patterns are shown as supplementary materials in Fig. 2-2 (a). Fig. 2-1(a) A shows the diffraction pattern of fcc/hcp Fe–Si alloy and Fe_3S taken at 59.2 GPa and 1490 K. The diffraction peaks from fcc/hcp Fe–Si alloy and Fe_3S weakened when the sample was heated to 1830 K (Fig. 2-1(a) B). Both the X-ray diffraction peaks of hcp Fe–Si alloy and Fe_3S disappeared at 1870 K, although the peaks of fcc Fe–Si alloy still remained in the diffraction pattern (Fig. 2-1(a) C). After quenching, the peaks of hcp Fe–Si alloy and Fe_3S reappeared (Fig. 2-1(a) D) due to crystallization from the melt. Although I could not observe diffuse scattering peaks from the melt in most runs except those made at low pressure around 10 GPa, this observation of the peak disappearance during heating and reappearance of the peaks after quenching implies strong evidence for melting of the sample. Similarly, Fe_3S disappeared first from the diffraction peaks, and fcc/hcp Fe–Si phases were observed at a higher temperature in the other runs. Disappearance of the diffraction peaks of Fe_3S was observed at 27, 44, 54, and 60 GPa. The determination of the solidus curve was also confirmed by texture observations of the recovered sample in a separate run, as shown in Fig. 2-3. The dendritic

quench texture of the recovered sample in this figure, which shows clear evidence for melting of the run product, is consistent with the melting curve determined by *in situ* X-ray diffraction experiments. Figure 2-1(b) A-D shows similar changes in diffraction profiles obtained in the pressure range of 49.2–58 GPa. The diffraction peaks of fcc/hcp Fe–Si alloy and Fe_3S were observed under subsolidus conditions at 58 GPa and 1650 K. The X-ray diffraction peaks of Fe_3S weakened with increasing temperature to 1810 K (B) and disappeared at 1840 K and 54 GPa (C). After quenching, the peaks of fcc/hcp Fe–Si alloy and Fe_3S reappeared (D). The 2D images of the same diffraction profiles are given in the supplementary materials (Fig. 2-2 (b)).

We observed the disappearance of the diffraction peaks from fcc/hcp Fe–Si alloy and Fe_3S. This disappearance suggests that total melting occurred in the Fe–S–Si system at 21, 34, 51, and 58 GPa for the bulk composition of $Fe_{80.1}S_{12.7}Si_{7.2}$ (Table 2-2).

Melting of Fe_3S corresponds to the solidus temperature, and the complete disappearance of both fcc/hcp Fe–Si alloy and Fe_3S corresponds to the liquidus temperature of the Fe–S–Si system. Based on these melting sequences, the phase relationships of the Fe–S–Si system are drawn in Fig. 2-4. Both the solidus and liquidus temperatures increase with increasing pressure. This criterion for determination of melting was also used by *Terasaki et al*. [2010] and melting was also confirmed by the observation of the quench textures of dendrite in the recovered samples after quenching at high pressure and temperature. The compositional change in the Fe–S–Si system with pressure and temperature is very important. However, the measurement of the compositions of the phases was very limited in this work due to technical difficulties. I used NaCl as the pressure medium and pressure marker, however, the samples in the NaCl pressure medium were difficult to recover due to its large deformation during decompression and recovery. Recovery experiments were conducted using alumina pressure medium. The composition of coexisting crystalline phases was analyzed in a run conducted at

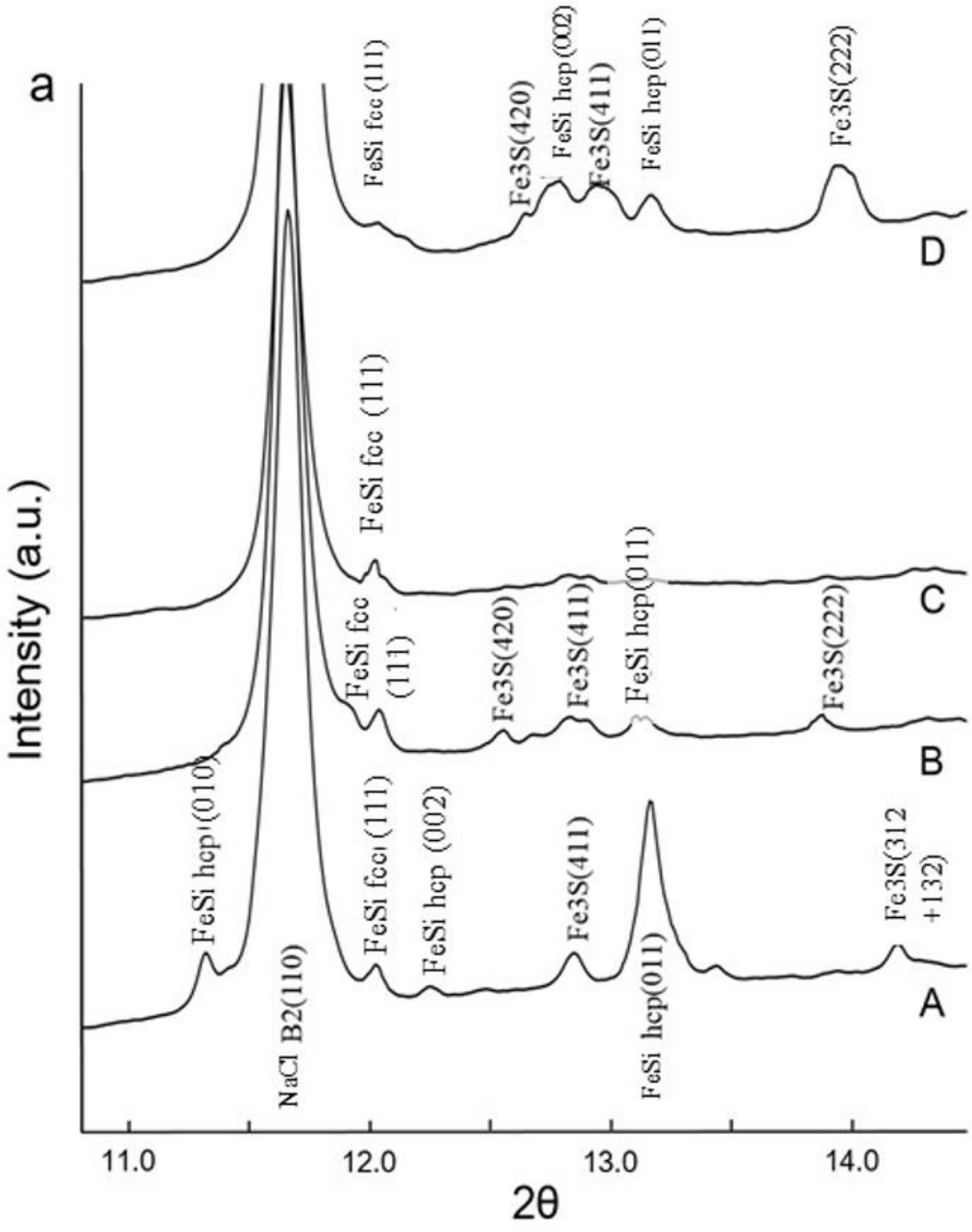

Fig. 2-1. (a) Diffraction patterns of the Fe–S–Si system at 42.2–44 GPa (Run FESSI20). A at 44(3) GPa and 1450(50) K, B at 44(4) GPa and 1650(50) K, C at 44(4) GPa and 1730(50) K, and D at 42.2(3) GPa and 300 K after quenching from 1730 K. NaCl was used as the pressure medium and thermal insulator. The X-ray diffraction pattern of Fe_3S and hcp-Fe–Si alloy disappeared at 1730 K due to the partial melting of samples. The X-ray diffraction peaks of Fe_3S reappeared after quenching. Abbreviations: NaCl B2, B2 phase of NaCl; FeSi hcp, hcp-phase of Fe–Si alloy; FeSi fcc, fcc-phase of Fe–Si alloy; Fe_3S, Fe_3S phase. The 2D images of the same diffraction profiles are given in Fig. 2-2(a).

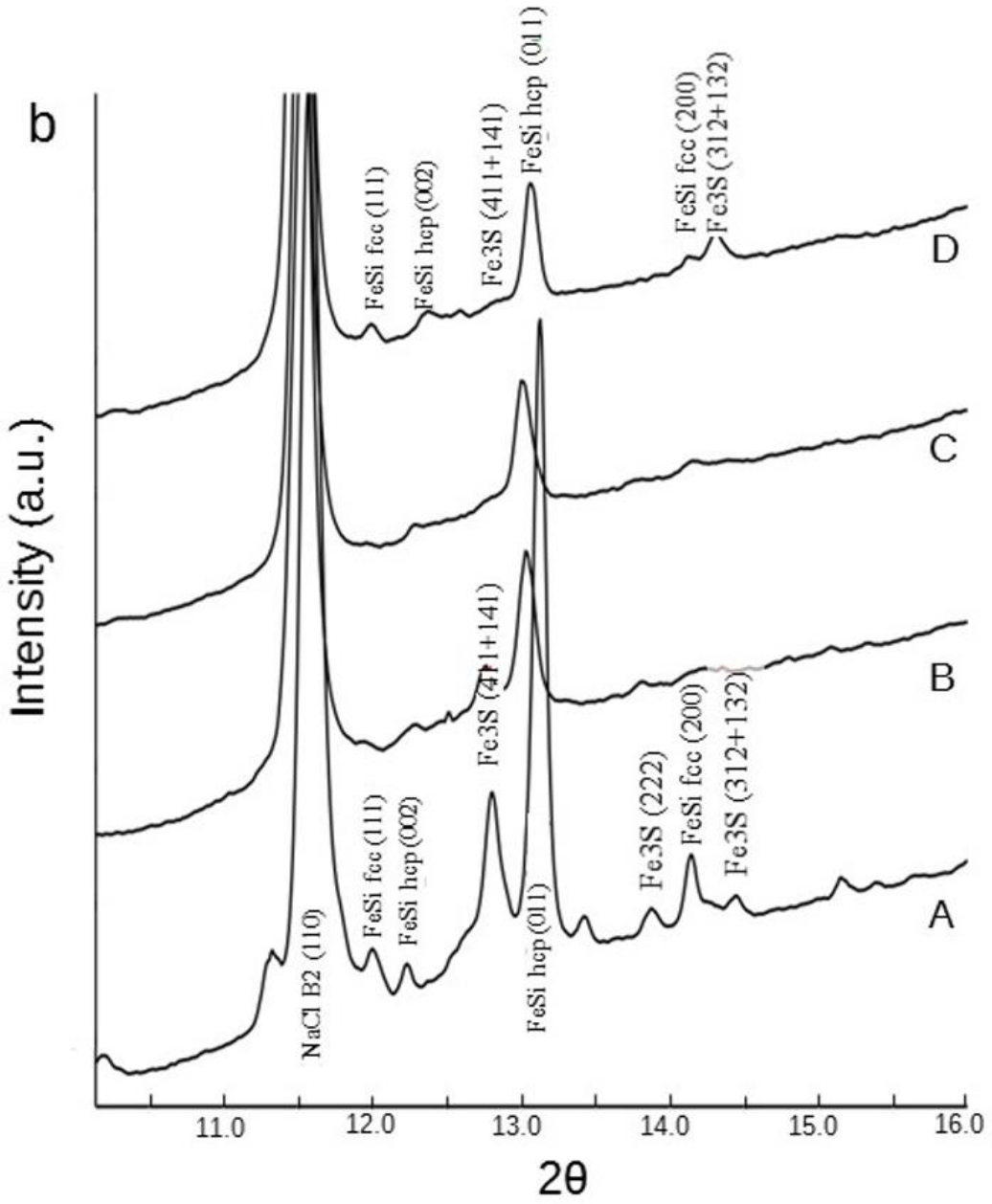

Fig. 2-1. (b) Typical example of diffraction patterns of the Fe–S–Si system at 49.2–58 GPa (FESSI10). A at 58(5) GPa and 1650(50) K, B at 54(4) GPa and 1810(50) K, C at 54(4) GPa and 1840(50) K, and D at 49.2(6) GPa and 300 K after quench from 1840 K. The X-ray diffraction pattern of Fe_3S disappeared at 1840 K due to partial melting of the sample. The X-ray diffraction pattern of Fe_3S and fcc-Fe–Si alloy reappeared after quenching. Abbreviations are the same as those of Figure 2-1(a). The 2D images of the same diffraction profiles are given in Fig. 2-2(b).

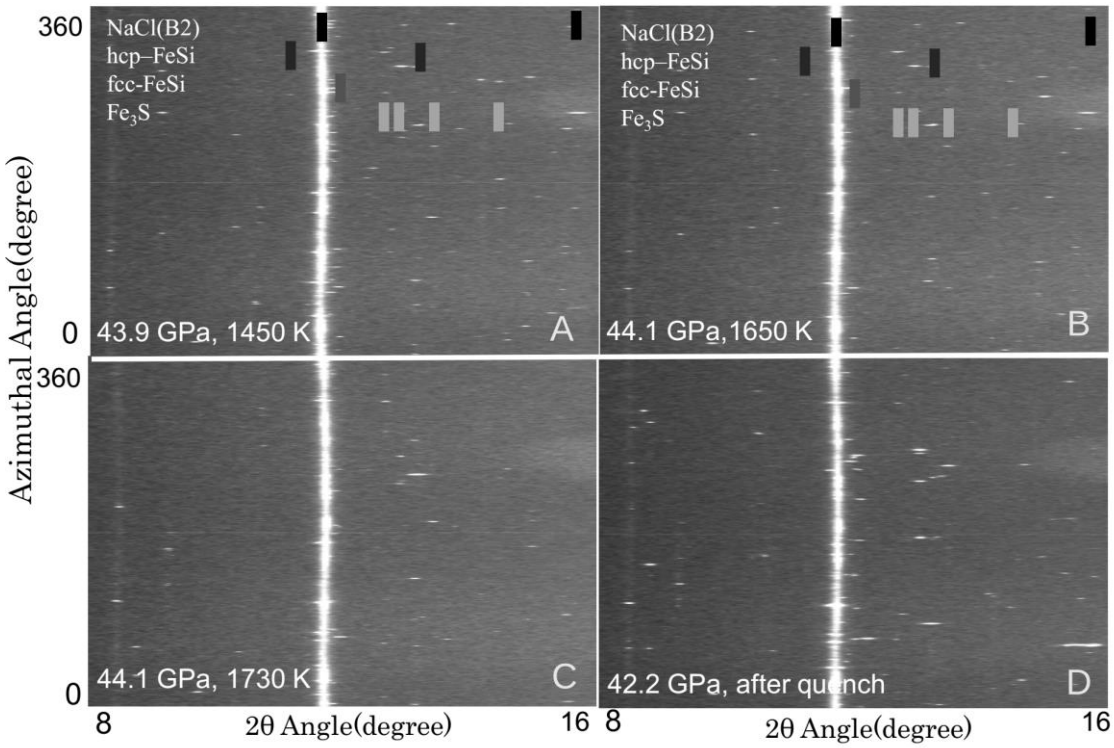

Fig. 2-2. (a) 2D images of diffraction patterns of the Fe–S–Si system at 42.2–44 GPa (Run FESSI20) corresponding to the X-ray profile given in Figure 2-1(a). A at 44(1) GPa and 1450(50) K, B at 44(4) GPa and 1650(50) K, C at 44(4) GPa and 1730(50) K, and D at 42.2(0.3) GPa and 300 K after quenching from 1730 K. NaCl was used as the pressure medium and thermal insulator.

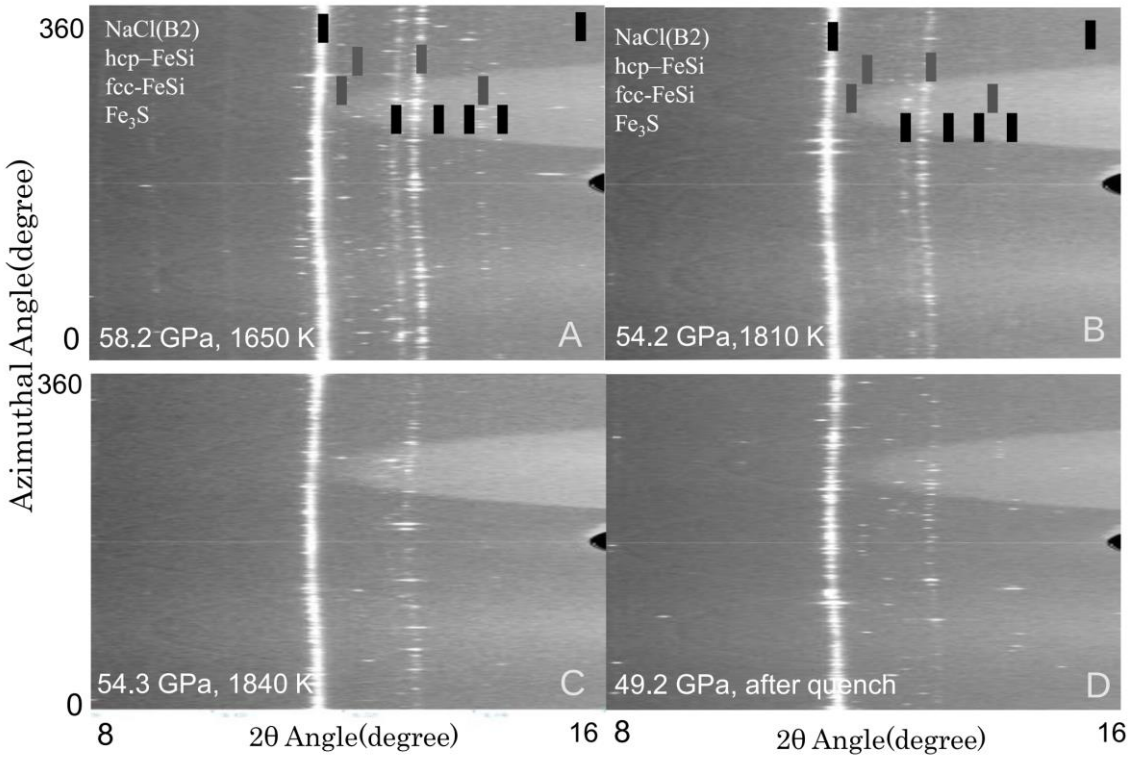

Fig. 2-2. (b) 2D images of diffraction patterns of the Fe-S-Si system at 49.2-58 GPa (Run FESSI10) corresponding to the X-ray profile given in Figure 2-1(b). A at 58(5) GPa and 1650(50) K, B at 54(4) GPa and 1810(50) K, C at 54(4) GPa and 1840(50) K, and D at 49.2(0.6) GPa and 300 K after quenching from 1840 K.

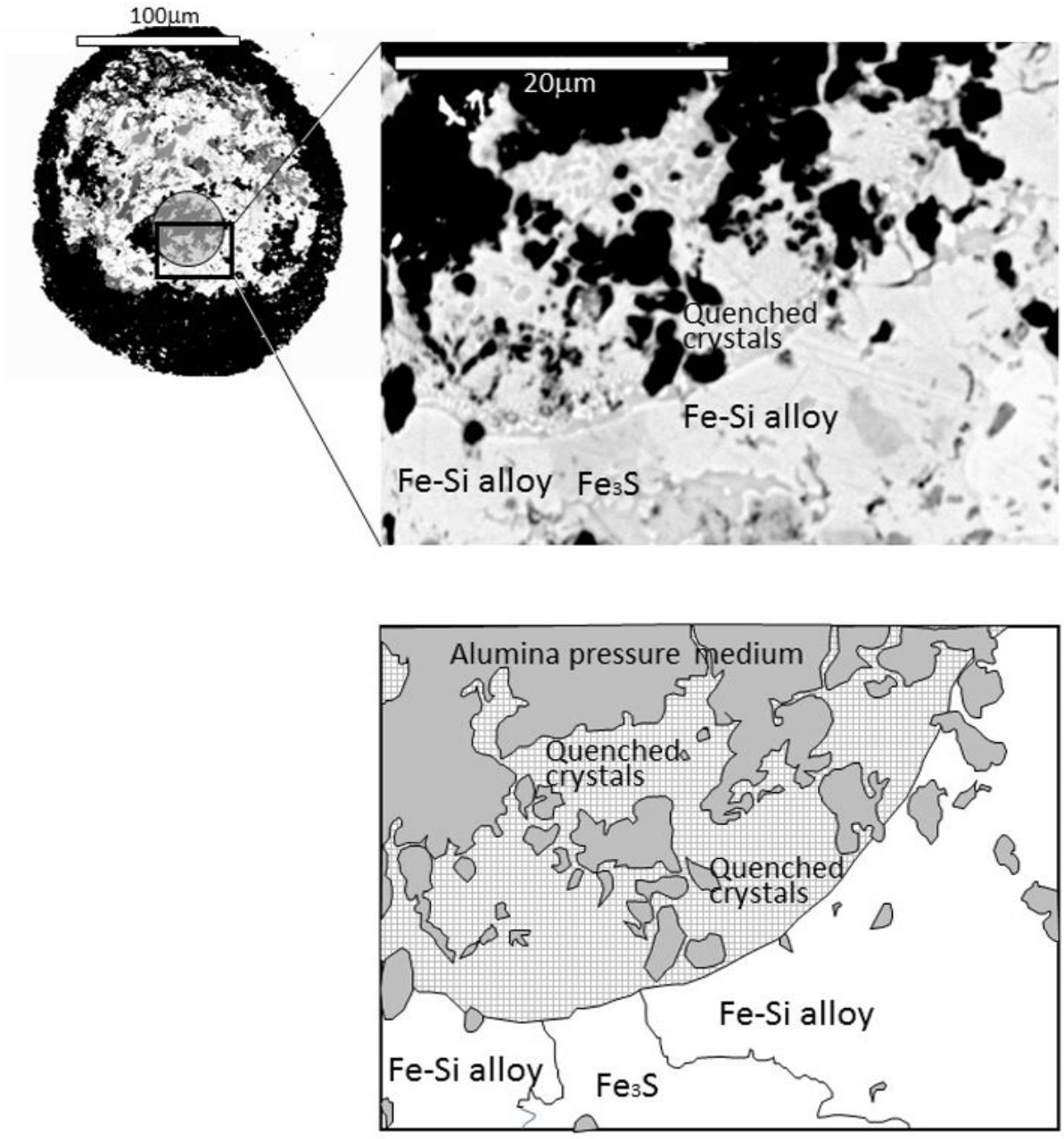

Fig. 2-3. Back-scattered electron image (BSE) of the quench textures of the melting experiment. The sample was recovered from 58(4) GPa and 1940(110). The experimental conditions are shown as a gray circle in the phase diagram given in Figure 2-4. A zoom-out image of the sample in DAC is shown in this figure. The diameter of laser beam is around 40 μm and is shown as a grey circle in the figure. The detailed textures of the zoom-in image are also sketched at the bottom of the BSE image. A dendritic texture showing quenching from the melt is clearly observed in the BSE image and shown as hatched areas in the sketch. The black grains in the zoom-in and zoom-out images are alumina grains used for the pressure medium. It was difficult to remove them from the sample during surface polishing.

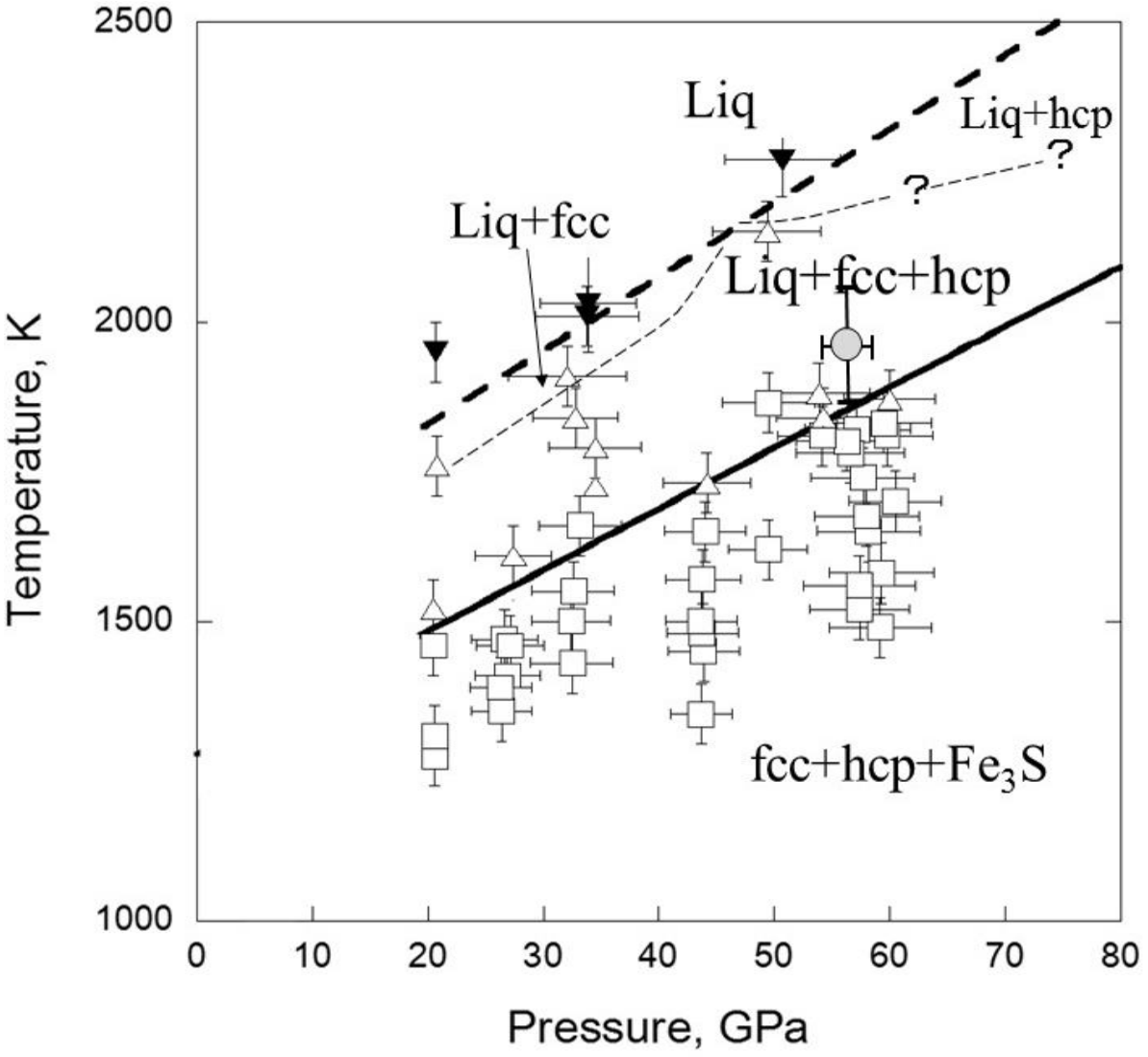

Fig. 2-4. Phase diagram of the Fe–S–Si system in this study. Open squares show the coexistence of Fe–Si alloys (fcc+hcp) and Fe_3S detected by X-ray diffraction experiments. The open triangles show partial melting, and the solid triangles show total melting above the liquidus detected by the disappearance of X-ray diffraction patterns of the crystalline phases. The fcc phase appears as the liquidus phase at least up to 32 GPa. The bold solid and dashed lines show the solidus and liquidus curves fitted by Simon's equation. The pressure and temperature condition of partial melting based on the quenched texture observation of the recovered sample (Figure 2-3) is shown as a gray circle.

58(4) GPa and 1940(110) K. The analyses revealed that the Si content was approximately 12.4 at. % in the metallic Fe–Si phase in the periphery of the laser spot of the recovered sample from 58(4) GPa and 1940(110) K conditions, whereas it was only 0.4 at. % in the Fe_3S phase adjacent to the Fe–Si alloy. Further work is needed for determination of the compositional variation among coexisting phases in this system with pressure and temperature.

2.4. Discussion

2.4.1. Comparisons with previous melting curves

The solidus and liquidus curves were fitted by the Simon equation [*Simon and Glatzel*, 1929], $T_m = T_m^R \times \left(\frac{P - P^R}{a} + 1 \right)^{\frac{1}{c}}$, as adopted by previous studies [e.g., *Asanuma et al*., 2010; *Terasaki et al*., 2011], where T_m is the melting temperature in kelvins at an experimental pressure (P) in GPa, T_m^R is the melting temperature at a reference pressure, and P^R, a and c are fitting parameters. The parameters fitted are T_m^R=1432(6), a=122(2), and c=1.10(2) for the solidus and T_m^R =1768(13), a=145 (5), and c=0.99(3) for the liquidus assuming the reference pressure of P^R=15GPa. When I assume the reference pressure of P^R=0 GPa, the parameters fitted are T_m^R=1277(6), a=116.1(21), and c=1.06(2) for the solidus and T_m^R =1582(13), a=127.9(48), and c=1.00(3) for the liquidus. The solidus and liquidus curves with different reference pressures are nearly the same, and the reference pressures do not affect the following discussions.

Sulfur and silicon are candidates for the light elements in the cores of Earth, Mars, and Mercury [e.g., *Malavergne et al*., 2007; *Sanloup and Fei*, 2004]. Thus, the present results on the solidus and liquidus temperatures can be applicable to the core formation processes in the terrestrial planets. Fig. 2-5 summarizes the liquidus and solidus temperatures of iron–light

element systems [*Campbell et al*., 2007; *Chudinovskikh and Boehler, R,* 2007; *Morard et al*., 2008; *Asanuma et al.*, 2010; *Terasaki et al.*, 2011; *Kamada et al.*, 2012] and peridotite [*Fiquet et al*., 2010; *Zhang and Herzberg*, 1994].

The liquidus temperature in this study is about 500 K lower than that of pure Fe [*Anzellini et al*., 2013; *Ma et al.*, 2004]. In addition, the present liquidus curve in Fe–Si–S is lower than the melting temperature in the Fe–Si alloy reported by *Asanuma et al*. [2010] and close to the liquidus of the Fe–S–O system [*Terasaki et al.*, 2011]. The present solidus of the Fe–S–Si system is very close to the eutectic temperature of the Fe–S system [*Campbell et al*., 2007; *Chudinovskikh and Boehler, R,* 2007; *Morard et al*., 2008: *Kamada et al*., 2012] and the solidus of the Fe–S–O system [*Terasaki et al*., 2011] within experimental uncertainties. This result indicates that the effect of the addition of Si and O on the depression of eutectic temperatures in the Fe–S system is very small.

2.4.2. Implications for the core of the Mars and Mercury

The Fe–S–Si system has a very low solidus temperature compared to the solidus of the silicate mantle, which indicates that heating during accretion of the Earth created a metallic melt in crystalline silicates, and the core separation perhaps started by percolation of a eutectic-like metallic melt with S-enrichment in the silicate mantle early in the accretion of the planetesimals [*Terasaki et al*., 2005]. The thermal models of Mars and Mercury [*Breuer et al*., 2007; *Solomon*, 1976; *Toksoz et al*., 1978] indicate that the internal temperatures approached the solidus temperature of the silicate mantle, and the magma ocean stage occurred early in the histories of these planets. By assuming that the cores of the planets contain both S and Si as light elements [*Malavergne et al*., 2007; *Malavergne et al*., 2010], the models of the thermal history of these planets suggest that, during their formation, the temperature in their centers

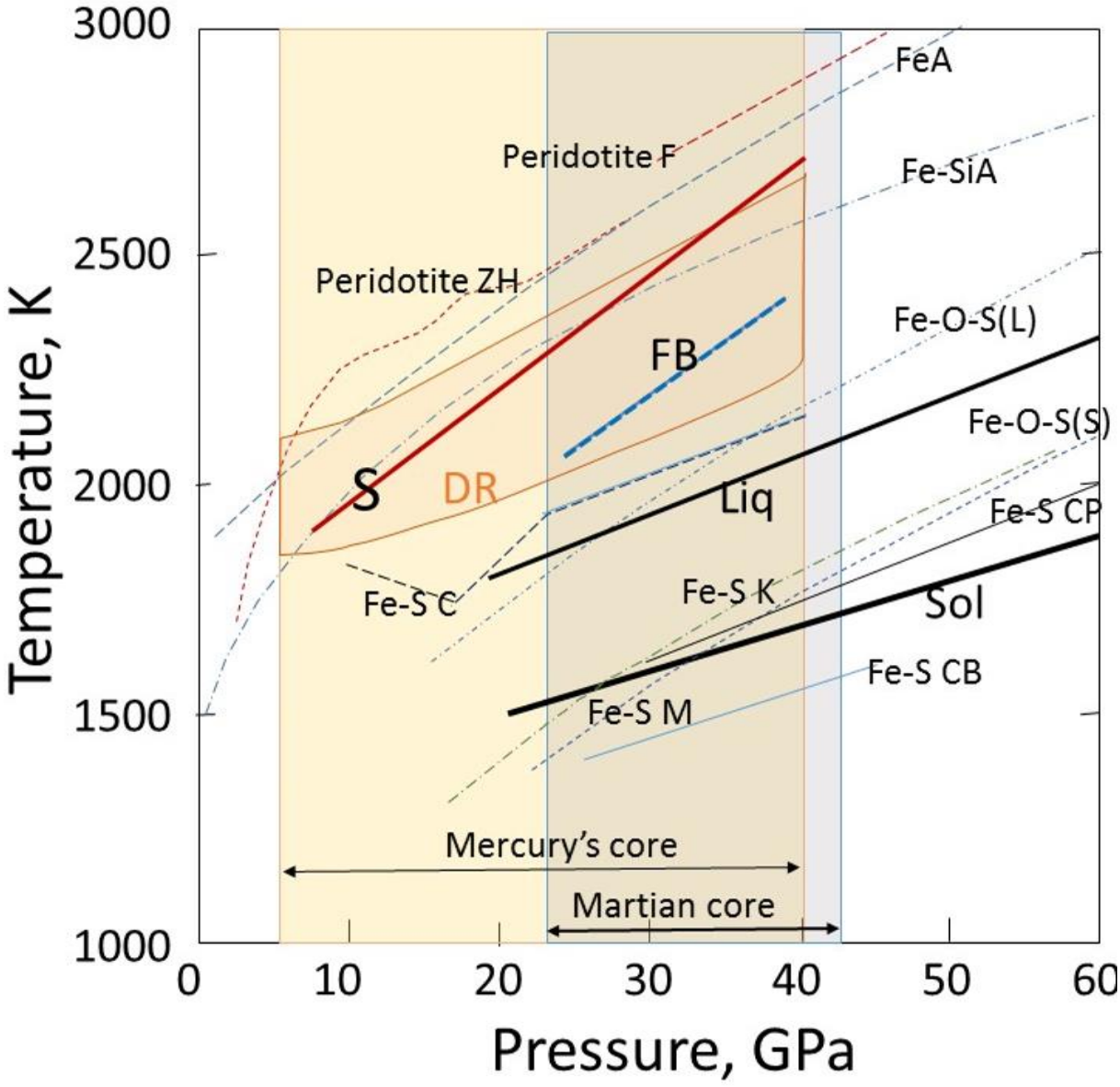

Fig. 2-5. The melting curves of Fe and Fe-light element systems. Temperature profiles of the cores of Mars and Mercury are also shown. The laveled bold solid lines are Sol and Liq, which show the solidus and liquidus temperatures of the $Fe_{80.1}S_{12.7}Si_{7.2}$ composition in the Fe–S–Si system. The adiabatic temperature of the core of Mercury estimated by this work, 27 K/GPa, is given as a red curve, S, under the assumption that the temperature at CMB of Mercury is 1800 K [e.g., *Dumberry and Rivoldini*, 2015; *Malavergne et al.*, 2010]. The temperature profiles of the Martian core estimated by *Fei and Bertka* [2005], and Mercury's core by *Dumberry and Rivoldini* [2015] are also shown as FB and DR. The previously reported melting curves of Fe-light element systems and solidus of peridotite are shown in this figure as follows. Melting curve of Fe by *Anzellini et al*. [2013] is labeled as Fe A; melting curve of Fe–Si by *Asanuma et al*. [2010] is labeled as Fe–Si A; solidus of the Fe–S system reported by *Kamada et al*. [2012] is labeled as Fe–S K; liquidus of Fe–S by *Chen et al*. [2008] is labeled as Fe–S C; solidus and liquidus temperatures for a composition of $Fe_{75}O_5S_{20}$ reported by *Terasaki et al*. [2011] are labeled as Fe-O-S(S) and Fe-O-S(L). Also, the eutectic of the Fe–S system by *Campbell et al*. [2007] is Fe–S CP; the eutectic of Fe-S by *Morard et al*. [2007] is Fe–S M; the eutectic of Fe–FeS by *Chudinovskikh and Borhler* [2007] is Fe–S CB; The solidus temperature of peridotite by *Fiquet et al*. [2010] is labeled as Peridotite F and that by *Zhang and Herzberg* [1994] is labeled as Peridotite ZH. The pressure conditions for the cores of Mercury and Mars are shown as shaded areas, yellow and gray.

approached or exceeded the liquidus temperature of the Fe–S–Si system after the magma ocean stage. Thus, the cores of these planets were once molten in the early stage of their core formation.

Existence of an ancient magnetic field in Mercury [*Johnson et al*., 2015] implies the operation of a dynamo in the molten core in Mercury's early history. Recent works on longitude libration of Mercury showed that the mantle and core of Mercury are decoupled and thus Mercury's core is at least partially molten [e.g., *Margot et al*., 2007; *Riner et al*., 2008].

Assuming that the core of Mercury is composed of iron alloy with minor amounts of sulfur and silicon and more likely to be under the reducing core conditions of the planet, we can estimate the adiabatic gradient of the molten core of the planet. The adiabatic gradient of the molten core can be expressed as follows [*Anderson*, 1998]:

$$\left(\frac{\partial \ln T}{\partial \ln \rho}\right)_S = \gamma_{th} \tag{2-2}$$

where T is a temperature at a certain depth in the outer core, ρ is the density of the core at that depth, and γ_{th} is the thermodynamic Grüneisen parameter. Therefore, the core–mantle boundary (CMB) temperature can be calculated as follows:

$$T_{CMB} = T_{ICB}\left(\frac{\rho_{CMB}}{\rho_{ICB}}\right)^{\gamma_{th}} \tag{2-3}$$

where T_{CMB} and T_{ICB} are temperatures at the CMB and the ICB conditions, respectively, and ρ_{CMB} and ρ_{ICB} are densities of the molten core at CMB and ICB, respectively. To calculate the adiabatic temperature gradients under the liquid core conditions, the thermodynamic Grüneisen parameter γ_{th} of the outer core may be around 1.3 [*Anderson*, 1998; *Dubrovinsky*, 2000; *Stacey*, 1995; *Vocadlo et al*., 2000]. However, it could have a large uncertainty. Therefore, we assumed γ_{th} to be in the range of 1.0–1.5. The density of molten metal in the core of Mercury may be taken to be the density of the Fe–S melt [*Sanloup et al*., 2000, 2002; *Terasaki*, 2016] or the Fe–

Si melt at high pressure [*Tateyama et al*., 2011; *Yu and Secco*, 2008; *Nishida et al*., 2011; *Terasaki*, 2015], and the CMB temperatures are assumed to be around 1770 K for Mercury and 1990 K for Mars [e.g., *Dumberry and Rivoldini*, 2015; *Malavergne et al*., 2010]. Based on these parameters with the above thermodynamic relations, the adiabatic temperature gradients of the liquid cores were calculated to be around 27(6) K/GPa for Mercury and 18(4) K/GPa for Mars. The adiabatic temperature gradient is consistent with that estimated by *Fei and Bertka* [2005] for the Martian core, and it is consistent but slightly greater than that estimated by *Dumberry and Rivoldini* [2015] for Mercury's core as shown in Figure 2-4.

The slope of the liquidus temperature of the Fe–S–Si system, approximately 12 K/GPa, is half of the adiabatic temperature gradient of the Mercury's and Martian cores. Although the liquidus temperature can be changed with the bulk composition of the metal systems and thus the slope of the liquidus curve could change with the composition, the above conclusion is valid for the liquidus temperatures for various bulk compositions of the Fe–S–Si system, since the slopes of the liquidus temperatures of the end member systems of Fe–S and Fe–Si are significantly smaller than the adiabatic gradient of the planets [e.g., *Chen et al*., 2008; *Asanuma et al*., 2010]. Therefore, crystallization of the core of the planets must have started at CMB. This crystallization start is consistent with the snowing-core model proposed for Ganymede [*Hauck et al*., 2006] and Mars [*Stewart et al.*, 2007].

The liquidus curve determined here for the present composition of the Fe–S–Si system relevant to Mercury's core is slightly lower than that of the Fe–S system with the same S content estimated by *Chen et al*. [2008], i.e., the existence of Si slightly lowers the liquidus of the Fe–S system. The conclusion of snowing in Mercury's core with the assumption of the Fe–S core suggested by *Chen et al*. [2008] is also valid for the Si and S bearing core model of Mercury, which is more likely under the reducing conditions in Mercury's core. The crystals

falling into the core could be dissolved again in the molten core, which would make it difficult to maintain the layered core structure composed of a completely molten outer core and a crystalline inner core in the planets. However, when the core adiabat is located between the solidus and liquidus temperatures of the core materials during cooling, we can expect core stratification in the form of a partially crystallizing outer core and precipitated crystalline inner core.

2.5. References

Alfé, D., G. D. Price, and M. J. Gillan (2002), Iron under Earth's core conditions: liquid-state thermodynamics and high-pressure melting curve from ab initio calculations. *Phys. Rev. **B*** **65**, 165118.

Allégre, C. J., J. P. Poirier, E. Humler, and A. W. Hofmann (1995), The chemical composition of the Earth. *Earth Planet. Sci. Lett.* **134**, 515–526.

Anderson, O. L. (1998), The Grüneisen parameter for iron at outer core conditions and the resulting conductive heat and power in the core. *Phys. Earth Planet. Inter*. **109**, 179–197.

Anzellini, S., A. Dewaele, M. Mezouar, P. Loubeyre, and G. Morard (2013), Melting of iron at Earth's inner core boundary based on fast X-ray diffraction. *Science* **340**, 464–466.

Asanuma, H., E. Ohtani, T. Sakai, H. Terasaki, S. Kamada, N. Hirao, N. Sata, and Y. Ohishi (2008), Phase relations of Fe-Si alloy up to core conditions: Implications for the Earth inner core. *Geophys. Res. Lett*. **35**, L12307.

Asanuma, H., E. Ohtani, T. Sakai, S. Kamada, H. Terasaki, T. Kondo, and T. Kikegawa (2010), Melting of iron-silicon alloy up to the core-mantle boundary pressure: Implications to the thermal structure of the Earth's core. *Phys. Chem. Minerals.* **37**, 353–359.

Asanuma, H., E. Ohtani, T. Sakai, H. Terasaki, S. Kamada, N. Hirano, and Y. Ohishi (2011),

Static compression of $Fe_{0.83}Ni_{0.09}Si_{0.08}$ alloy to 374GPa and $Fe_{0.93}Si_{0.07}$ alloy to 252GPa: Implications for the Earth's inner core. Earth Planet. Sci. Lett., **3**, 113-118.

Badro, J., G. Fiquet, F. Guyot, E. Gregoryanz, F. Occelli, D. Antonangeli, and M. d'Astuto (2007), Effect of light elements on the sound velocities in solid iron: Implications for the composition of Earth's core. *Earth Planet. Sci. Lett.* **254**, 233–238.

Bertka, C. M. and Y. Fei (1998), Density profile of an SNC model Martian interior and the moment-of inertia factor of Mars. *Earth Planet Sci. Lett.* **157**, 79–88.

Breuer, D., S. A. Hauck II, M. Buske, M. Pauer, and T. Spohn (2007), Interior evolution of Mercury. *Space Sci. Rev.* **132**, 229–260.

Birch, F. (1964), Density and composition of mantle and core. *J. Geophys. Res*. **69**, 4377–4388.

Boehler, R. (1996), Melting and element partitioning Fe-FeS eutectic temperatures to 620 kbar. *Phys. Earth Planet. Inter*. **96**, 181–186.

Brown, J. M. (1999), The NaCl pressure standard. *J. Appl. Phys.* **86**, 5801–5808.

Campbell, A.J, CT. Seagle, D. Heinz, G. Shen, and VB. Prakapenka (2007), Partial melting in the iron-sulfur system at high pressure: A synchrotron X-ray diffraction study. *Phys. Earth Planet. Inter.* 162:119–128.

Chen, B., L. Gao, K. Funakoshi, and J. Li (2007), Thermal expansion of iron-rich alloys and implications for the Earth's core. *Proc. Natl. Acad. Sci. U. S. A.* 104, 9162–9167.

Chen, B., J. Li, and S. A. Hauck (2008), Non-ideal liquidus curve in the Fe-S system and Mercury's snowing core. *Geophys. Res. Lett*. **35**, L07201.

Chudinovskikh, L., and R. Boehler (2007) Eutectic melting in the Fe-S system to 44 GPa. *Earth Planet. Sc. Lett*. **257:**97–103

Dubrovinsky, L. S., S. K. Saxena, N. A. Dubrovinskaia, S. Rekhi, and T. Le Bihan (2000), Grüneisen parameter of e-iron up to 300 GPa from in-situ X-ray study. *Am. Mineral.* **85**,

386–389.

Dumberry, M., and A. Rivoldini, (2015), Mercury's inner core size and core-crystallization regime. *Icarus* **248**, 254–268.

Fei, Y., C. M. Bertka, and L. W. Finger (1997), High-pressure iron-sulfur compound, Fe_3S_2, and melting relations in the Fe-FeS system. *Science* **275**, 1621–1623.

Fei, Y., and C. M. Bertka (2005), The interior of Mars. *Science* **308**, 1120–1121.

Fei, Y., J. Li, C. M. Bertka, and C. T. Prewitt (2000), Structure type and bulk modulus of Fe_3S, a new iron-sulfur compound. *Am. Mineral.* **85**, 1830–1833.

Fei, Y., A. Ricolleau, M. Prank, K. Mibe, G. Shen, and V. Prkapenka (2007), Toward an internally consistent pressure scale. *Proc. Natl Acad. Sci. U. S. A.* **104**, 9182–9186.

Fiquet, G., A. L. Auzende, J. Siebert, A. Corgne, H. Bureau, H. Ozawa, and G. Garbarino (2010), Melting of peridotite to 140 gigapascals. *Science* **329**, 1516–1518.

Fischer, R. A., A. J. Campbell, D. M. Reaman, N. A. Miller, D. L. Heinz, P. Dera, V. B. Prakapenka (2013), Phase relations in the Fe-FeSi system at high pressures and temperatures. *Earth Planet. Sci. Lett.* **373**, 54–64.

Hauck, S. A., J. M. Aurnau, and M. J. Dombard (2006), Sulfur's impact on core evolution and magnetic field generation on Ganymede. *J. Geophys. Res.* **111**, E09008.

Hillgren, V., C. K. Gessman, and J. Li (2000), An experimental perspective on the light element in Earth's core. In: Canup, R.M., Righter, K. (Eds), *Origin of the Earth and Moon.* The University of Arizona, pp. 245–263.

Hirao, N., E. Ohtani, T. Kondo, and T. Kikegawa (2004), Equation of state of iron-silicon alloys to megabar pressure. *Phys. Chem. Min.* **31**, 329–336.

Javoy, M. (1995), The integral enstatite chondrite model of the Earth. *Geophys. Res. Lett*. **22**, 2219–2222.

Johnson, C.L., R.J. Phillips, ME. Purucker, BJ. Anderson, PK. Byrne, BW. Denevi, JM. Feinberg, Hauck SA II, Head JW III, H. Korth, PB. James, E. Mazarico, GA. Neumann, LC. Philpott, MA. Siegler, NA. Tsyganenko, and SC. Solomon (2015) Low-altitude magnetic field measurements by MESSENGER reveal Mercury's ancient crustal field. *Science*, doi:10.1126/science.aaa8720.

Kamada, S., H. Terasaki, E. Ohtani, T. Sakai, T. Kikegawa, Y. Ohishi, N. Hirao, N. Sata, and T. Kondo (2010), Phase relationships of the Fe-FeS system in conditions up to the Earth's outer core. *Earth Planet. Sci. Lett*. **294**, 94–100.

Kamada, S., E. Ohtani, H. Terasaki, T. Sakai, M. Miyahara, Y. Ohishi and N. Hirao (2012), Melting relationships in the Fe-Fe_3S system up to the outer core conditions. *Earth Planet. Sci. Lett*. **359–360**, 26–33.

Kuwayama, Y., and K. Hirose (2004), Phase relations in the system Fe-FeSi at 21 GPa. *Am. Mineral.* **89**, 273–276.

Li, J., Y. Fei, H. K. Mao, K. Hirose, and S. R. Shieh, (2001), Sulfur in the Earth's inner core. *Earth Planet. Sci. Lett*. **193**, 509–514.

Lin, J. F., D. L. Heinz, A. J. Campbell, J. M. Devine, and G. Shen (2002), Iron-silicon alloy in Earth's core? *Science* **295**, 313–315.

Ma, Y., M. Somayazulu, G. Shen, H. K. Mao, J. Shub, and R. J. Hemley (2004), In situ X-ray diffraction studies of iron to Earth-core conditions. *Phys. Earth Planet. Inter.* **85**, 319–337.

Malavergne, V., M. Tarrida, R. Combes, H. Bureau, J. Jones, and C. Schwandt (2007), New high-pressure and high-temperature metal/silicate partitioning of U and Pb: Implications for the cores of the Earth and Mars. *Geochim. Cosmochim. Acta* **71**, 2635–2655.

Malavergne, V., M. J. Toplis, S. Berthet, and J. Jones (2010), Highly reducing conditions during core formation on Mercury: Implications for internal structure and the origin of a magnetic

field. *Icarus* **206**, 199–209.

Margot, J-L., SJ. Peale, RF. Jurgens, MA. Slade, and IV. Holin (2007), Large longitude libration of Mercury reveals a molten core. *Science* **316**:710–714.

McDonough, W. F. (2003), Compositional model for the Earth's core. In: Carlson, R.W. (Ed.), *Treatise on Geochemistry*, Volume 2, Elsevier B.V, Amsterdam, pp. 547–568.

McDonough, W. F. (2014), Compositional model for the Earth's core. In: Carlson, R.W. (Ed.), *The Mantle and Core*, Elsevier, Amsterdam, pp.559–577.

Morard, G., D. Andrault, N. Guignot, C. Sanloup, M. Mezouar, S. Petitgirard, and G. Fiquet (2008), In-situ determination of Fe-Fe_3S phase diagram and liquid structural properties up to 65 GPa. *Earth Planet. Sci. Lett.* **272**, 620–626.

Morard, G., C. Sanloup, B. Guillot, G. Fiquet, M. Mezouar, J. P. Perrillat, G. Garbarino, K. Mibe, T. Komabayashi, and K. Funakoshi, (2008), In situ structural investigation of Fe-S-Si system and evolution of Fe-S bond properties with pressure. *J. Geophys. Res.* **113**, B10205.

Morard, G., and T. Katsura (2010), Pressure-temperature cartography of Fe-S-Si immiscible system. *Geochim. Cosmochim. Acta* **74**, 3659–3667.

Morard, G., D. Andrault, N. Guignot, J. Sieveert, G. Garbarino, and D. Antonangeli (2011), Melting of Fe-Ni-Si and Fe-Ni-S alloys at megabar pressures: implications for the core – mantle boundary temperature. *Phys. Chem. Miner*. **38**, 767–776.

Nishida, K., E. Ohtani, S. Urakawa, A. Suzuki, T. Sakamaki, H. Terasaki, and Y. Katayama (2011), Density measurement of liquid FeS at high pressures using synchrotron X-ray absorption, *Am. Mineral.*, **96**, 864–868.

Ohishi, Y., N. Hirao, N. Sata, K. Hirose, and M. Takata (2008), Highly intense monochromatic X-ray diffraction facility for high-pressure research at Spring-8. *High Pressure Res.* **28**,

163–173.

Ozawa, H., K. Hirose, T. Suzuki, Y. Ohishi, and N. Hirao (2013), Decomposition of Fe_3S above 250 GPa. *Geophys. Res. Lett*., **40**, 4845–4849.

Poirier, J. P. (1994), Light elements in the Earth's outer core: a critical review. *Phys. Earth Planet. Inter.* **6**, 123–130.

Riner, MA., CR. Bina, MS. Robinson, and SJ. Desch (2008), Internal structure of Mercury: Implications of a molten core. *Jour. Geophys. Res*., 113, E08013. doi: 10.1029/2007JE002993.

Sakai, T., T. Kondo, E. Ohtani, H. Terasaki, N. Endo, T. Kuba, T. Suzuki and T. Kikegawa (2006), Interaction between iron and post-perovskite at core-mantle boundary and core signature in plume source region, *Geophys. Res. Lett.* **33**, L15317.

Sanloup, C., F. Guyot, P. Gillet, G. Fiquet, M. Mezouar, I. Martinez (2000), Density measurements of liquid Fe-S alloys at high-pressure. *Geophysical Res. Lett.* **27**, 811–814.

Sanloup, C., F. Guyot, P. Gillet, and Y. Fei (2002), Physical properties of liquid Fe alloys at high pressure and their bearings on the nature of metallic planetary cores. *J. Geophys. Res.* **107**, 2272, doi:10.1029/2001JB000808

Sanloup, C., and Y. Fei (2004), Closure of the Fe-S-Si liquid miscibility gap at high pressure. *Phys. Earth Planet. Inter.* **147**, 57.

Seagle, C. T., A. J. Campbell, D. L. Heinz, G. Shen, and V. B. Prakapenka (2006), Thermal equation of state of Fe_3S and implications for sulfur in Earth's core. *J. Geophys. Res*. **111**, B06209.

Seto, Y., D. Nishio-Hamane, T. Nagai, and N. Sata (2010), Development of a software suite on X-ray diffraction experiments. *Rev. High Pressure Sci. Technol.* **20**, 269–276.

Shen, G., H. K. Mao, and R. J. Hemley (1996), Laser-heated diamond anvil cell technique:

Double-sided heating with multimode Nd:YAG laser. Advanced Materials '96–New Trends in High Pressure Research. *Nat. Inst. Res. Inorg. Mater*, Tsukuba, pp 149–152.

Simon, F. E., and G. C. Glatzel (1929), Remarks on fusion pressure curve. *Z. Anorg. Allg. Chem*. **178**, 309.

Solomon, S. C. (1976), Some aspects of core formation in Mercury. *Icarus* **28**, 509–521.

Stacey, F. D. (1995), Theory of thermal and elastic properties of the lower mantle and core. *Phys. Earth Planet. Inter*. **89**, 219–245.

Stewart, A. J., M. W. Schmidt, W. V. Westrenen, and C. Liebske (2007), Mars. A New core-crystallization regime. *Science* **316**, 1323–1325.

Tateno, S., Y. Kuwayama, K. Hirose, and Y. Ohishi (2015), The structure of Fe–Si alloy in Earth's inner core. *Earth and Planetary Science Letters* **418**:11–19

Tateyama, R., E. Ohtani, H. Terasaki, K. Nishida, Y. Shibazaki, A. Suzuki, and T. Kikegawa (2011), Density measurements of liquid Fe-Si alloys at high pressure using sink-float method. *Phys. Chem. Minerals*, **38**, 801–807.

Terasaki, H., D. J. Frost, D. C. Rubie, and F. Langenhorst (2005), The effect of oxygen and sulphur on the dihedral angle between Fe-O-S melt and silicate minerals at high pressure: implications for Martian core formation. *Earth Planet. Sci. Lett.* **232**, 379–392.

Terasaki, H., S. Kamada, T. Sakai, E. Ohtani, N. Hirao, and Y. Ohishi (2011), Liquidus and solidus temperatures of a Fe-O-S alloy up to the pressures of the outer core: Implication for the thermal structure of the Earth's core. *Earth Planet. Sci. Lett.* **304**, 559–564.

Terasaki, H. (2015), Physical Properties of the Outer Core. In: Terasaki, H and Fischer, Ch.11, Deep Earth: Physics and Chemistry of the lower mantle and core. Geophysical Monograph series, Volume 217, American Geophys. Union, pp. 129-142.

Toksoz, M. N, A. T. Hsui, and D. H. Johnston (1978), Thermal evolutions of the terrestrial

planets. *Earth Moon Planets* **18**, 281–320.

Tsuno, K., and E. Ohtani (2009), Eutectic temperatures and melting relations in the Fe-O-S system at high pressures and temperatures. *Phys. Chem. Miner*. **36**, 9–17.

Vočadlo, L., J. P. Poirer, and G. D. Price (2000), Grüneisen parameters and isothermal equations of state. *Am. Mineral.* **85**, 390–395.

Yu, X., and RA. Secco (2008), Equation of state of liquid Fe-17wt %Si to 12 GPa, *High Press. Res.* **28**, 19–28.

Zhang, J., and C. Herzberg (1994), Melting experiments on anhydrous peridotite KLB-1 from 5.0 to 22.5 GPa. *J. Geophys. Res*. **99**, 17729–17742.

Chapter 3:

Element partitioning between metallic solid and liquid in the Fe–S–Si system up to 148 GPa

3.1. Introduction

It is widely accepted that the Earth's core is mainly composed of iron, with light elements to account for its density deficit [e.g., *Birch*, 1964; *Dubrovinsky et al*., 2000]. Alloying with light elements significantly affects the physical properties of iron and interpretation of the chemical structure of the Earth's core [e.g., *Boehler*, 1996; *Li and Fei*, 2003]. Therefore, the melting relationships of the Fe–light elements system are central to clarification of the chemical structure of the core because the inner core is forming by crystallization of the molten outer core. Although there are many candidates, sulfur and silicon are considered to be two of the major light elements in the core based on geochemical modeling [e.g., *Poirier*, 1994; *Ringwood*, 1959; *Allègre et al*., 1995] and high-pressure partitioning experiments [*Hillgren et al*., 2000; *Takafuji et al*., 2005; *Sakai et al*., 2006]. Despite the importance of sulfur and silicon as the light elements of the core, previous studies, including high-pressure melting experiments in the Fe–S–Si system, have not included the pressure conditions of the core [*Sanloup and Fei*, 2004; *Morard and Katsura*, 2010]. For better understanding the chemical structure of the core, knowledge of the melting relationships, and solid–liquid partitioning in the Fe–S–Si system under the high-pressure conditions of the Earth's core is essential. Here, I report the results of experiments on element partitioning between metallic solid and liquid in the Fe–S–Si system up to 148 GPa using LHDAC. The present result provides important constraint on total amount of light elements in the Earth's bulk core and the compositions of the inner and outer core of the Earth.

3.2. Experimental procedure

3.2.1. Sample preparation

Melting experiments were performed in the pressure range of 36–148 GPa and the temperature range of 1520–4100 K using a double-sided laser-heated diamond anvil cell. The culet sizes of the diamond anvils were 100 and 300 μm, depending on the experimental pressure. In the experiments on the Fe–S–Si system, the starting materials were Fe (99.9% purity, Wako Pure Chemical Industries, Ltd), FeS (99.9% purity, Rare Metallic Co., Ltd), and FeSi (99.9% purity, Rare Metallic Co., Ltd) powders that were ground in an agate mortar for 1 hour to make a homogeneous mixture. The sample composition used for this study was Fe with 8 wt. % S and 4 wt. % Si, which approximates the density deficit in the Earth's core. I used diamond anvils and the cold compression technique to make a thin foil from the starting material. The sample foil was embedded in Al_2O_3 powder, which worked as the pressure medium and thermal insulator. These samples were then loaded into a sample hole in a preindented rhenium or tungsten gasket with typical thickness of 35–50 μm. Before loading a sample, I checked the homogeneity of the starting material using a high-resolution reflection microscope.

Each sample was initially compressed to a target pressure at room temperature, and then annealed for about 15 minutes in order to synthesize solid phases and to reduce stress in the cell assemblages at pressures above 70 GPa. The samples were heated using the double-sided laser heating method employing a high-power Nd: YAG laser or fiber laser [*Shen et al.*, 1996]. The sample was heated to the desired temperature for 10–20 min. Temperature was measured by fitting the emission spectra from the heated sample to the gray body formula, and the experimental temperatures in Table 3-1 were determined by averaging the temperatures measured over several tens of seconds. The temperature fluctuation during the experiments was approximately 50–200 K. The experimental pressure was determined from the pressure

dependence at the edge of the T_{2g} Raman band of the culet of the diamond anvil at room temperature [*Akahama and Kawamura*, 2004] and then crosschecked with the ruby fluorescence [*Deweale et al., 2004*]. The average of the pressure before and after heating was adopted as the pressure value of each experiment. Although the thermal pressure was not determined, this was estimated to be 10% higher than the pressure determined at room temperature (Table 3-1) in accordance with the findings of the previous in situ X-ray diffraction experiments [*Kamada et al*., 2010; *Kamada et al*., 2012]. The errors in temperature were estimated using the standard deviations of the temporal fluctuations in the measured temperature.

3.2.2. Chemical analyses of the recovered samples

The recovered samples were prepared for chemical analyses using a focused ion beam (JEOL JEM-9320FIB). Heated portion in the recovered sample was cut out as a block piece once (see Fig. 3-1 (a)), and put it on a copper grid using a micro manipulator attached to a dedicated optical microscope. The cupper grid surface and sample layer are parallel each other. Then, upper Al_2O_3 layer as pressure medium was removed using a coarse gallium ion beam parallel to the sample layer. Finally, the sample surface was cleaned using a fine gallium ion beam. A gallium ion beam was accelerated to 30 kV during the sputtering of the recovered samples. I used a field emission gun scanning electron microscope (FEG-SEM) (*JEOL JSM-71010 and JSM-7001F*) in addition to a conventional SEM (*JEOL JSM-5410*) for textural observation and chemical analysis. An accelerating voltage of 15 kV and a beam current of 1.4 nA were employed. I used an energy dispersive X-ray spectroscopy (EDS) system (Oxford INCA) attached to the FEG- SEM to determine the chemical compositions. This instrument was suitable to analyze the fine-grained samples. Pyrite (FeS_2) and wollastonite ($Ca_3Si_3O_9$)

Table 3-1 Experimental conditions, chemical compositions of liquid and solid Fe alloys, and solid–liquid partition coefficients of sulfur, silicon, and oxygen.

Run no	Pressure[a] (GPa)	Pressure[b] (GPa)	Temperature (K)	Phases	Composition of Fe solids and liquids (wt.%)								
					Fe	S	Si	O	Ni	Total	*Dsulfur*[d]	*Dsilicon*[e]	*Doxygen*[f]
Fe–S–Si system													
FESSI22	36.7(6)	40.4(7)	1800(50)	solid Fe (*n* = 4)[c]	96.0(5)	0.4(4)	3.6(3)	-	-	100.0	0.03(3)	4.24(178)	-
				liquid (*n* = 4)	85.3(4)	13.8(1)	0.8(3)	-	-	100.0			
FESSI06	52.4(37)	57.6(41)	2050(50)	solid Fe (*n* = 6)	92.5(3)	0.8(1)	6.7(3)	-	-	100.0	0.06(1)	5.40(55)	-
				liquid (*n* = 7)	84.4(13)	14.4(13)	1.2(1)	-	-	100.0			
FESSI25	135(5)	148(6)	4100(200)	solid Fe (*n* = 9)	95.1(15)	1.1(2)	3.7(15)	-	-	100.0	0.13(3)	2.55(114)	-
				liquid (*n* = 6)	89.8(13)	8.7(13)	1.5(3)	-	-	100.0			
Fe–S–Si–O–Ni system													
FN006	21.9(33)	24.1(36)	1520(50)	solid Fe (*n* = 10)*	69.7(3)	26.0(9)	0.6(3)	0.8(3)	4.0(4)	101.1	1.35(6)	0.31(17)	0.28(14)
				liquid (*n* = 8)	70.2(13)	19.3(5)	2.0(7)	2.8(10)	8.1(4)	102.3			
FN002	28.0(10)	30.8(11)	2000(140)	solid Fe (*n* = 2)**	93.0(12)	0.4(3)	1.0(1)	1.1(2)	5.9(4)	101.2	0.03(3)	0.59(5)	0.37(8)
				liquid (*n* = 1)	75.3(-)	11.3(-)	1.6(-)	2.8(-)	7.1(-)	98.1			
FN005	63.6(16)	70.0(18)	1700(60)	solid Fe (*n* = 8)	90.8(19)	0.1(1)	4.1(2)	0.8(1)	6.0(4)	101.8	0.01(1)	2.19(105)	0.87(18)
				liquid (*n* = 3)	79.1(26)	12.8(32)	1.9(9)	1.0(2)	4.7(6)	99.4			
FN005	63.6(16)	70.0(18)	2200(60)	solid Fe (*n* = 4)	89.2(9)	0.4(3)	3.6(2)	1.0(2)	6.2(3)	100.3	0.03(3)	1.49(24)	0.84(31)
				liquid (*n* = 3)	79.0(8)	12.5(4)	2.5(4)	1.2(3)	5.1(1)	100.2			

Table 3-1 *Continued*

Fe–S–Si–O system													
FeSSiO_001	42.6(23)	46.9(25)	1710(270)	solid Fe (*n* = *8*)	96.9(7)	1.8(6)	1.0(3)	1.2(4)	-	100.9	0.14(5)	1.37(72)	0.60(23)
				liquid (*n* = *7*)	84.9(19)	13.0(17)	0.8(3)	2.0(3)	-	100.7			

[a]Pressure at room temperature.

[b]Pressure with 10% thermal pressure adjustment.

[c]Number of electron microprobe analyses.

[d] $Dsulfur = C^{solid}_{sulfur}/C^{liquid}_{sulfur}$.

[e] $Dsilicon = C^{solid}_{silicon}/C^{liquid}_{silicon}$.

[f] $Doxygen = C^{solid}_{oxygen}/C^{liquid}_{oxygen}$.

*Solid phase is Fe_3S.

**Solid phase is fcc-Fe.

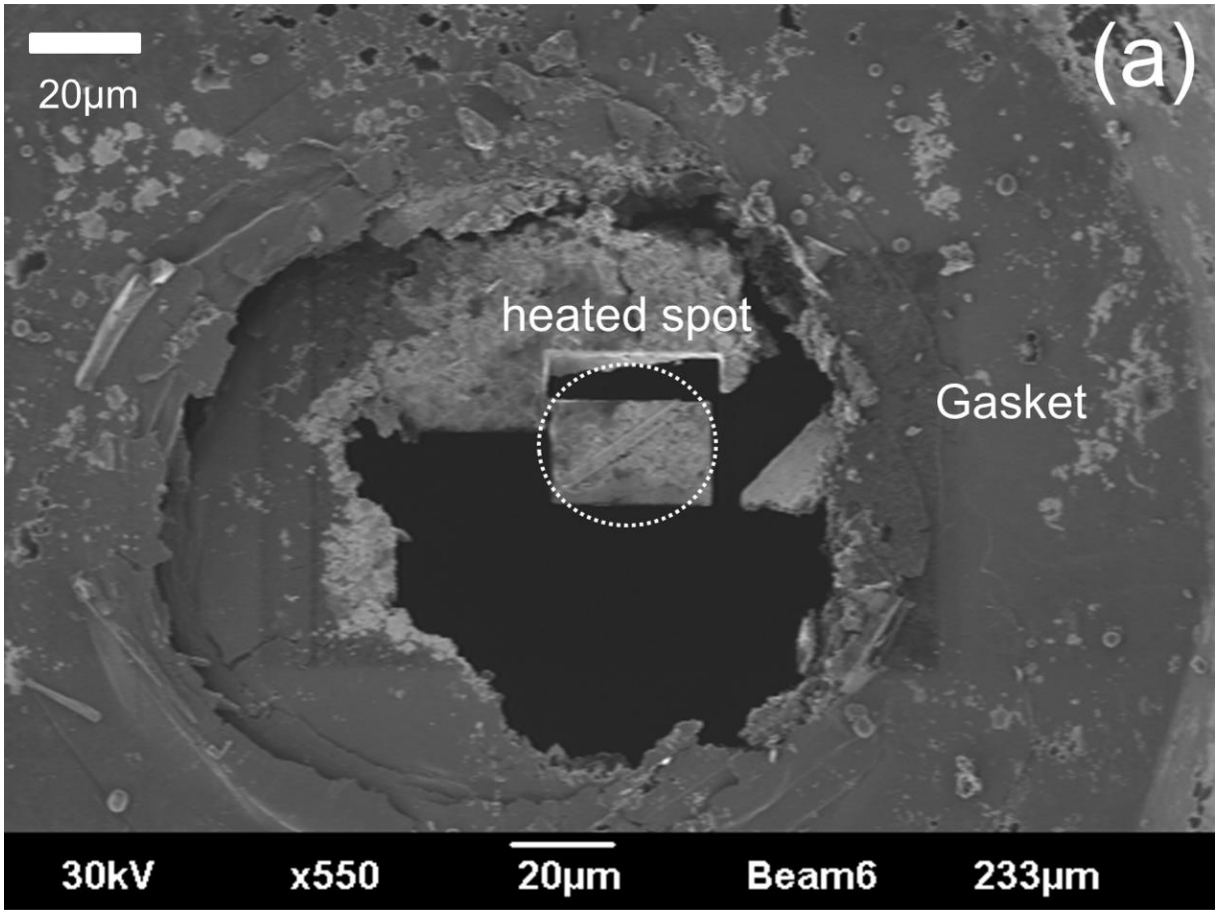

Fig. 3-1. (a) A scanning ion microscope image of the whole recovered sample from 148 GPa and 4100 K. The sample was prepared as a piece for textural observation by using an FIB. Al_2O_3 was used as a pressure medium.

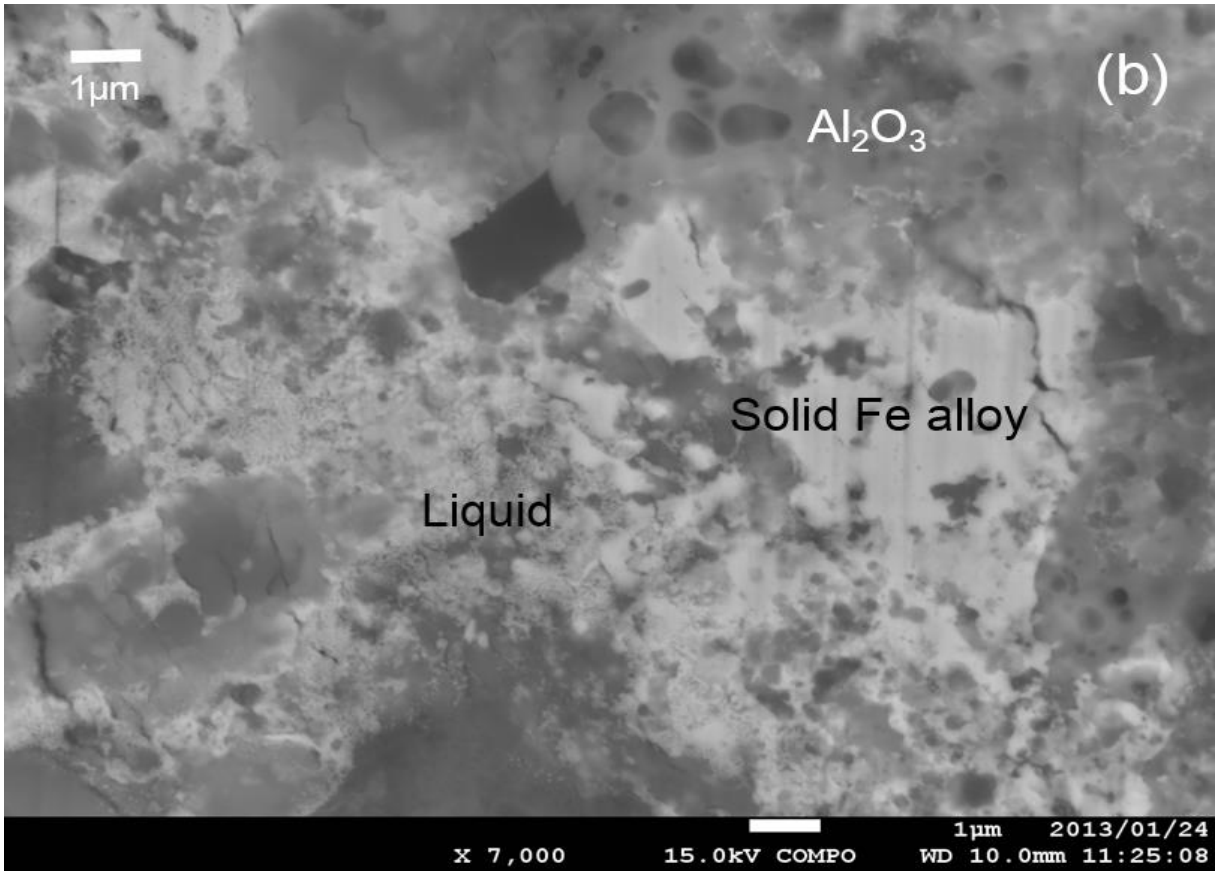

Fig. 3-1. (b) Backscattered electron image of the same sample via FEG-SEM, and a close-up image of the recovered sample coexisting with quenched liquids and solid Fe alloys.

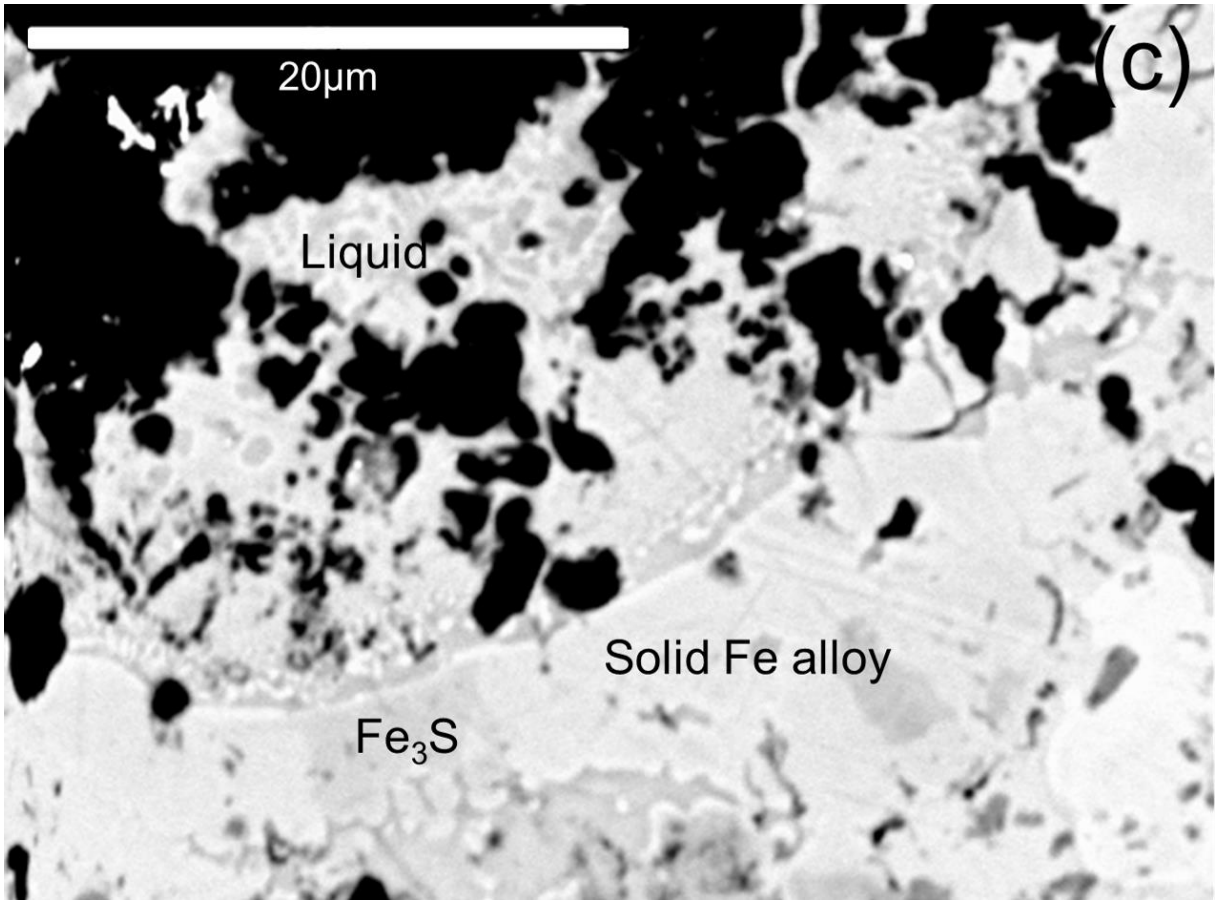

Fig. 3-1. (c) Backscattered electron image of the sample recovered from 57.6 GPa and 2050 K via SEM. A quenched liquid, solid Fe alloy, and Fe_3S were observed. The Fe_3S contains only a small amount of Si, approximately 0.2 wt. %.

were used as calibration standards for analyses of Fe, S, and Si respectively.

3.3. Results

3.3.1. Chemical analysis of recovered samples

The experimental conditions and results of chemical analyses of recovered samples are summarized in Table 3-1. Representative backscattered electron images for determining melting relationships are shown in Fig. 3-1. The compositions of the coexisting phases were determined and the partitioning behavior of sulfur and silicon between the metallic liquid and the coexisting Fe alloy was investigated.

I consistently found that a quenched liquid with a dendritic texture coexists with a solid Fe alloy in the recovered samples, implying that the samples were partially melted under the experimental pressure and temperature conditions. In the sample (run FESSI22) recovered from 40.4 GPa and 1800 K, the solid Fe alloy contained 0.4(4) wt. % S and 3.6(3) wt. % Si. On the other hand, the quenched liquid contained 13.8(1) wt. % S and 0.8(3) wt. % Si. At the maximum pressure and temperature investigated, i.e., 148 GPa and 4100 K (run FESSI25), which corresponds to the outer core conditions, the sulfur and silicon contents were 1.1(2) and 3.7(15) wt. % in solid Fe and 8.7(13) and 1.5(3) wt.% in the quenched liquid, respectively. Thus, differences in partitioning behavior of sulfur and silicon between a quenched liquid and solid Fe alloy were clearly observed, under each pressure condition in the Fe–S–Si system (see Table 3-1).

In the sample recovered from 58 GPa and 2050 K (run FESSI06), Fe_3S, which has been reported as an intermediate phase in the Fe–S system [*Fei et al*., 1997; *Fei et al*., 2000; *Li et al*., 2001] was observed along with the solid Fe alloy (Fig. 3-1 (c)). This implies that the solid Fe alloys containing silicon and Fe_3S are the subsolidus phases in the Fe–S–Si system under

this pressure condition. The silicon content in Fe_3S was significantly smaller (0.2(1) wt. %) than that of solid Fe alloy. Fe_3S appeared as a result of a reaction between Fe and FeS, while other possible phases in the Fe–FeS system, such as Fe_2S and Fe_3S_2, were not observed in this study. The phases observed in the present Fe–S–Si system were consistent with the findings of previous studies in the Fe–FeS system. [*Li et al*., 2001; *Kamada et al.*, 2010: *Kamada et al*., 2012]. On the other hand, silicon was incorporated into solid Fe as a solid solution, as confirmed by chemical analyses and in situ X-ray diffraction (XRD) in this study (see Chapter 2).

3.3.2. Partitioning coefficients of sulfur, silicon, and oxygen

In order to discuss the composition of the Earth's inner and outer cores in more details, the results of partitioning experiments in the Fe–S–Si–O and Fe–S–Si–O–Ni systems were referred in this study [*Watanabe*, 2015 (Graduation thesis); *Watanabe*, 2015 (Master thesis)]. The partition coefficient (*D*) between solid and liquid Fe alloy for an element X is calculated as:

$$D_X^{s/l} = \frac{C_X^{solid}}{C_X^{liquid}}, \quad (3\text{-}1)$$

where C_X is the average atomic concentration by weight (wt.%) of element X either in the solid phase or the liquid phase. The partition coefficients of sulfur, silicon, and oxygen (D_{sulfur}, $D_{silicon}$, D_{oxygen}) from the present chemical analyses are shown in Table 3-1.

Fig. 3-2 (a) shows variation in D_{sulfur}, $D_{silicon}$, and D_{oxygen}, between solid Fe and liquid metal, as a function of pressure. In the Fe–S–Si system, the value obtained for D_{sulfur} at 40.4 GPa was 0.03(3), whereas $D_{silicon}$ was 4.24(177), which is significantly higher. The obtained value of D_{sulfur} at the outer core condition, 148 GPa and 4100 K, was 0.13(3) and that of $D_{silicon}$ was 2.55(114). These results indicate that a silicon-rich solid Fe alloy coexists with sulfur-rich metallic liquid. In the Fe–S–Si–O and Fe–S–Si–O–Ni systems, the partitioning coefficients

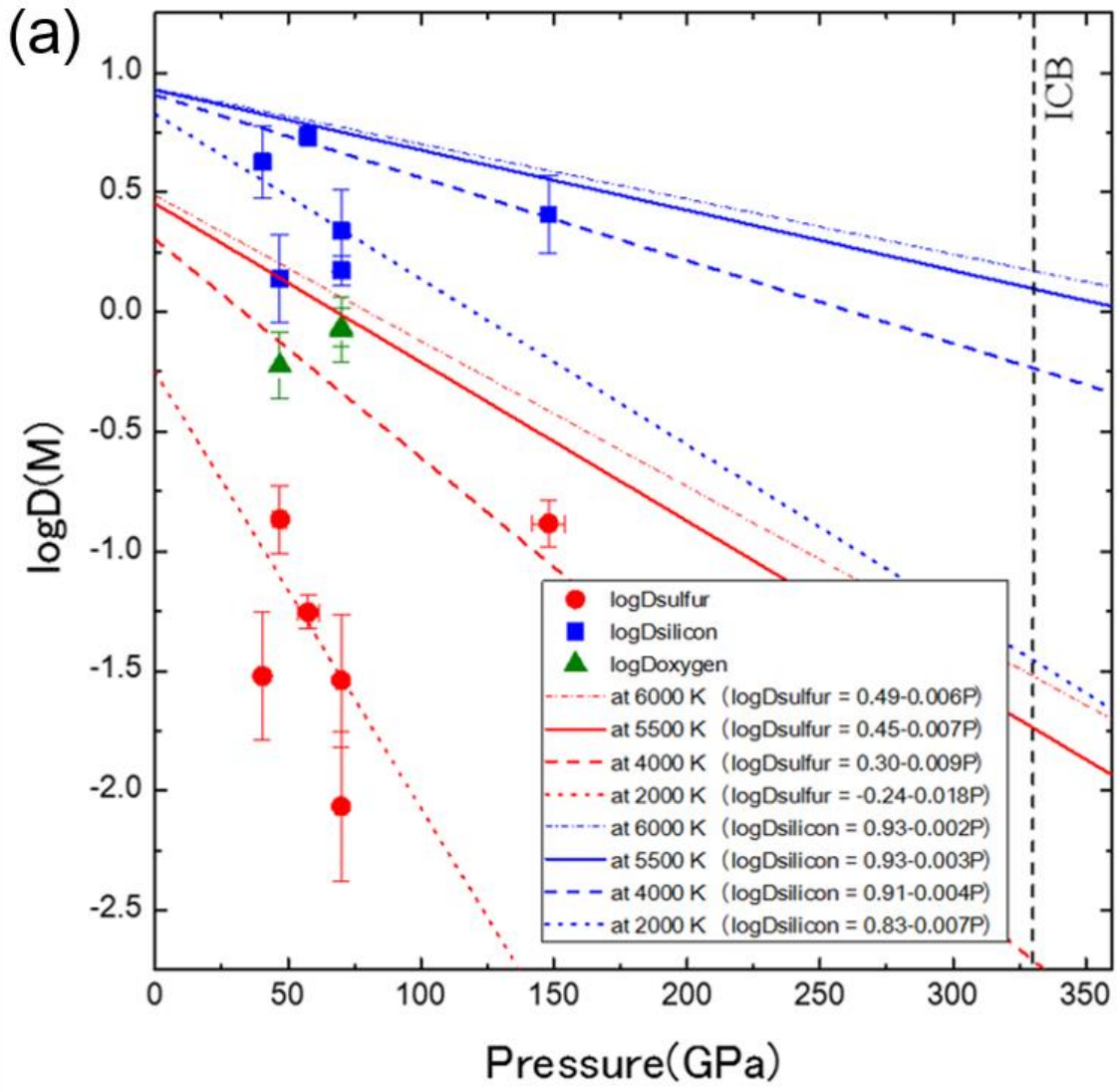

Fig. 3-2. (a) Partitioning coefficients of sulfur, silicon, and oxygen as a function of pressure and temperature, showing the dependency of logD_{sulfur} and log$D_{silicon}$ at 2000, 4000, 5500, and 6000 K. The red circles, blue squares, and green triangles show the partitioning coefficients of sulfur, silicon, and oxygen, respectively, between the liquid and solid Fe alloy. The red dashed, dotted, and solid lines show the pressure dependency of logD_{sulfur} at various temperatures using formulas derived from least squares fitting. The blue dashed, dotted, and solid lines show the pressure dependency of log$D_{silicon}$.

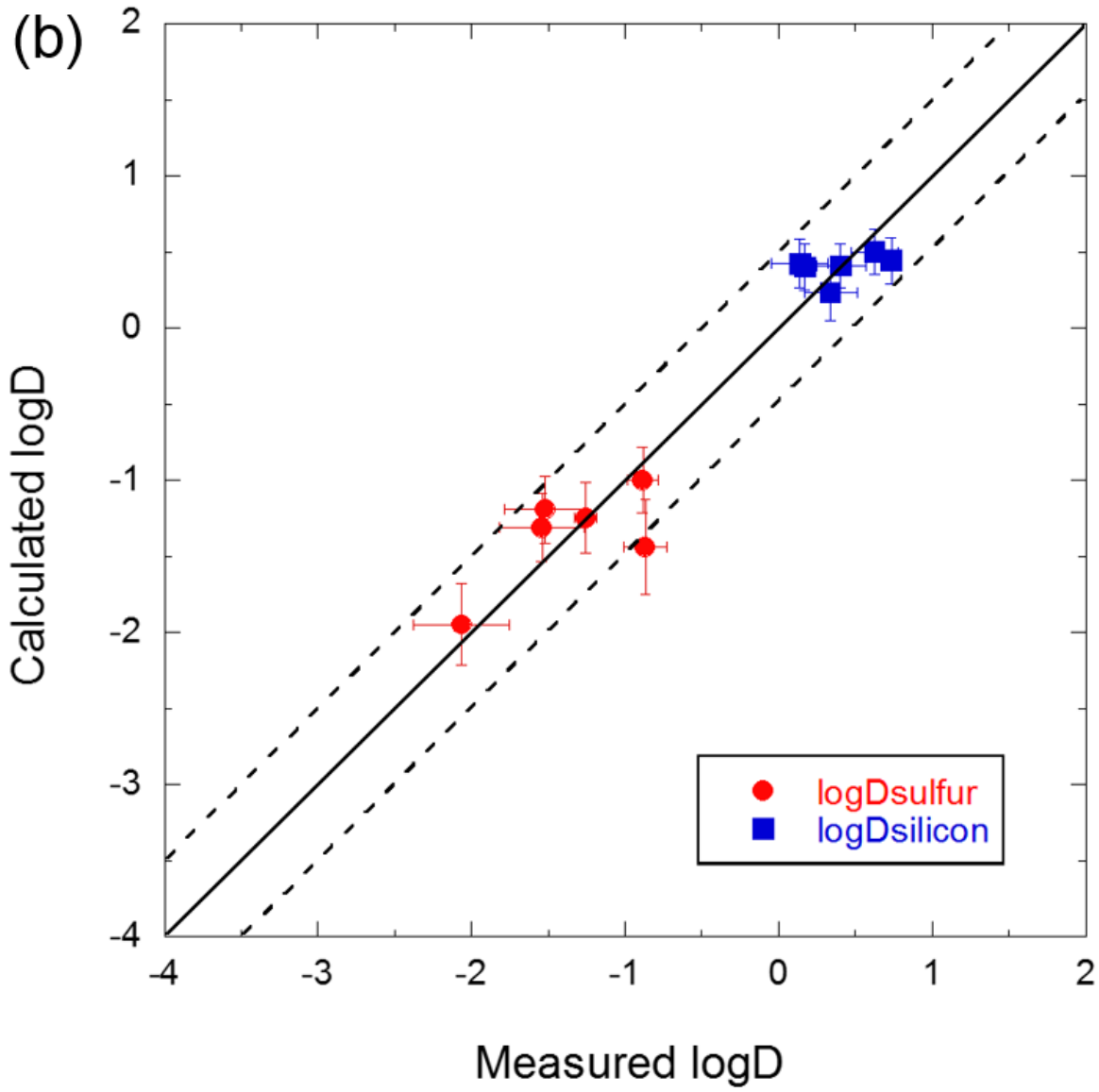

Fig. 2-2. (b) Comparison of measured and calculated partitioning coefficients of sulfur and silicon. Calculated logD_{sulfur} and log$D_{silicon}$ are the estimation using thermodynamic relationship of Eq. (3-2) (see main text for details). The 2sigma for fitting by the Eq. (3-2) is shown as dashed lines.

between solid Fe and liquid metal reveal several trends. Sulfur is strongly incorporated into liquid metal, relative to the solid Fe alloy, except at the lowest pressure (24.1 GPa). The solid phase in this run is Fe_3S, based on its composition. Silicon is enriched in solid Fe at higher pressures, while at relatively lower pressures below 40 GPa, the silicon is more partitioned in the liquid phase. This is caused by differences in the solid phases, Fe_3S at 24.1 GPa and fcc-Fe at 30.8 GPa. Oxygen is partitioned primarily into liquid in each pressure condition.

Previous studies have revealed that the solubility of sulfur in pure solid Fe has a maximum value at the eutectic temperature and increases with increasing pressure, with about 7 at. % of sulfur at around 123 GPa in the Fe–S system [*Kamada et al*., 2012], which is significantly larger than the 2 at. % (1.1 wt. %) sulfur content found in Fe–Si alloy here.

Based on previous in situ XRD experiments, in the pressure conditions of this study, the crystal structure of the solid Fe would be fcc phase or hcp phase. Through high-pressure experiments on Fe–Si alloys, *Lin et al*. [2002] reported that the hcp phase contains slightly more silicon than the fcc phase. Indeed, we observed a dramatic change in $D_{silicon}$, i.e., $D_{silicon} < 1.0$ at pressures below 31 GPa and $D_{silicon} > 1.0$ above this pressure (see Table 3-1). Considering these results, the crystal structure of the solid Fe alloy in run FN002 at low pressure would be fcc phase. Previous studies have reported that pure Fe at inner core boundary (ICB) conditions has the hcp structure [e.g., *Tateno et al*., 2010]. Therefore, while experimental results at pressures above 40 GPa may be applicable to the Earth's core, results at lower pressures cannot be used for this discussion.

3.3.3. Pressure and temperature dependences of D_{sulfur}, $D_{silicon}$, and D_{oxygen}

When considering the pressure and temperature dependencies of partitioning coefficient of sulfur and silicon in metal, we can use the thermodynamic relationship introduced

by some previous works [e.g., *Gudfinnsson and Presnall*, 2001]. These are expressed as follows:

$$\log D_M = A + B/T + C \times P/T. \quad (3\text{-}2)$$

where T and P represent temperature in Kelvin and pressure in GPa, respectively, and A, B, and C are fitting parameters.

The parameters A, B, and C in Eq. (3-2) were determined by fitting the sulfur and silicon partitioning coefficient data by the least squares method. The expression for D_{sulfur} was determined as:

$$\log D_{sulfur} = 0.85\ (\pm\ 0.13) - 2208\ (\pm\ 262)/T - 36.5\ (\pm\ 4.1) \times P/T. \quad (3\text{-}3)$$

The expression for $D_{silicon}$ was:

$$\log D_{silicon} = 0.98\ (\pm\ 0.09) - 311\ (\pm\ 181)/T - 13.8\ (\pm\ 2.9) \times P/T. \quad (3\text{-}4)$$

The pressure and temperature dependences of D_{sulfur} and $D_{silicon}$ are shown in Fig. 3-2 (a). Fig. 3-2 (b) shows the comparison of measured and calculated log*D* of sulfur and silicon, respectively. Measured log*D* is the data obtained in the experiments and calculated log*D* is the estimation using Eq. (3-2). When considering small difference between the value of measured and calculated log*D*, we can see the value derived from equation are appropriate for estimating log*D* under different pressure and temperature conditions in this study. We can see that both D_{sulfur} and $D_{silicon}$ decrease with increasing pressure, indicating that pressure has a negative effect on D_{sulfur} and $D_{silicon}$. On the other hand, D_{sulfur} and $D_{silicon}$ increase with increasing temperature, indicating that temperature has a positive effect on D_{sulfur} and $D_{silicon}$. In order to discuss the chemical structure of the Earth's core, the expressions of $\log D_{sulfur}$ and $\log D_{silicon}$ were extrapolated to the ICB condition assuming a pressure of 330 GPa and a temperature of 5500 ± 500 K, with the latter based on melting experiments on Fe–light element systems [e.g., *Terasaki et al*., 2011]. D_{sulfur} and $D_{silicon}$ were estimated to be 0.02(2) and 1.25(72), respectively,

at ICB conditions. These results imply that sulfur is likely to be partitioned into the liquid outer core, whereas silicon is likely to be partitioned into the solid inner core. Although initial inner core crystallization might have occurred at the higher temperature (6000K), the partitioning behavior would have been nearly the same (Fig. 3-2 (a)). In case of the partition coefficient of oxygen, there are few data points in this study. Although it is difficult to apply Eq. (3-2) on D_{oxygen}, we can see that oxygen is slightly enriched in the liquid phase. Considering that D_{oxygen} did not change significantly with increasing pressure and temperature, as shown in Table 3-1, I tentatively assumed that D_{oxygen} at ICB condition is 0.76(56) which is the average of the D_{oxygen} in the Fe–S–Si–O and Fe–S–Si–O–Ni systems. The estimated value of D_{sulfur} and D_{oxygen} at ICB condition in this study are quite different from the ab initio calculated behavior by *Alfè et al*. [2002]. Because of the large uncertainty in D_{oxygen}, we need further study on the partitioning of oxygen between solid and liquid iron.

3.4. Discussion

3.4.1. Calculation of the amount of light elements in the bulk core

Information on partitioning of light elements between the metallic liquid and hcp-Fe alloy is the key to clarify the chemical structure of the Earth's core because the inner core is considered to have crystallized from the liquid outer core during cooling and inner core growth is an ongoing process. Moreover, previous studies have strongly implied that sulfur, silicon, and oxygen are the plausible candidates for the light elements in the core [e.g., *Hillgren et al.*, 2000]. Therefore, my experimental results provide important clues for understanding the composition of the Earth's core. In order to demonstrate the influence of this study, the bulk composition of the Earth's core was calculated based on the present results of partitioning experiments. Assuming iron and iron alloys are ideal mixing compounds, we calculated the bulk composition

of the core by finding possible combination of light elements (silicon, sulfur, and oxygen) for which their densities match the seismologically determined density of the core [*Dziewonski and Anderson*, 1981]. The densities of solid iron and iron alloys at ICB condition (assuming a pressure of 330 GPa and a temperature of 5500 K [*Terasaki et al*., 2011]) were calculated by using the data of thermal equation of state of iron alloys [*Sakai et al*., 2014; *Fischer et al*., 2011;2014; *Seagle et al*., 2006]. The densities of molten iron and FeS at ICB condition were derived from the estimation based on *ab initio* calculations of liquid iron and Fe–S alloys [*Vočadro et al.*, 2003; *Umemoto et al*., 2014] In the case of Fe–Si, Fe–O compounds, the density decrease due to melting was assumed to be 1.8 % [e.g., *Vočadro et al.*, 2003]. The possible combination of light elements, silicon, sulfur, and oxygen of the bulk core composition were summarized in Table 3-2 and Fig. 3-3. The estimates of element abundances in the inner and outer cores were also shown in Table 3-2 and Fig. 3-3.

3.4.2. Estimate of the composition of the core

Based on the result of calculation, we constrained that the total amount of light elements in the bulk core was 7.4(26)–9.9(13) wt. %. In these variations of the bulk core composition, the oxygen content varies from 5.6(23) wt. % to 0 wt. %, whereas the silicon content varies from 0 wt. % to 3.5(12) wt. %. When the total light element content of the bulk core is 7.4 wt. %, we may expect the bulk core contains 1.8(49) wt. % of sulfur and 5.6(23) wt. % of oxygen without silicon. Therefore, the Earth's inner core contains minor amount of sulfur, and 4.3(1) wt. % of oxygen, while the light elements in the outer core is 1.9(51) wt. % of sulfur, and 5.6(26) wt. % of oxygen (Fig. 3-3). If the bulk core contains 9.9 wt. % of light elements, the light elements of the bulk core were estimated to be 3.5(12) wt. % of silicon and 6.4(25) wt. % of sulfur without oxygen. Hence, the inner core contains 4.3(2) wt. % of silicon

Table 3-2 The estimate of the chemical compositions of the Earth's core.

Partitioning coefficient of Si, S, and O (This study)							
	$D_{silicon}$	1.25	±0.72				
	D_{sulfur}	0.02	±0.02				
	D_{oxygen}	0.76	±0.56				
The eatimate value of element abandance in the bulk/inner/outer core							
Bulk core	Si	0	-	-	3.5	±1.2	[wt.%]
	S	1.8	±4.9	-	6.4	±2.5	[wt.%]
	O	5.6	±2.3	-	0	-	[wt.%]
	Total	7.4	±2.6		9.9	±1.3	[wt.%]
Inner core	Si	0	-	-	4.3	±0.2	[wt.%]
	S	0	±0.1	-	0.1	±0.1	[wt.%]
	O	4.3	±0.1	-	0	-	[wt.%]
Outer core	Si	0	-	-	3.4	±1.2	[wt.%]
	S	1.9	±5.1	-	6.8	±2.7	[wt.%]
	O	5.6	±2.6	-	0	-	[wt.%]

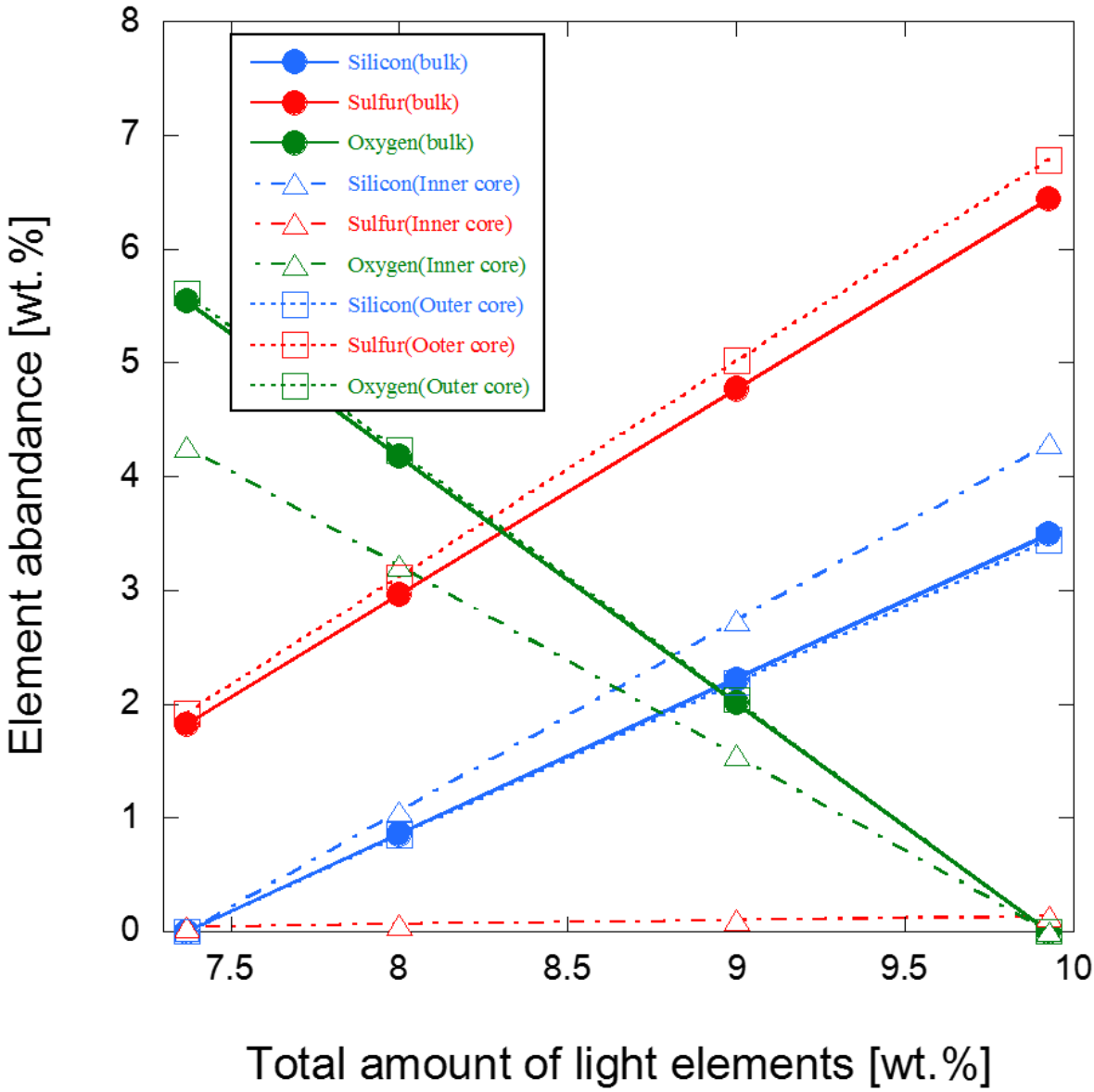

Fig. 3-3. The estimate values of element abundances in the bulk, inner and outer cores of the Earth. The blue, red, and green solid circles represent the abundances of silicon, sulfur, and oxygen in the bulk core, respectively. The blue, red, and green open triangles show the abundances of silicon, sulfur, and oxygen in the inner core. The blue, red, and green open squares show the abundances of silicon, sulfur, and oxygen in the outer core, respectively.

and 0.1(1) wt. % of sulfur, whereas the light elements in the outer core is mainly sulfur, amounting to 6.8(27) wt. %, with 3.4(12) wt. % of silicon (Fig. 3-3). This approximation indicates that the contents of silicon and oxygen in the inner and outer cores depend crucially on the bulk core composition. On the other hand, the content of sulfur in the inner core is consistently minor and outer core is sulfur-rich. My results demonstrate that the present-day Earth has a sulfur-rich outer core and a significant amount of sulfur may create the seismologically observed density contrast between the inner and outer cores. The density contrast between inner and outer cores may not be explained by silicon or oxygen alone. Although the compositional model of the core has a large range and it depends on the bulk core composition, my compositional model of the inner and outer cores are consistent with the compositions of the inner and outer cores proposed by previous studies based on mineral physics constraints [e.g., *Badro et al*., 2007; *Antonangeli et al*., 2010; *Huang et al*., 2011; *McDonough,* 2003]. Further experiment and theoretical information of the density and sound velocity on the iron alloys will help us for better understanding of processes occurred during core information and composition of the Earth's core.

3.5. References

Akahama, Y. and H. Kawamura (2004), High-pressure Raman spectroscopy of diamond anvils to 250 GPa: Method for pressure determination in the multimegabar pressure range, *J. Appl. Phys.* **96(7)**, 3748–3751.

Alfè. D., M. J. Gillan, and G. D. Price (2002), Composition and temperature of the Earth's core constrained by combining *ab initio* calculations and seimic data, Earth. Planet. Sci. Lett. **195**, 91–98.

Allègre, C. J., J. P. Poirier, E. Humler, and A. W. Hofmann (1995), The chemical composition

of the Earth, *Earth Planet. Sci. Lett.* **134**, 515–526.

Antonangeli, D., J. Siebert, J. Badro, D. L. Farber, G. Fiquet, G. Morard, and F. J. Ryerson (2010), Composition of the Earth's inner core from high-pressure sound velocity measurements in Fe–Ni–Si alloys, *Earth Planet. Sci. Lett.* **295**, 292–296.

Asanuma, H., E. Ohtani, T. Sakai, H. Terasaki, S. Kamada, N. Hirao, N. Sata, and Y. Ohishi (2008), Phase relations of Fe–Si alloy up to core conditions: Implications for the Earth inner core, *Geophys. Res. Lett*. **35**, L12307.

Badro, J., G. Fiquet, F. Guyot, E. Gregoryanz, F. Occelli, D. Antonangeli, and M. d'Astuto (2007), Effect of light elements on the sound velocities in solid iron: implications for the composition of Earth's core, *Earth Planet. Sci. Lett.* **254**, 233–238.

Birch, F. (1964), Density and composition of mantle and core, *J. Geophys. Res*. **69(20)**, 4377–4388.

Boehler, R. (1996), Melting and element partitioning Fe–FeS eutectic temperatures to 620 kbar, *Phys. Earth Planet. Inter*. **96**, 181–186.

Deweale, A., P. Loubeyre, and M. Mezouar (2004), Equation of state of six metals above 94 GPa, *Phys. Rev.* B. **70**, 094112.

Dubrovinsky, L. S., S. K. Saxena, F. Tutti, S. Rekhi, and T. LeBehan (2000), In situ X-ray study of thermal expansion and phase transition of iron at multimegabar pressure, *Phys. Rev. Lett.* **84(8)**, 1720–1723.

Dziewonski, A.M. and D.L. Anderson (1981), Preliminary reference Earth model, *Phys. Earth Planet. Inter*. **25**, 297–356.

Fei, Y., C. M. Bertka, and L. W. Finger (1997), High-pressure iron–sulfur compound, Fe_3S_2, and melting relations in the Fe–FeS system, *Science* **275**, 1621–1623.

Fei, Y., J. Li, C. M. Bertka, and C. T. Prewitt (2000), Structure type and bulk modulus of Fe_3S,

a new iron–sulfur compound, *Am. Mineral.* **85**, 1830–1833.

Fischer, R. A., A. J. Campbell, G. A. Shofner, O. T. Lord, P. Dera, and V. B. Prakapenka (2011), Equation of state and phase diagram of FeO, *Earth Planet. Sci. Lett*. **304**, 496–502.

Fischer, R. A., A. J. Campbell, R. Caracas, D. M. Reaman, D. L., Heinz, P. Dera, and V. B. Prakapenka (2014), Equation of state in the Fe–FeSi system at high pressures and temperatures, *J. Geophys. Res*. **119**, 2810–2817.

Gudfinnsson, G. H., and D. C. Presnall (2001), A pressure-independent geothermometer for primitive mantle melts, *J. Geophys. Res.* **106**, 205-211.

Hillgren, V., C. K. Gessman, and J. Li (2000), An experimental perspective on the light element in Earth's core, In: Canup, R. M., Righter, K. (Eds.), *Origin of the Earth and Moon.* The University of Arizona, pp. 245–263.

Huang, H., Y. Fei, L. Cai, F. Jing, X. Hu, H. Xie, L. Zhang, and Z. Gong (2011), Evidence for an oxygen-depleted liquid outer core of the Earth, *Nature.* **479**, 513–516.

Kamada, S., H. Terasaki, E. Ohtani, T. Sakai, T. Kikegawa, Y. Ohishi, N. Hirao, N. Sata, and T. Kondo (2010), Phase relationships of the Fe–FeS system in conditions up to the Earth's outer core, *Earth Planet. Sci. Lett*. **294**, 94–100.

Kamada, S., E. Ohtani, H. Terasaki, T. Sakai, M. Miyahara, Y. Ohishi, and N. Hirao (2012), Melting relationships in the Fe–Fe_3S system up to the outer core conditions, *Earth Planet. Sci. Lett*. **359–360**, 26–33.

Li, J., Y. Fei, H. K. Mao, K. Hirose, and S.R. Shieh (2001), Sulfur in the Earth's inner core, *Earth Planet. Sci. Lett*. **193**, 509–514.

Li, J. and Y. Fei (2003), Experimental constrains on core composition, In: Carlson, R. W. (Ed.), *Treatise on Geochemistry 2: The Mantle and Core*. Elsevier, Amsterdam, pp. 521–546.

Lin, J. F., D. L. Heinz, A. J. Campbell, J. M. Devine, and G. Shen (2002), Iron-Silicon alloy in

Earth's core? *Science* **295**, 313–315.

McDonough, W. F. (2003), Compositional model for the Earth's core, in Treatise of Geochemistry, vol. 2, edited by R. W. Carlson, pp. **547–568**, Elsevier-Pergamon, Oxford.

Morard, G. and T. Katsura (2010), Pressure–temperature cartography of Fe–S–Si immiscible system, *Geochimica et Cosmochimica Acta* **74,** 3659–3667.

Ohishi, Y., N. Hirao, N. Sata, K. Hirose, and M. Takata (2008), Highly intense monochromatic X-ray diffraction facility for high-pressure research at SPring-8, *High Pressure Res.* **28**, 163–173.

Poirier, J. P. (1994), Light elements in the Earth's outer core: a critical review, *Phys. Earth Planet. Inter.* **6**, 123–130.

Ringwood, A. E. (1959), On the chemical evolution and densities of the planets, *Geochem. Cos*. **15**, 257–283.

Sakai, T., T. Kondo, E. Ohtani, H. Terasaki, N. Endo, T. Kuba, T. Suzuki, and T. Kikegawa (2006), Interaction between iron and post-perovskite at core-mantle boundary and core signature in plume source region, *Geophys. Res.* **33**, L15317.

Sakai, T., S. Takahashi, N. Nishitani, I. Mashino, E. Ohtani, and N.Hirao (2014), Equation of state of pure iron and Fe0.9Ni0.1 alloy up to 3 Mbar, *Phys. Earth Planet. Inter*. **228**, 114–126.

Sanloup, C. and Y. Fei (2004), Closure of the Fe–S–Si liquid miscibility gap at high pressure, *Phys. Earth Planet. Inter.* **147**, 57–65.

Seagle, C. T., A. J. Campbell, D. L. Heinz, G. Shen, and V. B. Prakapenka (2006), Thermal equation of state of Fe3S and implications for sulfur in Earth's core, *J. Geophys. Res*., **111**, B06209.

Seto, Y., D. Nishio-Hamane, T. Nagai, and N. Sata (2010), Development of a software suite on

X-ray diffraction experiments, *Rev High Pressure Sci Technol* 20, 269–276.

Shen, G., H. K. Mao, and R. J. Hemley (1996), Laser-heated diamond anvil cell technique: double-sided heating with multimode Nd:YAG laser, *Advanced Materials '96: New Trends in High-Pressure Research*. Nat. Inst. Res. Inorg. Mater. Tsukuba, pp. 149–152.

Takafuji, N., K. Hirose, M. Mitome, and Y. Bando (2005), Solubilities of O and Si in liquid iron in equilibrium with (Mg, Fe)SiO_3 perovskite and the light elements in the core, *Geophys. Res. Lett.* **32**, L06313.

Tateno, S., H. Hirose, Y. Ohishi, and Y. Tatsumi (2010), The structure of iron in Earth's inner core, *Science*, **330**, 359–361.

Terasaki, H., S. Kamada, T. Sakai, E. Ohtani, N. Hirao, and Y. Ohishi (2011), Liquidus and solidus temperature of a Fe–O–S alloy up to the pressures of the outer core: Implication for the thermal structure of the Earth's core, *Earth Planet. Sci. Lett*. **232**, 379–392.

Umemoto, K., K. Hirose, S. Imada, Y. Nakajima, T. Komabayashi, S. Tsutsui, and A. Q. R. Baron (2014), Liquid iron-sulfur alloys at outer core conditions by first-principles calculations, *Geophys. Res. Lett*. **41**, 6712–6717.

Vočadro, L., D. Alfè, M J. Gillan, and G. D. Price (2003), The properties of iron under core conditions from first principles calculations, *Phys. Earth Planet. In*. **140**, 101–125.

Watanabe, K. (2015), Experimental constraints on the chemical composition of the Earth's core, Tohoku University, Master thesis.

Watanabe, K. (2015), Element partitioning of S, Si, and O between metallic solid and liquid in the Fe–S–Si–O system at high pressure and temperature: Implications for the planetary core, Tohoku University, Graduation thesis.

Chapter 4:

Sound velocity measurements of Fe–Si alloy at high pressure and temperature

4.1. Introduction

The physical properties of the Earth's deep interior have been demonstrated as "PREM (Preliminary Earth reference model)" based on seismological observations [*Dziewonski and Anderson*, 1981]. PREM shows the density (ρ) and sound velocities (V_P, V_S) of the Earth and Earth's inner core is mainly composed of an iron alloy with light elements, such as sulfur (S), silicon (Si), oxygen (O), carbon (C), and hydrogen (H), to account for the core density deficit [*Birch*, 1964]. We can constrain the composition of the core by comparing sound velocity data of Fe and Fe alloy with PREM. Therefore, Sound velocity measurement of Fe and Fe-light element alloy is essential to understand the chemical properties of the core and have been performed under high pressure conditions using various method, such as shockwave measurements [e.g., *Brown and McQeen*, 1986], inelastic X-ray scattering (IXS) [e.g., *Kamada et al*., 2014; *Ohtani et al*., 2013; *Sakamaki et al*., 2016; *Shibazaki et al*., 2012], nuclear resonant inelastic X-ray scattering (NRISX) [e.g., *Lin et al*., 2005]. It is accepted that there is a liner relation between density and sound velocity, i.e., Birch's law [*Birch*, 1961]. However, the effect of temperature on Birch's law is not revealed in detail because of experimental difficulty and under debate [e.g., *Antonangeli et al*., 2004; *Sakamaki et al*., 2016].

Silicon is one of major candidates as light element in the Earth's core. Sound velocity of Fe–Si alloy at room temperature has been measured by NRIXS [*Lin et al*., 2003] and IXS method [*Badro et al*., 2007; *Mao et al*., 2012]. *Lin et al*. [2003] reported the sound velocity of $Fe_{0.85}Si_{0.15}$ alloy based on NRIXS and they mentioned that silicon alloyed with iron increases the compressional wave velocity and share wave velocity of iron under high pressure. *Badro et*

al. [2007] measured the sound velocity of FeSi based on IXS measurements and showed that the incorporation of small amounts of silicon, 2.3 wt. %, is comparable with geophysical observation. On the other hand, *Mao et al*. [2012] reported the sound wave velocity of $Fe_{0.85}Si_{0.15}$ alloy by IXS and their data demonstrated that the sound velocity profile of iron with 8 wt. % Si at 6000 K matches with PREM of the inner core. As mentioned above, the effect of silicon on sound velocity of iron and the silicon content in the inner core have been discussed in previous studies. However, the sound velocity measurements of Fe–Si alloy at high temperature have not been reported and sound velocity of Fe–Si alloy at high pressure and temperature is still unclear.

The sound velocity of hcp Fe–Si alloy at high pressure and temperature gives us an important constraint on the composition of the Earth's inner core. The candidate for the Earth's inner core is required to match both the core density and sound velocity at pressure and temperature conditions of the core. Here, I reported the sound velocity of Fe–Si alloy up to 76 GPa and 2500 K based on IXS measurements and the effect of temperature on the sound velocity of Fe–Si alloy and silicon content in the inner core were discussed.

4.2. Experimental procedure

4.2.1. Sample preparation

High pressure was generated by a symmetric-type DAC. The culet sizes of the diamond anvils were 300 and 200 μm, depending on the desired experimental pressures. The starting material used in this study was Fe–6 wt. % Si alloy (99.9% purity; Rare Metallic Co., Ltd). A thin foil of starting material was made using a cold compression technique. The sample foil was sandwiched between NaCl pellets, which worked as a pressure medium, thermal

insulator, and pressure marker. A rhenium gasket was pre-indented to a thickness of 30–50 μm and 80–100 μm in diameter hole and was drilled into the indentation to shape a sample chamber.

4.2.2. Inelastic X-ray scattering at SPring-8

Sound velocity of Fe–Si alloy was measured based on inelastic X-ray scattering technique at the BL35XU beamline of the SPring-8 facility [*Baron et al*., 2000]. The Si (9 9 9) backscattering optics was used, which provides an incident photon energy of 17.794 keV with an energy resolution of 2.8 meV full width at half-maximum (FWHM). The scattered X-rays were analyzed by 12 crystals, which are arranged in a 2-dimensional (3×4) array. The momentum transfer, $Q=2k_0\sin(2\theta/2)$, where k_0 is the wave vector of the incident photons and 2θ is the scattering angle, was selected by rotating the spectrometer arm in the horizontal plane. The X-ray beam size was focused to 16 μm×16 μm by a Kirkpatrick-Baez (KB) mirror pair. IXS spectra was collected in the range of Q= 6.15–9.52 nm^{-1} at each pressure conditions. The momentum resolution was set to about 0.4 nm^{-1} full width. The experimental duration was about 8-12 hours at room temperature and 6-8 hours at high temperature condition.

In order to calculate the density of Fe–Si alloy, X-ray diffraction patterns of samples were also obtained using a Flat panel detector (FP; C9732DK, Hamamatsu Photonics K.K.) at same experimental conditions as IXS measurements. The camera length between the sample and FP was calibrated by collecting the diffraction pattern of CeO_2. The density of Fe–Si alloy was calculated based on lattice parameters of Fe–Si alloy in XRD pattern. The experimental pressure was determined from the lattice parameters of NaCl using the EOS of B2 phase [*Fei et al.*, 2007] of NaCl. The details of pressure calculation were shown in Chapter 2. Typical X-ray diffraction pattern from the sample was shown in Fig. 4-1.

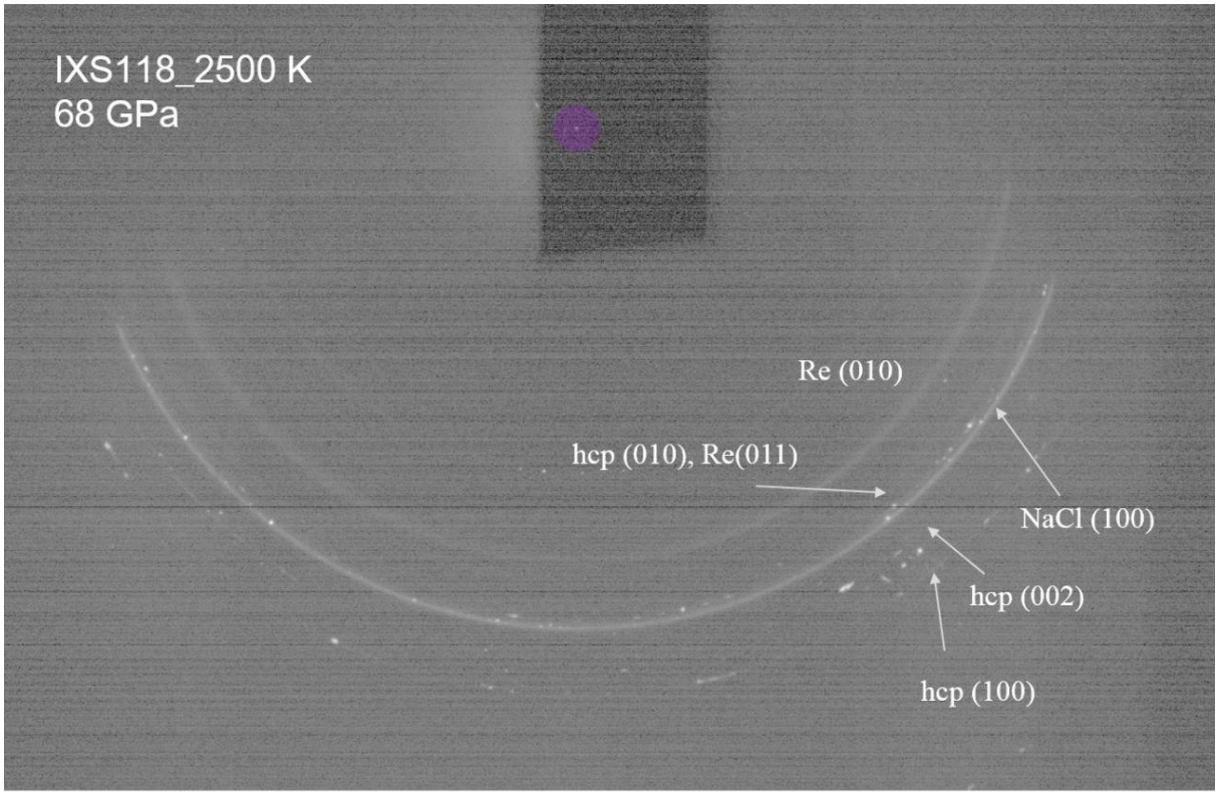

Fig. 4-1. Typical 2D image of X-ray diffraction pattern at 68 GPa and 2500 K (run IXS118). The diffraction patterns from hcp Fe–Si alloy, NaCl, and Re were observed.

The example of the IXS spectra collected at 46 GPa and 1800 K was shown in Fig. 4-2. The spectra are characterized by an elastic contribution centered at zero energy and inelastic contributions from Fe-Si alloy and diamond derived from the diamond anvils. As shown in Fig. 4-2, the spectra derived from the longitudinal acoustic (LA) phonons of Fe-Si alloy was observed between the peak of the elastic scattering of the sample and the transverse acoustic (TA) phonons of the diamond. The energy positions of phonons were extracted by fitting the spectra data with a set of Lorentzian functions. In order to determine the compressional sound velocity (V_P), the obtained phonon dispersion were fitted using a sine function as shown below:

$$E[meV] = 4.192\times10^{-4} V_P[m/s] \times Q_{MAX}[nm^{-1}] \sin\left(\frac{\pi}{2}\frac{Q[nm^{-1}]}{Q_{MAX}[nm^{-1}]}\right) \quad (4.1)$$

where E and Q are the energy and the momentum of the acoustic mode and V_P is the sound velocity of Fe–Si alloy in this study. Q_{MAX} is corresponding to the first Brillouin zone edge [e.g., *Fiquet et al*., 2004]. V_P and Q_{MAX} were taken as free parameters.

For high temperature experiments, the COMPAT laser-heating system, which has been developed for LHDAC by *Fukui et al*. [2013], was used and the sample was heated using fiber laser (λ= 1.070 μm). The temperature has been monitored for experimental duration and recorded every 30 min during laser heating. Temperature was determined by fitting Plank's formula to a spectrum of thermal radiation from the sample. The experimental temperature was calculated by averaging the variation in the heating area during the IXS measurements.

4.3. Results

4.3.1. Sound velocity of Fe-Si alloy

IXS measurements were conducted in the pressure range from 44 to 76 GPa and the

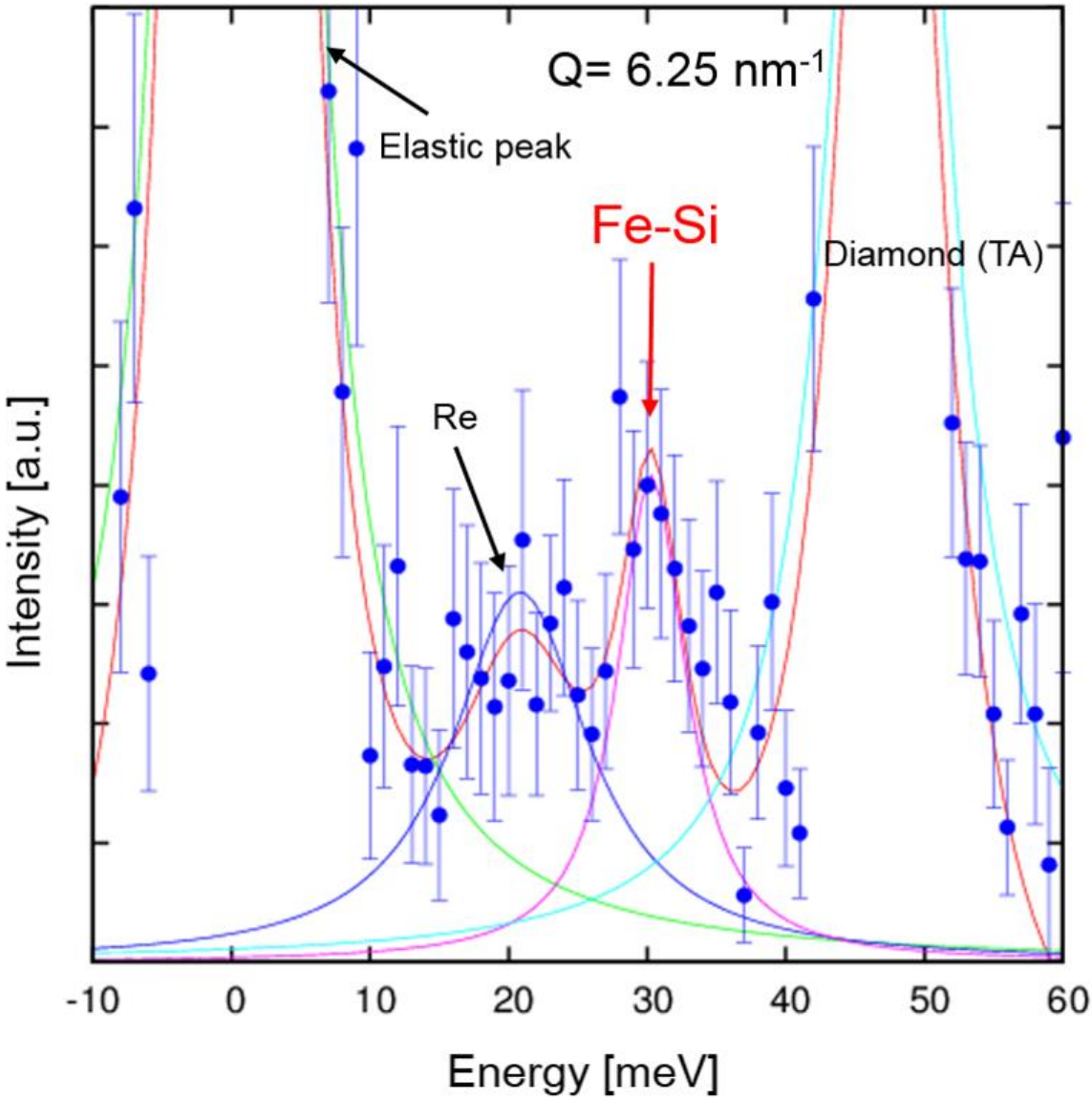

Fig. 4-2. Typical IXS spectra at 46GPa (run IXS121). Peaks were assigned to an elastic scattering, LA phonon of Fe–Si alloy, and Re using as gasket, and TA phonon of diamond using as anvils. The spectra was fitted by a Lorentzian function.

Table. 4-1 Experimental conditions and density, V_P and Q_{MAX}

Run No	Pressure(GPa)	Temperature(K)	ρ (g/cm^3)	*error*	*Vp* (km/s)	*error*	Q_{MAX} (nm-1)	*error*
IXS113	94	300	10.51	0.07	9.35	0.18	16.90	1.50
IXS116	67	300	9.70	0.02	9.55	0.22	14.60	1.13
IXS117	68	2000	9.77	0.03	9.99	0.30	13.08	1.12
IXS118	68	2500	9.74	0.03	9.44	0.26	15.16	1.50
IXS121	46	1800	9.21	0.03	8.16	0.18	13.86	0.89
IXS122	44	300	9.15	0.02	8.14	0.15	13.90	0.82
IXS132	59	1800	9.74	0.03	8.75	0.22	13.49	0.96
IXS146	58	1600	9.49	0.03	8.44	0.25	15.54	1.73
IXS148	63	2000	9.69	0.03	8.42	0.17	15.94	1.29
IXS149	61	300	9.70	0.03	8.26	0.20	16.98	1.88
IXS152	76	300	9.89	0.02	8.78	0.38	15.21	2.31
IXS153	70	1600	10.10	0.02	8.94	0.30	13.81	1.39

temperature range from 300 to 2500 K. The experimental conditions are summarized in Table 4-1. I conducted the experiments in the P-T conditions which corresponds to the crystal structure of Fe-Si alloy as hcp phase because Earth's inner core is considered to be hcp phase [e.g., *Tateno et al*., 2010]. Dispersion curves of Fe–Si alloy at each measurement were shown in Fig.4-3 and all dispersion curves were compiled in Fig. 4-4. The obtained density (ρ), V_P, and Q_{MAX} in this study were also shown in Table 4-1. We can see that V_P and Q_{MAX} increases with increasing pressure.

4.3.2. Birch's law of Fe-Si alloy

In order to define the Birch's law of Fe–Si alloy, the result of IXS measurement of Fe–6 wt. % Si at 94 GPa and 300 K was referred in this study [*Takahata*, 2015 (Master thesis)]. In Fig. 4-4, we can see that the dispersion curves of run IXS116, IXS117, and IXS118 did not follow the trend of other data. This is caused due to weak intensity of sample peak and lack of quality of IXS spectra. Therefore, the results of these runs cannot be used discussion and will be excluded from the following discussion.

Fig. 4-5 shows the measured V_P of Fe-Si alloy as a function of density. The V_P of Fe-Si alloy in this study were followed linear relationships between density and velocity, i.e., Birch's law. To evaluate the effect of temperature on the sound velocity of Fe–Si alloy, the V_P data at room temperature and high temperature were fitted separately using Birch's law. The Birch's law of Fe–Si alloy at room temperature was obtained as shown below:

$$V_P = 0.89 \pm 0.19 \times \rho - 0.13 \ (\pm 1.90) \quad (4\text{-}2)$$

On the other hand, the Birch's law at high temperature was expressed as below:

$$V_P = 0.85 \pm 0.22 \times \rho + 0.35 \ (\pm 2.08) \quad (4\text{-}3)$$

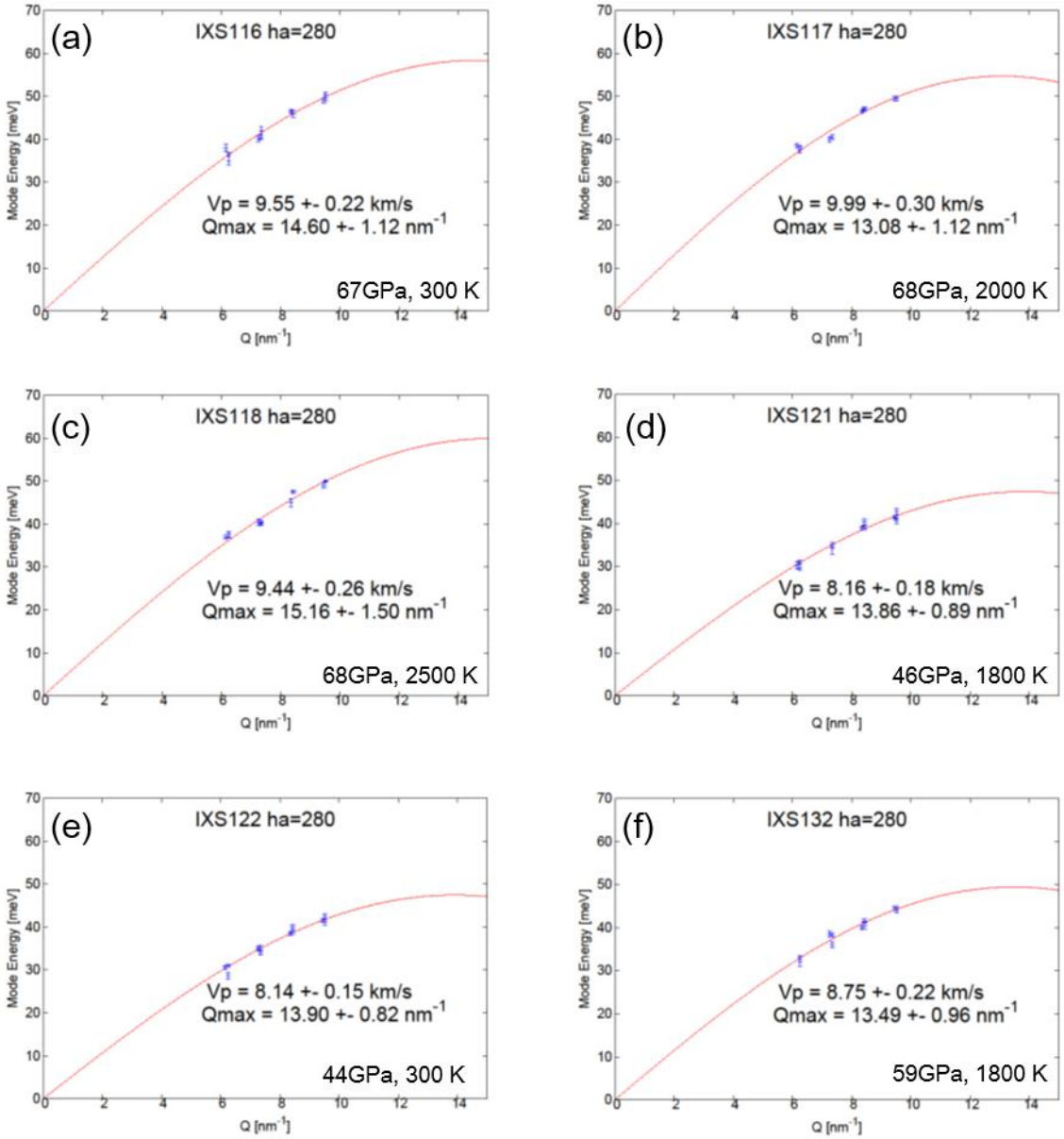

Fig. 4-3. Dispersion curves in this study at (a) 67 GPa and 300 K, (b) 68 GPa and 2000K, (c) 68 GPa and 2500 K, (d) 46 GPa and 1800 K, (e) 44 GPa and 300K, (f) 59 GPa and 1800 K, (g) 58 GPa and 1600 K, (h) 63 GPa and 2000 K, (i) 61 GPa and 300 K, (j) 76 GPa and 300 K, and (k) 70 GPa and 1600 K.

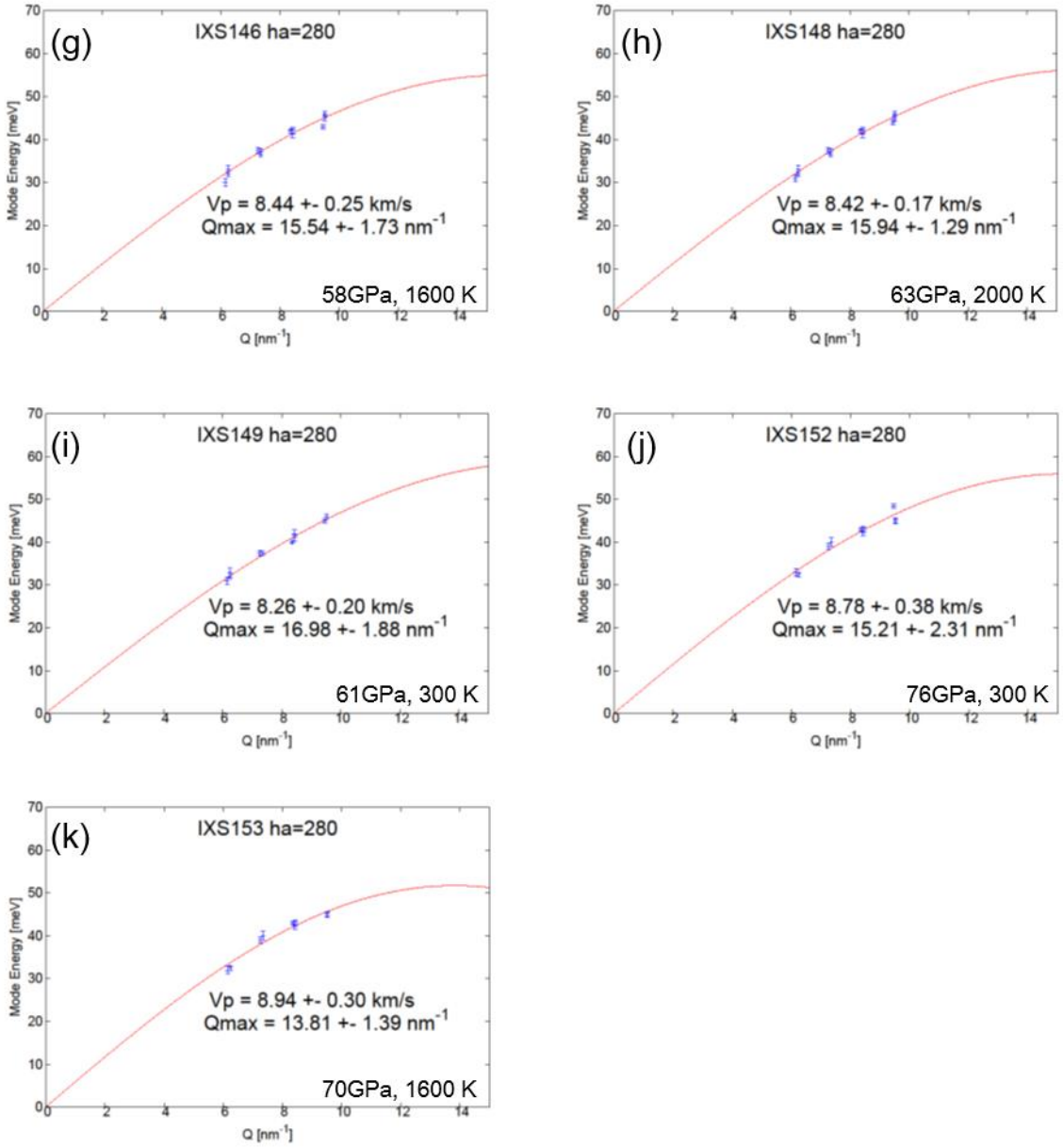

Fig. 4-3. *Continued*

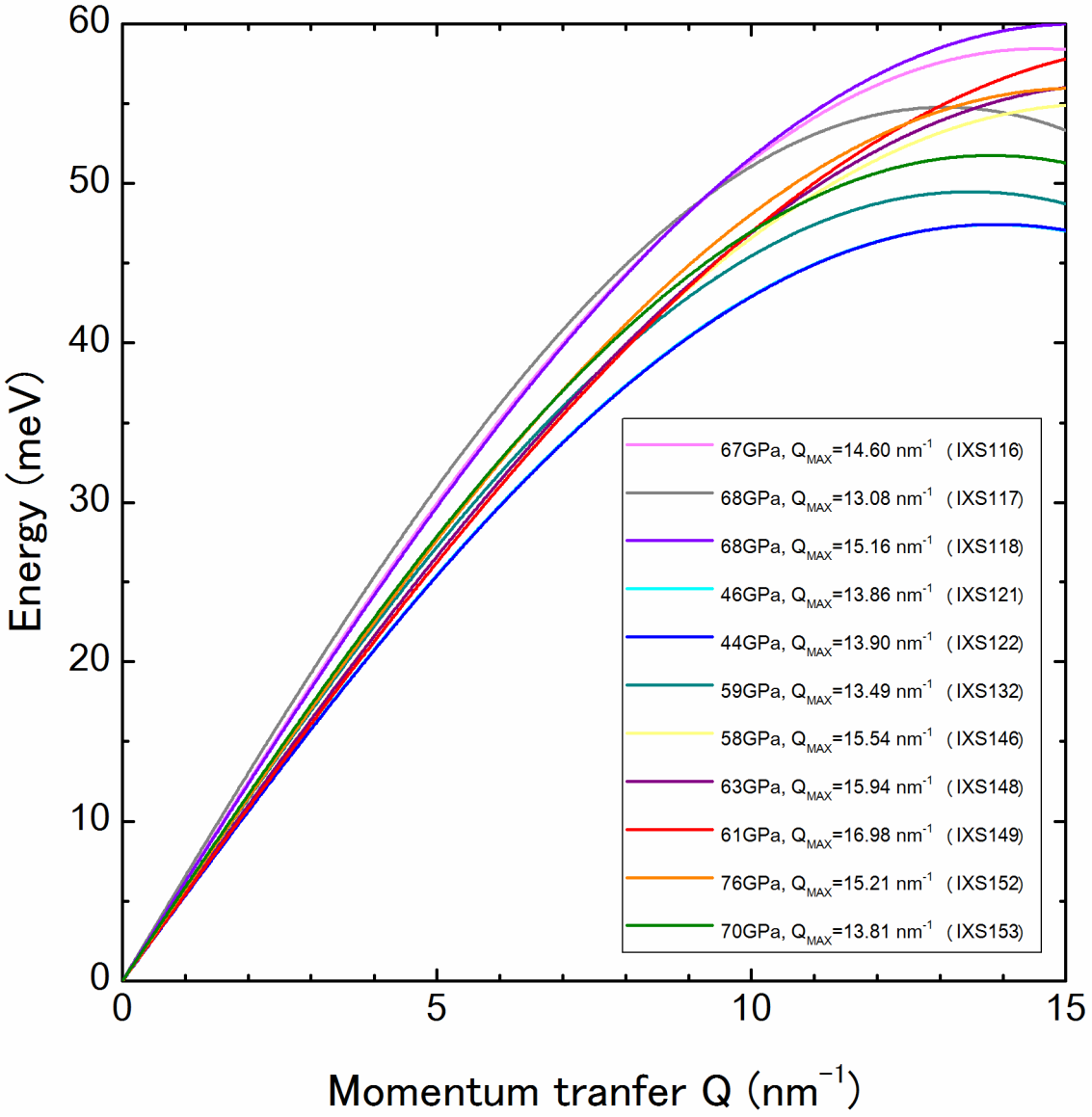

Fig. 4-4. Dispersion curves of Fe–Si alloy in the pressure 44–76 GPa in this study. Experimental conditions and obtained V_P and Q_{MAX} were shown in Table 4-1.

4.4. Discussion

4.4.1. The effect of temperature on sound velocity of Fe–Si alloy

As shown in Fig. 4-5, the present results demonstrated that obtained Birch's law at high temperature is closely similar to that of room temperature, and V_P measured at high temperature fall within errors of V_P at room temperature. Hence, the effect of temperature on V_P of Fe–Si alloy could be negligible at least in present experimental conditions, below 2000 K. Recent experimental study about sound velocity of pure iron [*Sakamaki et al*., 2016] argued that V_P of iron decreases with increasing temperature based on IXS measurements in high temperature conditions (~3000K). In view of the lack of experimental data of high temperature conditions in this study, the thermal effect on V_P of Fe–Si alloy is likely to be obtained at more high temperature conditions.

Then, including the relationships of V_P and ρ at high temperature, the obtained Birch's law was expressed as below in conclusion:

$$V_P = 0.90 \pm 0.12 \times \rho - 0.15 \ (\pm 1.19) \qquad (4\text{-}4)$$

4.4.2. Comparisons of Birch's law of Fe-Si alloy

In order to compare the Birch's law of Fe–Si alloy between this study and previous studies, the sound velocities of Fe–Si alloy measured by IXS method [*Badro et al*. 2007; *Mao et al*. 2012] and NRIXS method [*Lin et al*., 2004] were summarized in Fig. 4-6. The slope of Birch's law in this study was good agreement with previous IXS results of $Fe_{0.85}Si_{0.15}$ alloy reported by *Mao et al*. [2012]. On the other hand, there are large differences between my results and V_P of FeSi based on IXS measurements reported by *Badro et al*. [2007], and that of $Fe_{0.85}Si_{0.15}$ alloy based on NRIXS method by *Lin et al*. [2004]. These differences were caused

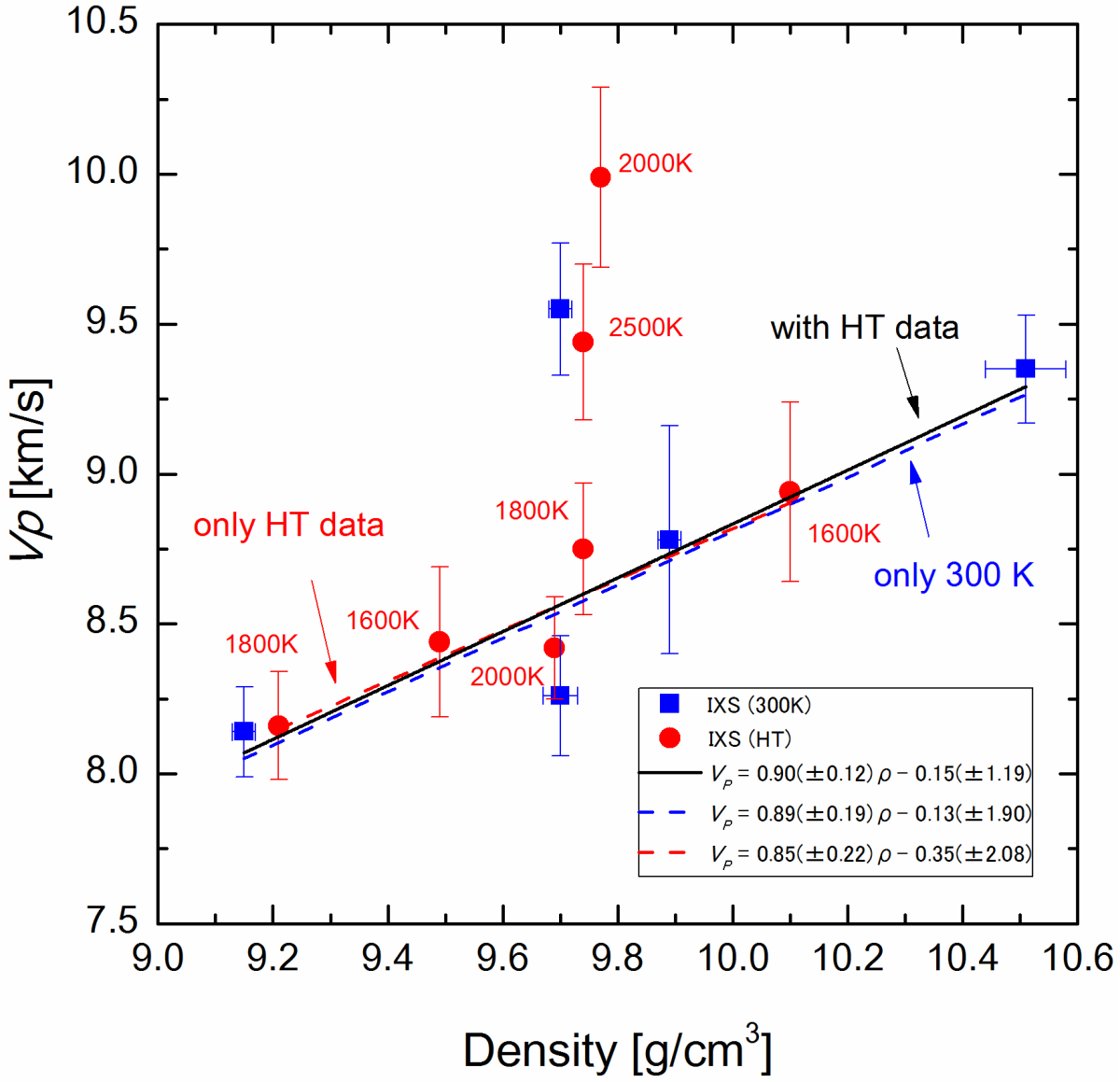

Fig. 4-5. The present results of measured V_P as a function of density. Blue solid square symbols show the data of V_P at room temperature. Red solid circle symbols show the data measured at high temperature. Black solid line represents the Birch's law of all IXS data (without run IXS116, IXS117, and IXS118). Red dashed line shows the Birch's law of high temperature data and Blue dashed line shows that of room temperature data, respectively.

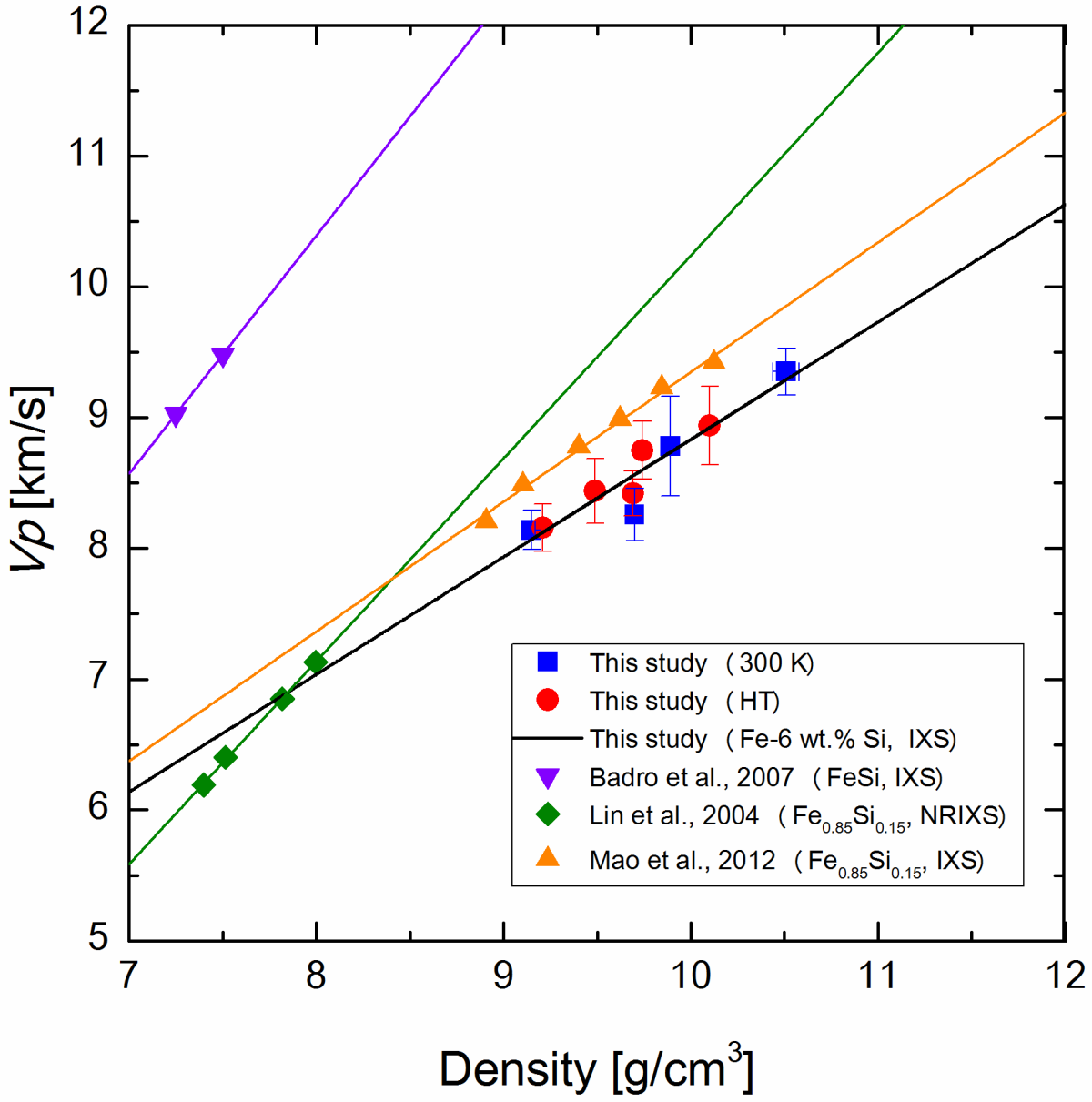

Fig. 4-6. Comparisons of Birch's law of Fe–Si alloys. Blue squares and red circles show the V_P of Fe–6 wt. % Si alloy at 300 K and high temperature conditions in this study. Black solid line represents the Birch's law of Fe–6 wt. % Si alloy in this study. Purple triangles show the results of V_P of FeSi based on IXS measurements by *Badro et al*. [2007]. Green diamonds show the results of NRIXS measurements of $Fe_{0.85}Si_{0.15}$ alloy by *Lin et al*. [2004]. In addition, orange triangles represent the results of IXS measurements of $Fe_{0.85}Si_{0.15}$ alloy by *Mao et al*. [2012].

due to the difference of crystal structure of Fe–Si alloy. The crystal structure of these Fe–Si alloys are bcc phase, whereas the structure of Fe-Si alloy in this study is hcp phase.

4.4.3. The amount of silicon in the Earth's inner core

The present experimental results of V_P for Fe–6 wt. % Si alloy demonstrated that the effect of temperature on V_P of Fe–Si alloy was very small and negligible in the temperature conditions below 2000 K. However, the temperature of the inner core was estimated to 5000 K–6000 K [e.g., *Terasaki et al*., 2011] and the thermal effect on V_P would not be ignored as reported in the case of iron [e.g., *Sakamaki et al*. 2016]. In order to consider the effect of temperature on V_P of Fe–Si alloy, the thermal effect on V_P of Fe–6wt. % Si was assumed to be the same as that of pure iron in this study. According to the high-temperature Birch's law of iron which proposed by *Sakamaki et al*. [2016], the Eq. (4-4) can be expressed as follows:

$$V_P = 0.90 \pm 0.12 \times \rho - 0.15\ (\pm 1.19) + [7.2\times10^{-5}\times(T-300)\times(\rho-14.2)] \quad (4\text{-}5)$$

In order to estimate the amount of silicon in the Earth's inner core, a linear mixing model, which introduced by some previous works [e.g., *Antonangeli et al*., 2010; *Badro et al*., 2007], was used. In this model, the average density ρ and sound velocity V of a two-component ideal solid solution are given as follows:

$$\rho = x\rho_{Fe\text{-}Si} + (1-x)\,\rho_{Fe} \quad (4\text{-}6)$$

and

$$V = \frac{V_{Fe-Si}V_{Fe}}{(1-x)V_{Fe-Si} + xV_{Fe}} \quad (4\text{-}7)$$

where x is the volume function of Fe–6 wt. % Si alloy. The average density ρ and sound velocity V were assigned to those of the inner core derived from the PREM [*Dzeiewonski and Anderson*, 1981]. The temperature at ICB was assumed to be 5500 K [e.g., *Terasaki et al*., 2011]. The

density of pure iron, ρ_{Fe}, at the high pressure and temperature conditions corresponding to the inner core was estimated by using thermal equation of state of iron [*Sakai et al*. 2014] and V_{Fe} was calculated based on a high–temperature Birch's law of iron which proposed by *Sakamaki et al*. [2015]. For the relation between $\rho_{Fe\text{-}Si}$ and $V_{Fe\text{-}Si}$, the obtained Birch's law for Fe–6 wt. % Si alloy in the present study was used (Eq. (4-5)) and the density of Fe–Si alloy at the inner core condition was calculated by the thermal equation of state of Fe–9 wt. % alloy [*Fischer et al*., 2014]. Sound velocities and Birch's law of pure iron and Fe–Si alloys as a function of density up to core pressure condition were summarized in Fig. 4-7.

Fig. 4-8 shows the comparison between the V_P of the linear mixing of Fe and Fe–6 wt. % Si and PREM at ICB condition as a function of density. From the data set of Eq. (4-6) and Eq. (4-7) and considering the V_P and density errors of PREM [*Masters*, 1979], the volume function of Fe–6 wt. % Si alloy x was determined to be 0.384(56), which indicate 2.2(3) wt. % of silicon at the ICB conditions (330 GPa and 5500 K). The present result indicates that a Fe alloy with 2.2(3) wt. % of silicon can explain both the density and sound velocity of the PREM at ICB condition assuming that the light element in the inner core is only silicon. This estimate value of silicon in the inner core is good agreement with previous IXS studies [*Antonangeli et al*., 2010; *Badro et al*., 2007]. The 2.2 wt. % of silicon determined from IXS measurements in this study may be the upper bound of the amount of silicon in the Earth's inner core because other light element, such as sulfur and oxygen, could be present in the core (see Chapter 3). It is necessary to perform further experiments of the sound velocity of variety of iron-light elements alloy at core condition for better understanding of composition of the Earth's core.

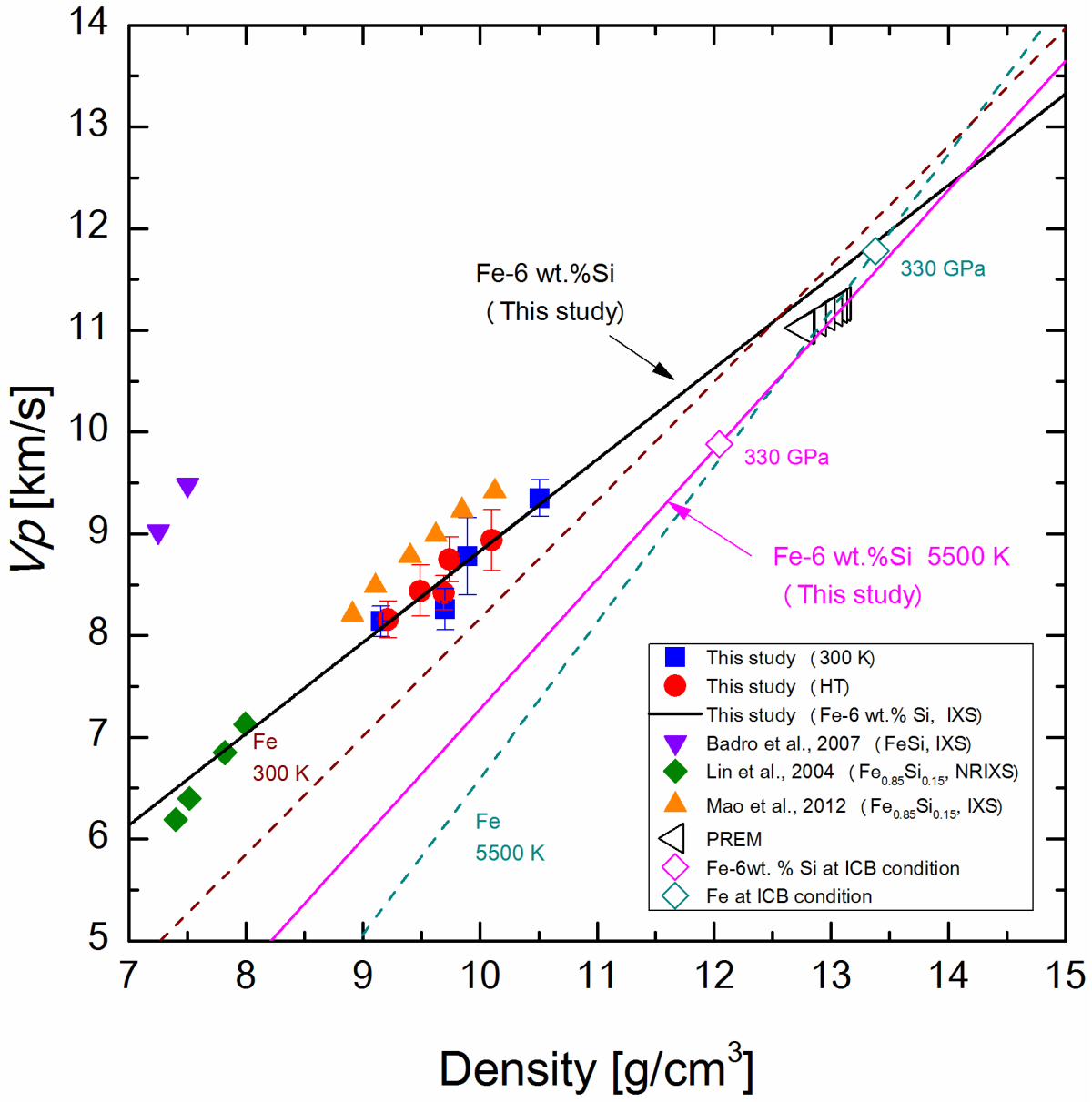

Fig. 4-7. Sound velocities and Birch's law of pure iron and Fe–Si alloys as a function of density. Blue squares and red circles show the V_P of Fe–6 wt. % Si alloy at 300 K and high temperature conditions in this study. Black solid line represents the Birch's law of Fe–6 wt. % Si alloy in this study. Open triangle symbols represent the density and V_P of PREM [*Dziewonski and Anderson*, 1981]. The dashed lines indicate the Birch's law for pure iron at 300 K and 5500 K based on the IXS measurements at high pressure and temperature conditions [*Sakamaki et al.*, 2016]. The density and V_P profiles at ICB condition (330 GPa, 5500 K) of Fe and Fe–Si alloy were also shown as open squares.

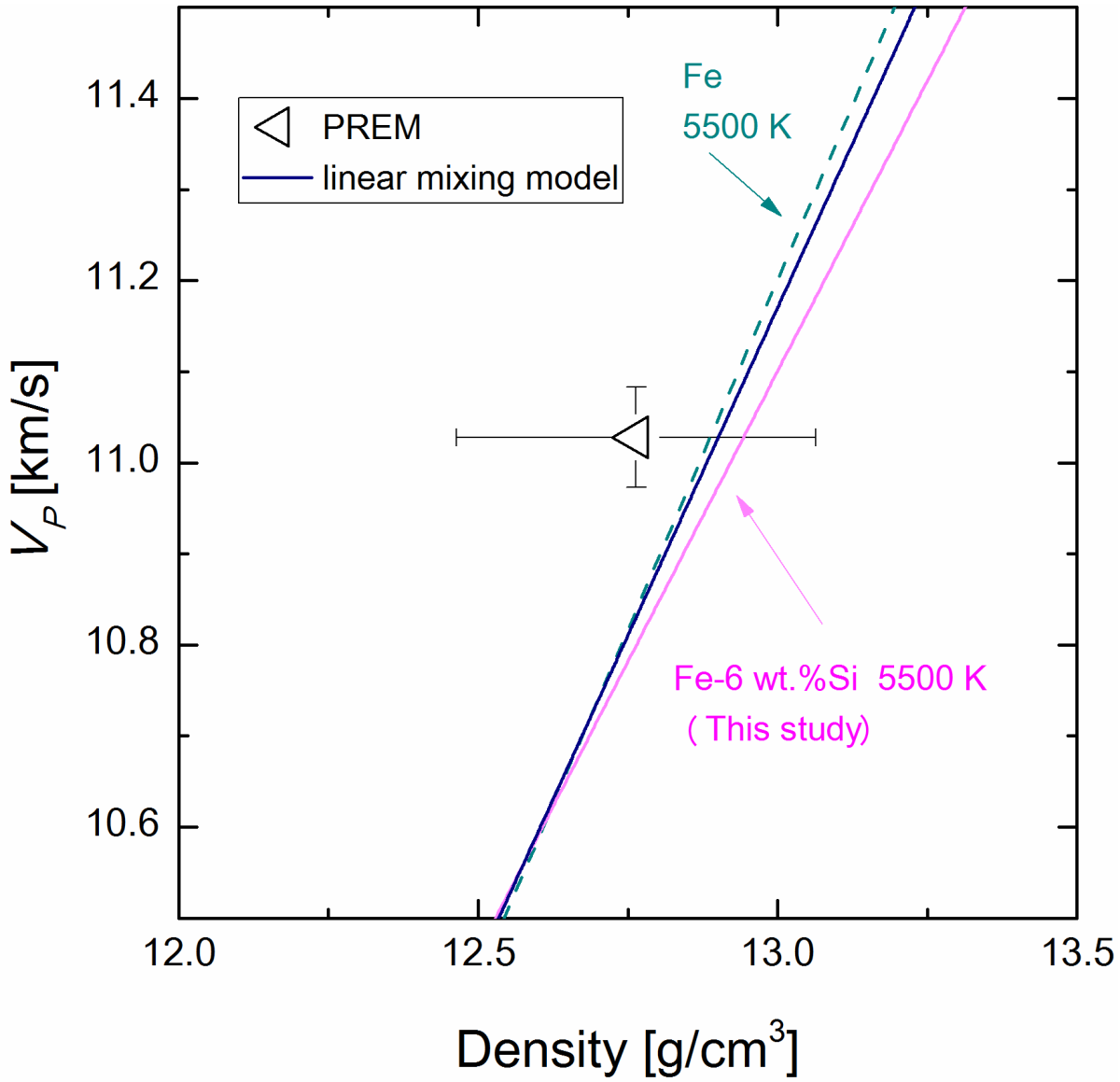

Fig. 4-7. The V_P of the linear mixing of Fe and Fe–6 wt. % Si as a function of density. The solid blue line represents the V_P of the linear mixing as a function of density. The linear mixing model was expressed as the set of Eq. (4-6) and Eq. (4-7) (see main text).The open triangle symbol shows the V_P of PREM at ICB condition. From the data set of Eq. (4-6) and Eq. (4-7) and considering the V_P and density errors of PREM [*Masters*, 1979], the volume function of Fe–6 wt. % Si alloy x was determined to be 0.384(56), which indicate 2.16(33) wt. % of silicon at the ICB conditions (330 GPa and 5500 K).

4.5. References

Antonangeli, D., J. Siebert, J. Badro, D. L. Farber, G. Fiquet, G. Morard, and F. J. Ryerson (2010), Composition of the Earth's inner core from high-pressure sound velocity measurements in Fe–Ni–Si alloys, *Earth Planet. Sci. Lett.* **295**, 292–296.

Badro, J., G. Fiquet, F. Guyot, E. Gregoryanz, F. Occelli, D. Antonangeli, and M. d'Astuto (2007), Effect of light elements on the sound velocities in solid iron: implications for the composition of Earth's core, *Earth Planet. Sci. Lett.* **254**, 233–238.

Birch, F. (1961), Composition of the Earth's Mantle. *Geophys. J. R. Astron. Soc.* **4**, 295–311.

Birch, F. (1964), Density and composition of mantle and core, *J. Geophys. Res*. **69(20)**, 4377–4388.

Baron, A. Q. R., Y. Tanaka, S. Goto, K. Takeshita, T. Matsushita, and T. Ishikawa (2000), An X-ray scattering beamline for studying dynamics, *J. Phys. Chem. Solids*. **61**, 461–465.

Brown, J. M. and R. G. McQueen (1986), Phase transitions Grüneisen parameter and elasticity for shocked iron between 77 GPa and 400 GPa. *J. Geophys. Res*. **91**, 7485–7494.

Dziewonski, A.M. and D.L. Anderson (1981), Preliminary reference Earth model, *Phys. Earth Planet. Inter*. **25**, 297–356.

Fiquet, G., J. Badro, F. Guyot, Ch. Bellin, M. Krisch, D. Antonangeli, H. Requardt, A. Mermet, D. Farber, C. Aracne-Ruddle, and J. Zhang (2004), Application of inelastic X-ray scattering to the measurements of acoustic wave velocities in geophysical materials at very high pressure. *Phys. Earth Planet. Inter.* **143–144**, 5–18.

Fischer, R. A., A. J. Campbell, R. Caracas, D. M. Reaman, D. L., Heinz, P. Dera, and V. B. Prakapenka (2014), Equation of state in the Fe–FeSi system at high pressures and temperatures, *J. Geophys. Res*. **119**, 2810–2817.

Fukui, H., T. Sakai, T. Sakamaki, S. Kamada, S. Takahashi, E. Ohtani, and A. Q. R. Baron (2013), A compact system for generating extreme pressures and temperatures: An application of laser-heated diamond anvil cell to inelastic X-ray scattering. *Rev. Sci. Instrum.* **84**, 113902.

Kamada, S., E. Ohtani, H. Fukui, T. Sakai, H. Terasaki, S. Takahashi, Y. Shibazaki, S. Tsutsui, A.Q.R. Baron, N. Hirao, and Y. Ohishi (2014), The sound velocity measurements of Fe_3S. *Am. Mineral.* **99**, 98–101.

Lin, J. F., V. V. Struzhkin, W. Sturhahn, E. Huang, J. Zhao, M. Y. Hu, E. E. Alp, H. K. Mao, N. Boctor, and R. J. Hemley (2003), Sound velocities of iron–nickel and iron–silicon alloys at high pressures. *Geophys. Res. Lett.* **30**, 2112.

Mao, Z., J. F. Lin, J. Liu, A. Alatas, L. Gao, J. Zhao, and H. K. Mao (2012), Sound velocities of Fe and Fe-Si alloy in the Earth's core. *Proc. Natl. Acad. Sci. U.S.A.* **109**, 10239–10244.

Masters, G. (1979), Observational constraints on the chemical and thermal structure of the earth's deep interior. *Geophys. J. R. Astronut. Soc*. **57**, 507–534.

Ohtani, E., Y. Shibazaki, T. Sakai, K. Mibe, H. Fukui, S. Kamada, T. Sakamaki, Y. Seto, S. Tsutsui, and A. Q. R. Baron (2013), Sound velocity of hexagonal close-packed iron up to core pressures. *Geophys. Res. Lett.* **40**, 5089–5094.

Sakamaki, T., E. Ohtani, H. Fukui, S. Kamada, S. Takahashi, T. Sakairi, A. Takahata, T. Sakai, S. Tsutsui, D. Ishikawa, R. Shiraishi, Y. Seto, T. Tsuchiya, and A. Q. R. Baron (2016), Constraints on the Earth's inner core composition inferred from measurements of the sound velocity of hcp-iron in extreme conditions, *Science Advances*, accepted.

Sakai, T., S. Takahashi, N. Nishitani, I. Mashino, E. Ohtani, and N.Hirao (2014), Equation of state of pure iron and Fe0.9Ni0.1 alloy up to 3 Mbar, *Phys. Earth Planet. Inter*. **228**, 114–126.

Shibazaki, Y., E. Ohtani, H. Fukui, T. Sakai, S. Kamada, D. Ishikawa, S. Tsutsui, A.Q.R. Baron, N. Nishitani, N. Hirao, and K. Takemura (2012), Sound velocity measurments in dhcp-FeH up to 70 GPa with inelastic X-ray scattering: Implications for the composition of the Earth's core. *Earth Planet. Sci. Lett.* **313-314**, 79-85.

Takahata, A. (2015), Melting temperature of the Fe-Ni-Si alloy and sound velocity measurements of Fe-Si alloy at high pressure: Implications for the structure of the core, Tohoku University, Master thesis.

Tateno, S., H. Hirose, Y. Ohishi, and Y. Tatsumi (2010), The structure of iron in Earth's inner core, *Science*, **330**, 359–361.

Terasaki, H., S. Kamada, T. Sakai, E. Ohtani, N. Hirao, and Y. Ohishi (2011), Liquidus and solidus temperature of a Fe–O–S alloy up to the pressures of the outer core: Implication for the thermal structure of the Earth's core, *Earth Planet. Sci. Lett*. **232**, 379–392.

Chapter 5:

Summary

5.1. Summary

The physical properties, such as density and sound velocity, of the Earth's deep interior have been investigated by seismic observations known as PREM. We can provide a constraint on the properties of the core by combining seismological data with mineral physics data based on high pressure experiments. It is accepted that the core of the Earth is composed of mainly Fe alloy. However, the density and sound velocity of pure iron at high pressure and temperature conditions could not explain those of PREM. In order to account for the contrast of density and sound velocity, the Earth's core contains some light elements (S, Si, O, C, and H). Sulfur and silicon are both major candidates as light elements in the core and some geochemical models predicted that sulfur and silicon could be present not only in the core of the Earth but also in the core of other terrestrial planets such as Mars and Mercury. In this study, high pressure experiments in the Fe–S–Si system have been conducted to reveal the chemical and physical properties of the Fe–S–Si system. The present experimental results were applied to discuss the properties of the planetary core.

At first, the phase and melting relationships in the Fe–S–Si system have been determined under high-pressure conditions. The phase and melting relationships in the Fe–S–Si system were studied up to 60 GPa by using a double-sided laser-heated diamond anvil cell combined with X-ray diffraction. I confirmed that hcp/fcc Fe–Si alloys and Fe_3S are stable phases under subsolidus conditions in the system. The liquidus phase changes from fcc to hcp at around 40 GPa. Both solidus and liquidus temperatures are significantly lower than the melting temperature of pure Fe, and both increase with increasing pressure. The slope of the Fe–S–Si liquidus temperature determined here is 12 K/GPa, which is significantly smaller than

the adiabatic temperature gradients of the liquid cores of Mercury and Mars, at around 18~27 K/GPa. Thus, crystallization of their cores started at the core–mantle boundary region even in the cores containing both silicon and sulfur as light elements. This crystallization start is consistent with the snowing-core model proposed by previous authors for the cores with the Fe–S systems [*Chen et al*., 2008; *Stewart et al*., 2007].

Secondly, element partitioning between metallic solid and liquid in the Fe–S–Si system were investigated up to 148 GPa based on the chemical analyses of recovered samples. The present results of partitioning behavior of sulfur and silicon indicate that a silicon-rich solid Fe alloy coexists with sulfur-rich metallic liquid. For discussion, the partition coefficients of sulfur, silicon, and oxygen (D_{sulfur}, $D_{silicon}$, D_{oxygen}) were obtained with the results of partitioning experiments in the Fe–S–Si–O and Fe–S–Si–O–Ni systems.

In order to discuss the chemical structure of the Earth's core, the D_{sulfur} and $D_{silicon}$ were extrapolated to the ICB condition and estimated to be 0.02(2) and 1.25(72), respectively. These results imply that sulfur is likely to be partitioned into the liquid outer core, whereas silicon is likely to be partitioned into the solid inner core. In the case of oxygen, D_{oxygen} at ICB condition was assumed to be 0.76(56), suggests oxygen is slightly enriched in the liquid phase. Based on the present partitioning data, the total amount of light elements in the bulk core of the Earth was constrained to be 7.4–9.9 wt. % and compositional model of the inner and outer cores was shown. The present results demonstrate that the present-day Earth has a sulfur-rich outer core and a significant amount of sulfur may create the seismologically observed density contrast between the inner and outer cores.

Finally, the sound velocity of Fe–6wt. % Si alloy at high pressure and temperature conditions was measured using inelastic X-ray scattering (IXS) method at BL35XU beamline of SPring-8 facility. IXS measurements were conducted in the pressure range from 44 to 76

GPa and the temperature range from 300 to 2500 K. The V_P of Fe–Si alloy in this study were followed linear relationships between density and velocity. The present results showed that the thermal effect on the V_P of Fe-Si alloy was very small than that of pure iron and the relationships of V_P and ρ at high temperature, i.e., Birch's law for Fe–6wt. % Si, was obtained as $V_P = 0.90 \pm 0.12 \times \rho - 0.15$ (±1.19). By using linear mixing model, the present result indicates that 2.2(3) wt. % of silicon in the inner core can explain both the density and sound velocity of the PREM at ICB condition assuming that the light element in the inner core is only silicon.

In this study, sulfur and silicon were focused as light elements in the planetary core and the composition of the Earth's core was discussed from both physical and chemical approaches. The present experimental results will provide an important constraint on the chemical property of the Earth's core assuming silicon and sulfur as light elements in the core. Further experiment and theoretical information of the density and sound velocity on the variety of iron alloys will help us for better understanding the "real" composition of the Earth's core.